

ALICE-ANA-2014-xxx  
January 28, 2023

# Strangeness Production ( $\Lambda$ ) in Jets and Medium in p-Pb collisions at $\sqrt{s_{NN}} = 5.02$ TeV

Ryan Hannigan

1. University of Texas at Austin

Emails: ryan.hannigan@austin.utexas.edu

## Abstract

By studying strange hadrons in proton-proton, proton-nucleus, and heavy ion collisions, one can investigate strange quark production and hadron formation with respect to increasing system size. Recent measurements show an enhancement of strange particles (e.g. an increase in the  $\Lambda/\pi$  ratio) in p-Pb and high multiplicity pp collisions. In order to probe the origin of this increase, it is necessary to separate the strange particles produced in hard processes (jets) from those produced in soft processes (bulk). By examining this trend from low to high multiplicity p-Pb collisions, we are able to study the onset of this enhancement from small to large collision systems.

Two-particle jet-like angular correlations with identified strange hadrons in p-Pb collisions allow us to measure both the jet and non-jet components of strange particle production. Modifications in the production mechanisms across different system sizes can be probed by examining changes in the  $\Lambda/h$  ratio within jets and in the underlying event separately. In addition, changes to the jet hadrochemistry via medium interactions are studied by measuring strangeness production in the away-side jet. In this note we present the first measurements of the  $\Lambda/h$  ratio in jets as a function of multiplicity using jet-like hadron- $\Lambda$  angular correlations in p-Pb collisions at  $\sqrt{s_{NN}} = 5.02$  TeV.



---

23 **Contents**

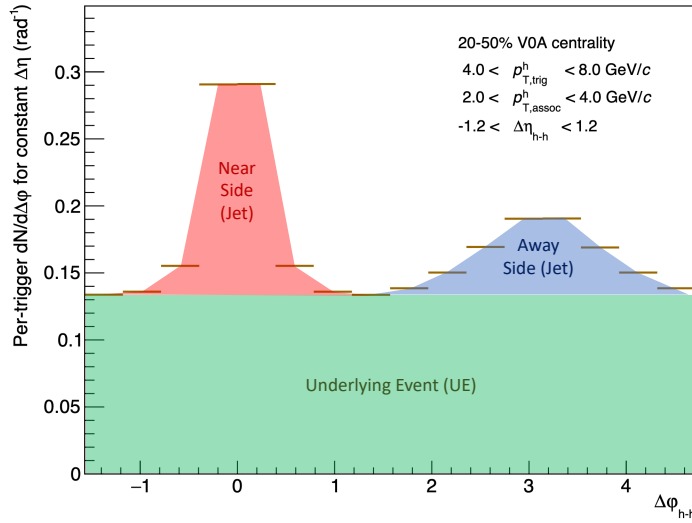


**Fig. 1:** A h-h  $\Delta\phi$  distribution taken from this analysis with the near-side, away-side, and uncorrelated regions highlighted.

## 1 Introduction

### 1.1 Motivation

Recent studies have shown that the ratio of the yield of  $\Lambda$  baryons to charged pions differs between pp, p-Pb and PbPb collisions, specifically in the mid- $p_T$  region of 1–4 GeV/c. Additionally, similar studies have seen an increase in the  $\Lambda/(\pi^+ + \pi^-)$  yields as a function of charged particle multiplicity in p-Pb collisions. The origin of this increase is still unknown.

By performing angular correlations of a high  $p_T$  trigger hadron with an associated  $\Lambda$  (or charged hadron as a proxy for a pion) in p-Pb events, we are able to separate out  $\Lambda$  baryon production into three distinct kinematic regions:

- The near-side peak of the correlation, corresponding to jet-like production with no medium interactions,
- The away-side peak of the correlation, corresponding to jet-like production with possible medium interaction, and
- The uncorrelated pairs, corresponding to the “underlying event” or soft production within the medium.

A h-h  $\Delta\phi$  distribution with these regions highlighted is shown in Figure ??.

For this study, 1-d  $\Delta\phi$  angular correlations of jet-like  $h - \Lambda$  and  $h - h$  pairs were measured in p-Pb events independently for three multiplicity bins (0-20%, 20-50%, 50-80%), and the final ratios of yields of correlated pairs were compared to study the onset of this enhancement.

### 1.2 Dataset and Event Selection

#### 1.2.1 Dataset

Every event in this analysis was a p-Pb collision at  $\sqrt{s_{NN}} = 5.02$  TeV taken from the following runlist which consists of 32 runs during the LHC16q period:

47 **265525, 265521, 265501, 265500, 265499, 265435, 265427, 265426, 265425, 265424, 265422, 265421,**  
 48 **265420, 265419, 265388, 265387, 265385, 265384, 265383, 265381, 265378, 265377, 265344, 265343,**  
 49 **265342, 265339, 265338, 265336, 265335, 265334, 265332, 265309**

50 This analysis uses the data from these runs with the FAST reconstruction, corresponding to approxi-  
 51 mately 400 million minimum bias events.

52 For the majority of the MC studies (MC method test, MC Closure test), the analysis was performed  
 53 using the standard purpose generated MC production LHC17f2b\_FAST, anchored to the LHC16q\_FAST  
 54 production. This production consists of around 30 million minimum bias events.

55 Larger statistics were needed to correct for a pairwise hadron- $\Lambda$  inefficiency due to track merging, which  
 56 was done using a template created from analyzing the standard purpose generated pp MC production  
 57 LHC18j2\_FAST, which is anchored to the LHC17q\_FAST production consisting of 15 TeV pp data. This  
 58 MC production contains around N million minimum bias events.

### 59 1.2.2 Event Selection

60 Events were selected by requiring a collision Z-vertex of less than 10 cm and at least 3 reconstructed  
 61 tracks in the event.

62 This reduces the total number of events (FAST + CENT\_wo\_SDD) considered to approximately 420  
 63 million events (see Table ??). The V0A estimator was chosen to determine event multiplicity percentile,  
 64 and the correlation measurement was performed in three multiplicity percentile bins: **0-20%, 20-50%,**  
 65 **and 50-80%.**

Multiplicity	Total Evt.	Has 3 Tracks	$ Z_{vtx}  < 10\text{cm} + 3 \text{ tracks}$	% Pass
0-20%	1.218E08	1.217E08	1.061E08	87.1%
20-50%	1.840E08	1.835E08	1.590E08	86.4%
50-80%	1.850E08	1.804E08	1.563E08	84.5%

**Table 1:** Number of events passing our criteria for each multiplicity bin considered.

66 For all events, the standard Physics selection with pile-up cuts was applied with AddTaskPhysicsSelection(kFALSE  
 67 kTRUE).

### 68 1.3 Code Locations

69 The code for this analysis can be found in the following locations:

70 *Correlations in Data and MC:*

- 71 – PWGLF/Strangeness/DPhi/AliAnalysisTaskLambdaHadronRatioV0 (for  $\Lambda$ s reconstructed using  
 72 V0 finder)
- 73 – PWGLF/Strangeness/DPhi/AliAnalysisTaskLambdaHadronRatioRes (for  $\Lambda$ s reconstructed using  
 74 resonance technique)

75 *Efficiency Computation:*

- 76 – PWGLF/Strangeness/DPhi/AliAnalysisTaskLambdaHadronEfficiency (for  $\Lambda$ s reconstructed using  
 77 V0 finder and resonance technique)

78 *MonteCarlo Closure Test*

- PWGLF/Strangeness/DPhi/AliAnalysisTaskLambdaHadronV0Closure (for  $\Lambda$ s reconstructed using V0 finder)
- PWGLF/Strangeness/DPhi/AliAnalysisTaskLambdaHadronResClosure (for  $\Lambda$ s reconstructed using resonance technique)

## 1.4 Relevant Contributions to ALICE Meetings

This analysis was presented at the following ALICE meetings, in reverse chronological order:

- Strangeness PAG Meeting: 10 January 2023 (<https://indico.cern.ch/event/1237832>)
- Strangeness PAG Meeting: 18 October 2022 (<https://indico.cern.ch/event/1211594>)
- Correlations PAG Meeting: 11 October 2022 (<https://indico.cern.ch/event/1210412>)
- Strangeness PAG Meeting: 4 October 2022 (<https://indico.cern.ch/event/1206673>)
- Resonance PAG Meeting: 17 November 2021 (<https://indico.cern.ch/event/1096156>)
- Strangeness PAG Meeting: 4 August 2020 (<https://indico.cern.ch/event/943026>)
- Correlations PAG Meeting: 26 June 2020 (<https://indico.cern.ch/event/903613>)
- Resonance PAG Meeting: 24 June 2020 (<https://indico.cern.ch/event/931429>)

## 2 Track Selection

### 2.1 Associated Hadron Track Cuts

For all associated hadrons, a minimum  $p_T$  cuts of  $p_T > 0.15$  GeV/c was applied. Additionally, an  $\eta$  cut of  $|\eta| < 0.8$  was required. Furthermore, all associated hadrons were required to meet the standard cuts supplied by `AliESDtrackCuts::GetStandardITSTPCTrackCuts2011()` corresponding to track filter bit 1024, with a modified number of `MinNClustersTPC` from the standard cut of 50:

- TPC Refit
- ITS Refit
- **SetMinNClustersTPC: 80**
- SetMaxChi2PerClusterTPC: 4
- SetAcceptKinkDaughters: kFALSE
- SetMaxDCAToVertexZ: 2
- SetMaxDCAToVertexXYPtDep:  $0.0105 + 0.0350/p_T^{1.1}$
- SetDCAToVertex2D: kFALSE
- SetMaxChi2TPCConstrainedGlobal: 36
- SetRequireSigmaToVertex: kFALSE
- SetMaxChi2PerClusterITS: 36

110 For the correlation, the associated hadron is selected only in the momentum region

$$1.0 < p_T < 4.0 \text{ GeV}/c,$$

111 with further binning performed offline. The  $p_T$ ,  $\phi$  and  $\eta$  distributions for the associated hadrons that  
112 pass these cuts in the 0-20% multiplicity bin can be seen in Figure ??.

## 113 2.2 $\Lambda$ Daughter Proton and Pion Track Cuts

114 The proton and the pion are required to have a minimum  $p_T$  of  $p_T > 0.15 \text{ GeV}/c$  and an  $\eta$  cut of  
115  $|\eta| < 0.8$ . Furthermore, the proton and pion are required to meet the following quality cuts:

- 116 – TPC refit flag enabled
- 117 – TPC crossed rows  $> 70$
- 118 – (TPC crossed rows)/(findable clusters)  $> 0.8$

119 All of these cuts are applied to the daughters of the reconstructed  $\Lambda$ , independent of the technique used  
120 for said reconstruction. For the correlation, the reconstructed  $\Lambda$  is selected only in the momentum region

$$1.0 < p_T < 4.0 \text{ GeV}/c,$$

121 with further binning performed offline.

## 122 2.3 Trigger Track Cuts

123 For the trigger hadron tracks, Hybrid Global constrained tracks were accepted using the cuts supplied by  
124 `IsHybridGlobalConstrainedGlobal()`, or track bit 768:

- 125 – `SetMinNClustersTPC`: 50
- 126 – `SetMaxChi2PerClusterTPC`: 4
- 127 – `SetAcceptKinkDaughters`: kFALSE
- 128 – `SetMaxDCAToVertexZ`: 3.2
- 129 – `SetMaxDCAToVertexXY`: 2.4
- 130 – `SetDCAToVertex2D`: kTRUE
- 131 – `SetMaxChi2TPCConstrainedGlobal`(36)
- 132 – `SetMaxFractionSharedTPCClusters`(0.4)

133 For the both the di-hadron and h- $\Lambda$  correlation, the trigger hadron is selected in the momentum region:

$$4.0 < p_T < 8.0 \text{ GeV}/c,$$

134 with further binning performed offline. The  $p_T$ ,  $\phi$  and  $\eta$  distributions for the trigger hadrons that pass  
135 these cuts in the 0-20% multiplicity bin can be seen in Figure ??.

### 3 $\Lambda$ Reconstruction

The  $\Lambda$  candidates were reconstructed through the  $\Lambda \rightarrow p\pi^-$  ( $\bar{\Lambda} \rightarrow \pi^+p$ ) decay channel with a branching ratio of 63.9%. For the majority of this analysis, the  $\Lambda$  and  $\bar{\Lambda}$  are combined together. Thus, unless otherwise specified,  $\Lambda = \Lambda + \bar{\Lambda}$ .

The  $\Lambda$  candidates in this analysis were reconstructed using two separate techniques:

- **V0 Finder Technique** - The V0 finder technique reconstructs the  $\Lambda$  by combining the proton and pion tracks with the V0 finder algorithm, which can be found within the AliROOT framework.
- **Resonance Technique** - The resonance technique combines all oppositely charged proton-pion pairs to reconstruct the  $\Lambda$ , resulting in maximal statistics at the cost of a large combinatorial background.

The central points in this analysis are from  $\Lambda$  candidates reconstructed using the V0 finder technique. The resonance technique serves as a powerful cross-check to ensure no topological biases are introduced within the V0 finder algorithm, and is investigated in detail in Section ??.

#### 3.1 V0 Selection

The central points in this analysis were generated using  $\Lambda$ s reconstructed using the V0-finder algorithm found within the AliROOT framework. All of the V0s found by the V0 finder algorithm were required to pass the following cuts:

- $p_T > 0.2 \text{ GeV}/c$
- $|\eta| < 0.8$
- On the fly status: disabled (offline V0s only)

There were no additional topological cuts applied to the V0s or their corresponding daughters. This was done to maximize statistics and to minimize any topological biases beyond those introduced by reconstructing  $\Lambda$ s using the V0-finder algorithm.

#### 3.2 V0 Daughter PID Cuts

The daughter protons and pions were required to meet the following PID cuts using both the TPC and TOF detectors:

- \*  $|n\sigma_{TPC,p}| < 2$
- \*  $|n\sigma_{TPC,\pi}| < 3$
- \*  $|n\sigma_{TOF,p}| < 2$  (if signal exists)
- \*  $|n\sigma_{TOF,\pi}| < 3$  (if signal exists)

The  $n\sigma$  values for both the TPC and TOF detectors of the daughter proton and pion are shown in Figure ?? and Figure ??, respectively. These values were obtained from the AOD tracks associated with every V0 found by the V0 finder algorithm, provided that those tracks also pass the aforementioned daughter track quality cuts.



To account for any biases introduced from choosing daughter tracks from the V0 finder algorithm, the TPC and TOF  $n\sigma_{p,\pi}$  distributions are shown for all AOD tracks in the tracklist in Figure ???. There are no major differences between the  $n\sigma$  distributions of the daughter tracks from the V0 finder algorithm and the AOD tracks in the tracklist. This indicates that the V0 finder algorithm is not introducing any biases in the PID selection of the daughter tracks. These plots also represent the PID cuts used for the resonance technique, which utilizes the full AOD track list and will be discussed in Section ??.

### 3.3 Invariant Mass Region

The invariant mass distributions in each multiplicity bin for the  $\Lambda$ s reconstructed using the V0 finder algorithm are shown in Figure ???. The  $\Lambda$  peak is clearly visible with almost zero background.

A Voigt (signal) + 2nd order polynomial (BG) fit was applied to the invariant mass distributions for each multiplicity bin. The extracted parameters from the Voigt fit are shown in Table ???. While the background is nearly zero for each multiplicity bin, its effect on the final correlation measurement is investigated in Section ??.

Multiplicity	A	$\mu$ (GeV/ $c^2$ )	$\sigma$ (GeV/ $c^2$ )	$\gamma$ (GeV/ $c^2$ )	$\chi^2/NDF$
0-20%	1.82e+02	1.116	1.24e-03	1.10e-03	31.24
20-50%	8.58e+01	1.116	1.24e-03	1.07e-03	15.55
50-80%	1.78e+01	1.116	1.23e-03	1.03e-03	4.55

**Table 2:** Parameters from the Voigt fit to the invariant mass distributions for the  $\Lambda$ s reconstructed using the V0 finder, along with the  $\chi^2/NDF$  for the total fit. The errors were negligible relative to the values.

Measuring the  $h - \Lambda$  correlation requires a clearly defined signal region for the unlike-sign  $p\pi$  pairs from the V0 finder. The signal region range is as follows:

$$\text{-- unlike-sign } p\pi \text{ in } \Lambda \text{ mass region: } 1.100 \text{ GeV}/c^2 < M_{p\pi} < 1.134 \text{ GeV}/c^2$$

This signal region was chosen to maximize statistical significance, and it does not depend on multiplicity. As it accounts for roughly 99.5% of the total signal, no correction for the tails of the distribution was applied. However, the choice of signal region and the corresponding correction factors are investigated more closely in Section ??.

## 4 Acceptance and Efficiency Corrections

This section details all of the detector acceptance and efficiency corrections applied to the central values of this analysis. All other corrections are discussed in Section ??.

### 4.1 Mixed Event Acceptance Correction

For each multiplicity bin, events were separated into z-vertex position bins with a width of 2 cm, ranging from  $-10$  cm to  $10$  cm. An AliEventPool of size 500 and track-depth 1000 was filled with a list of trigger tracks, then correlated with a list of associated hadrons (or  $p\pi$  pairs) for each event once the pool was ready. The pair-wise efficiency correction in Section ?? is also applied to the mixed event pairs. The uncorrected and mixed-event distributions ( $h$ - $p\pi$ ,  $h$ - $h$ ) for each multiplicity bin are shown in Figures ?? through ??.

For each multiplicity bin, the acceptance correction (as described in Eq. 1) was performed for each z-vertex bin, then the results were merged together to form the acceptance-corrected distributions, shown in Figures ?? through ???. Each plot was scaled by  $1/N_{trig}$ .

As this analysis relies on multiple angular correlations ( $h - \Lambda$ ,  $h - h$ ), the event mixing was done with a shared mixed event pool containing the list of trigger tracks, then the correlation was performed using the associated ( $p\pi$ ) or hadron list for each event. After mixing, each correlation was corrected using its corresponding mixed-event distribution. The event mixing was only performed on events that contained both a  $\Lambda$  candidate ( $p\pi$  pair from either V0 finder or global AOD list) and an associated hadron.

## 4.2 Reconstruction Efficiency

In this section we investigate the reconstruction efficiency of the  $\Lambda$ , trigger and associated hadrons.

### 4.2.1 $\Lambda$ Reconstruction Efficiency

To estimate the  $\Lambda$  reconstruction efficiency, we compare  $\Lambda$  yields reconstructed using the V0 finder to the true  $\Lambda$  yields using the MC production LHC17f2b\_FAST (anchored to LHC16q\_FAST production). The efficiency was calculated using the following formula:

$$\varepsilon_{\Lambda} = \frac{N_{\Lambda, \text{ reco with V0 finder}}}{N_{\Lambda, \text{ real MC yield}}},$$

where each  $\Lambda$  in  $N_{\Lambda, \text{ reco with V0 finder}}$  meets the following criteria:

- Found in the list of offline V0s
- $|\eta_{V0}| \leq 0.8$
- The daughter  $p, \pi$  pass the daughter track cuts outlined in Section ??
- The daughter  $p, \pi$  tracks have corresponding real  $p, \pi$  in the MC stack
- The corresponding MC stack  $p, \pi$  daughters come from the same mother  $\Lambda$  (also in MC stack)

and each  $\Lambda$  in  $N_{\Lambda, \text{ real MC yield}}$  meets the following criteria:

- Found in the MC stack
- $|\eta_{\Lambda}| \leq 0.8$
- The  $\Lambda$  decays to  $p\pi$

While previous analyses focus solely on primary  $\Lambda$ s (excluding  $\Omega$  and  $\Xi$  contamination), there is no requirement for either the V0-reconstructed  $\Lambda$  or the MC-generated  $\Lambda$  to be a primary particle. As this analysis is mostly interested in the  $\Lambda$  due to its strange quark content, whether or not the  $\Lambda$  came from a cascade decay is irrelevant. This is important to note when making comparisons between this analysis and previous analyses, as secondary contamination from cascades accounts for nearly 20% of all  $\Lambda$ s.

As mentioned in Section ??, both the  $\Lambda$  and the  $\bar{\Lambda}$  were combined together for this efficiency calculation. Efficiencies were calculated as a function of  $p_T$ ,  $\eta$ ,  $\phi$ , Event Z vertex, and Multiplicity. However, the final efficiency correction was applied as a function of  $p_T$  only and can be seen in Figure ??.

### 4.2.2 Trigger and Associated Hadron Reconstruction Efficiency

The trigger and associated hadron reconstruction efficiencies are calculated using the following formula:

$$\epsilon_{trig,assoc} = \frac{N_{trig,assoc, \text{ reco yield}}}{N_{trig,assoc, \text{ real MC yield}}},$$

where each trigger or associated hadron in  $N_{trig,assoc, \text{ reco yield}}$  meets the following criteria:

- Found in the list of AOD tracks
- $|\eta_{track}| \leq 0.8$
- The track passes the track cuts outlined in Section ?? (trigger) or ?? (associated)
- The track has a corresponding real track in the MC stack
- The corresponding MC track is either a pion, proton, kaon, electron or muon
- The corresponding MC track is not a secondary particle (`IsPhysicalPrimary() == true`)

and each trigger or associated hadron in  $N_{trig,assoc, \text{ real MC yield}}$  meets the following criteria:

- Found in the MC stack
- $|\eta_{track}| \leq 0.8$
- The track is either a pion, proton, kaon, electron or muon
- The track is not a secondary particle (`IsPhysicalPrimary() == true`)

The efficiencies for both the trigger and associated hadrons as a function of  $p_T$  are shown in Figure ??.

Because all of these efficiencies appear to be multiplicity independent, the final efficiency correction is performed using the integrated 0-100% points shown in red for each of the  $\Lambda$ , trigger and associated efficiency plots.

As our correlation measurement depends on both the trigger and associated particle, we must combine the two efficiencies to get the overall efficiency for the pair. This is done using the following formula:

$$\epsilon_{pair} = \epsilon_{trig} * \epsilon_{assoc}$$

This efficiency is corrected for on-the-fly as the pairs are being filled into the total correlation distribution by using a weighting factor equal to the inverse of  $\epsilon_{pair}$ . The same trigger efficiency used in the pair efficiency is then also to correct our  $N_{trig}$  for our final per-trigger correlation in both the h-h and h- $\Lambda$  case.

### 4.3 Track Merging Efficiency

Many correlation studies are susceptible to track merging inefficiencies, whereby either the trigger or associated particle gets merged over by the other during the track reconstruction. This results in a dip at small angles in the  $\Delta\eta\Delta\phi$  distribution when compared to a similar distribution with no instances of track merging. As this effect cannot be seen directly in data due to the missing reconstructed tracks, it was investigated using our MonteCarlo sample, where we can compare the reconstructed tracks with the MC generated particles they were reconstructed from. While this effect is usually negligible and only relevant at extremely small angles ( $\Delta\phi < 0.01, \Delta\eta < 0.1$ ), in this analysis we see that this effect is more severe and occurs at larger angles ( $\Delta\phi < 1, \Delta\eta < 0.6$ ), shown in Figure ??.

The severity of this effect is likely due to two factors:

- The  $\Lambda$  decay length is large ( $c\tau \approx 10$  cm), meaning the daughter particles will have less hits in the detector than the trigger particle (which is produced at the primary vertex). As Kalman filtering (track reconstruction) favors the track with more hits, the  $\Lambda$  daughter track is “merged” over by the trigger track.
- The  $\Lambda$  decay is assymmetric ( $m_p/m_\pi \approx 7$ ), so the  $\Lambda$  and daughter proton end up with similar momenta (and thus  $\phi$  and  $\eta$ ). This means that whenever a proton from a  $\Lambda$  decay is “merged” over by a trigger track, an  $h - \Lambda$  pair with small  $\Delta\phi, \Delta\eta$  is lost.

To see how the decay length can affect the track merging, we can measure the  $\Delta\phi$  distributions in the  $-1.2 < \Delta\eta < 1.2$  region for  $h$ -proton and  $h$ -pion pairs in our MonteCarlo sample where the proton/pion is secondary—meaning it came from a weak decay with decay length  $\ell \approx 2$  cm—and compare it to the same ratio for  $h$ -proton and  $h$ -pion pairs where the proton/pion is primary. The result is shown in Figures ?? (proton) and ??. All reconstructed triggers and protons are selected from the AOD track list and pass our trigger and daughter cuts from Sections ?? and ??, respectively (with the caveat being that the protons are required to have a corresponding entry in the MC stack and that entry is either secondary or primary). All distributions were corrected for detector acceptance using the procedure described in Section ??, and the baselines were scaled to each-other to emphasize this effect. We clearly observe a large suppression in the near side of the reconstructed distributions when compared to the ground truth for the  $h$ -secondary proton/pion case, but no significant suppression for the  $h$ -primary proton/pion case. As such, we conclude that this suppression is at least in part due to the decay length of the  $\Lambda$ , as all protons and pions that come from  $\Lambda$ s are secondaries (by a long shot).

Due to statistics, it is not possible to study the full  $\Delta\eta\Delta\phi$  distributions for the  $h$ -(secondary proton) case. However, the  $\Delta\eta\Delta\phi$  (reconstructed)/(ground truth) ratio for the  $h$ -(secondary pion) case is shown in Figure ??. Even with limited statistics, we can clearly observe a suppression ranging from around  $-0.8 < \Delta\phi < 0.8$  and  $-0.3 < \Delta\eta < 0.3$ .

We can also observe the  $p_T$  dependence of this effect by looking at the reconstructed and ground truth  $h$ -(secondary pion)  $\Delta\phi$  distributions in a low ( $0.15 < p_T < 2$ ) and high ( $2 < p_T < 4$ ) bin. The result is shown in Figure ??. We clearly observe a suppression in the near side of the reconstructed distribution for the high  $p_T$  bin, but not for the low  $p_T$  bin. This is consistent with the decay length dependence shown in the previous figures, as decay length is roughly proportional to  $p_T$ .

The  $p_T$  dependence of this inefficiency demonstrates why this effect is so severe in the  $h - \Lambda$  case (when compared analyses involving another secondary weak decay, like  $h - K^0$  from LUCIA\_ANALYSIS\_NOTE). Due to the asymmetry of the  $\Lambda$  decay ( $m_p/m_\pi \approx 7$ ), the daughter proton receives most of the momentum. Therefore when we are investigating  $h - \Lambda$  correlations within  $2 < p_{T,\Lambda} < 4$  GeV/c, any inefficiencies present in the corresponding  $h$ -(daughter proton) distribution with the same associated momentum would also be present in our final  $h - \Lambda$  distribution within the same  $\Delta\phi, \Delta\eta$  range. As we’ve demonstrated in

Figure ??, secondary charged protons with  $2 < p_T < 4$  GeV/c see a large inefficiency, and therefore we would expect a similar inefficiency to be present in our  $h - \Lambda$  distribution (which we've shown in Figure ??). Such an effect would not be as present in the  $h - K^0$  case with the same associated momentum, both because the decay length is much shorter (2 cm vs 10 cm), and the  $K^0$  decay is symmetric, meaning the daughter pions will have a momentum that is much lower than the mother (and therefore less affected by this inefficiency).

Due to the width of this inefficiency (in both  $\Delta\phi$  and  $\Delta\eta$ ) we were unable to correct for this effect using the following techniques:

- Applying a  $\Delta\phi^*$  correction, described DPHIS<sub>TAR<sub>P</sub>APER</sub>: While  $\Delta\phi$  and  $\Delta\phi^*$  are different, they are correlated enough that in order to remove this effect we had to cut on  $|\Delta\phi^*| < 0.7$ , which removes a significant amount of our near-side yield in the corresponding  $\Delta\phi$  distribution.
- Applying a cut on the minimum distance between the fully reconstructed helices of the trigger and  $\Lambda$  daughter proton (varied between 0.1 cm and 10 cm): Again, this cut removes roughly the same amount of near-side yield as the  $\Delta\phi^*$  cut, as this minimum distance is also highly correlated with  $\Delta\phi$ .

The most promising correction procedure is the one described in VICTOR\_ANALYSIS\_NOTE, which corrects for this inefficiency using a  $\Delta\eta\Delta\phi$  template generated from MonteCarlo. The formula for this correction is:

$$C_{corr.}(\Delta\phi, \Delta\eta) = C_{uncorr.}(\Delta\phi, \Delta\eta) \left( \frac{C_{reco.MC}(\Delta\phi, \Delta\eta)}{C_{real.MC}(\Delta\phi, \Delta\eta)} \right)^{-1}$$

where  $C_{corr.}$  is the corrected correlation,  $C_{uncorr.}$  is the uncorrected correlation, and  $\frac{C_{reco.MC}(\Delta\phi, \Delta\eta)}{C_{real.MC}(\Delta\phi, \Delta\eta)}$  is the angular efficiency template generated from MonteCarlo. This template is generated using the exact same procedure as our MonteCarlo closure tests (see Section ??) by taking the fully acceptance and efficiency-corrected reconstructed  $\Delta\eta\Delta\phi$  distribution and dividing it by the ground-truth  $\Delta\eta\Delta\phi$  distribution, and is shown in Figure ?. However, due to the limited statistics of our MonteCarlo sample (and that using a MonteCarlo sample that is not anchored to our data set would be unwise), we do not apply this correction to our final results. Instead, we apply a 10% systematic correction to our near-side yields for the  $h - \Lambda$  correlation (see Section ??). In the event that more statistics become available, we will revisit this correction.

## 5 Correlation Measurement Technique

### 5.1 Full Correlation Measurement Method

The per-trigger correlation is approximated for each multiplicity bin using the formula:

$$C_{trig}(\Delta\phi, \Delta\eta) = \frac{1}{N_{trig}} \frac{B(0,0) * S(\Delta\phi, \Delta\eta)}{B(\Delta\phi, \Delta\eta)} \quad (1)$$

where  $N_{trig}$  is the total number of hadrons in the  $4 < p_T < 8$  GeV/c range that pass our trigger cuts described in Section ??,  $S(\Delta\phi, \Delta\eta)$  is the efficiency-corrected (Section ??) same event correlation and  $B(\Delta\phi, \Delta\eta)$  is the mixed-event correlation. To properly account for the acceptance effects, the mixed-event distribution is scaled to the value of the  $(\Delta\phi = 0, \Delta\eta = 0)$  bin of the same event distribution.

However, what is actually measured is an angular correlation of  $h - (p\pi)$  pairs that is comprised of the real  $h - \Lambda$  signal as well as a background of  $h - (p\pi)$  pairs. The full correlation equation is then:

$$C_{h-\Lambda}(\Delta\phi, \Delta\eta) = r_{\text{Signal}} \left( C_{(h-p\pi)_{\text{Signal}}^{US}}(\Delta\phi, \Delta\eta) - r_{LS} * C_{(h-p\pi)_{\text{RSB}}^{US}}(\Delta\phi, \Delta\eta) \right) \quad (2)$$

Where each term is defined as follows:

- $C_{h-\Lambda}(\Delta\phi, \Delta\eta)$ : The final  $h - \Lambda$  correlation distribution
- $C_{(h-p\pi)_{\text{Signal}}^{US}}$ : The  $h - (p\pi)$  correlation in our signal region
- $C_{(h-p\pi)_{\text{RSB}}^{US}}(\Delta\phi, \Delta\eta)$ : The  $h - (p\pi)$  correlation in the right sideband region (RSB)
- $r_{\text{Signal}}$ : Scaling factor used to account for fraction of the  $h - \Lambda$  signal that is missed by choosing a finite signal region
- $r_{LS}$ : Scaling factor used to account for combinatorial background in the  $h - (p\pi)$  correlation

In our primary momentum bin ( $2 < p_T < 4$ ) for  $\Lambda$ s reconstructed using the V0 finder,  $r_{\text{Signal}}$  is nearly unity (1.001) and  $C_{(h-p\pi)_{\text{RSB}}^{US}}(\Delta\phi, \Delta\eta)$  is not used as our combinatorial background is negligible, thus the full correlation equation simplifies to (1). However, the full correlation equation (2) is used in the systematic uncertainty calculations (Section ??) as well as the  $h - \Lambda$  correlations where the  $\Lambda$  is reconstructed using the resonance technique (Section ??).

## 5.2 Full h- $\Lambda$ and h-h Correlation Measurement

Using Equation ?? and the efficiencies calculated in Section ??, we can plot the 2D and 1D angular correlations for both h- $\Lambda$  and  $h - h$  pairs, shown in Figures ?? through ?. Both the 2D and 1D correlations are such that  $|\Delta\eta| < 1.2$ .

## 5.3 Extracting Near-side, Away-side, and Underlying Event Yields

Once the  $\Delta\phi$  distributions are calculated, they are separated into the three kinematic regions discussed in Section ?. While this can be done in a multitude of ways, the central points of this analysis were calculated using the following technique (with other techniques discussed in Section ?):

### 6-bin underlying event technique:

- The underlying event region is defined using a straight-line fit of the average of bins (1, 2, 7, 8, 9, 16) in the  $\Delta\phi$  distribution
- The near-side yield is calculated via  $\sum_{i=1}^8 (\Delta\phi_{\text{bin } i} - UE_i)$ , where  $UE_i$  is the value of the straight-line fit at the center of the  $i$ th bin
- The away-side yield is calculated via  $\sum_{i=9}^{16} (\Delta\phi_{\text{bin } i} - UE_i)$ , where  $UE_i$  is the value of the straight-line fit at the center of the  $i$ th bin
- The underlying-event yield is calculated via  $\sum_{i=1}^{16} UE_i = 16 \times UE$
- The total-yield is calculated via  $\sum_{i=1}^{16} \Delta\phi_{\text{bin } i} = \text{near-side} + \text{away-side} + \text{underlying-event}$

The final per-trigger  $\Delta\phi$  distributions with the 6-bin UE fit for the  $h - \Lambda$  and  $h - h$  pairs in each multiplicity bin are shown in Figures ? and Figure ?, respectively.

## 5.4 Per-trigger Pairwise Yields

The  $h - \Lambda$  and  $h - h$  near-side, away-side, and underlying-event per-trigger pairwise yields for each multiplicity bin are shown in Table ?? ( $h - \Lambda$ ) and Table ?? ( $h - h$ ). The errors reported are the statistical errors on the yields. The systematic errors are discussed in Section ??.

Multiplicity Bin	Near-side Jet	Away-side Jet	Underlying Event	Total
0-20%	$3.90\text{e-}03 \pm 1.84\text{e-}04$	$4.42\text{e-}03 \pm 1.88\text{e-}04$	$8.75\text{e-}02 \pm 3.84\text{e-}04$	$9.58\text{e-}02 \pm 2.45\text{e-}04$
20-50%	$3.41\text{e-}03 \pm 1.52\text{e-}04$	$3.24\text{e-}03 \pm 1.54\text{e-}04$	$4.69\text{e-}02 \pm 3.11\text{e-}04$	$5.36\text{e-}02 \pm 2.02\text{e-}04$
50-80%	$2.72\text{e-}03 \pm 1.94\text{e-}04$	$2.80\text{e-}03 \pm 2.06\text{e-}04$	$2.44\text{e-}02 \pm 3.89\text{e-}04$	$2.99\text{e-}02 \pm 2.66\text{e-}04$

**Table 3:** Per-trigger pairwise  $h - \Lambda$  extracted yields and corresponding statistical errors in the different kinematic regions for each multiplicity bin. The yields were extracted using the same procedure described in the previous section.

Multiplicity Bin	Near-side Jet	Away-side Jet	Underlying Event	Total
0-20%	$3.54\text{e-}01 \pm 9.32\text{e-}04$	$2.28\text{e-}01 \pm 9.29\text{e-}04$	$3.63\text{e+}00 \pm 1.88\text{e-}03$	$4.21\text{e+}00 \pm 1.23\text{e-}03$
20-50%	$3.43\text{e-}01 \pm 8.49\text{e-}04$	$2.08\text{e-}01 \pm 8.38\text{e-}04$	$2.18\text{e+}00 \pm 1.65\text{e-}03$	$2.73\text{e+}00 \pm 1.12\text{e-}03$
50-80%	$3.40\text{e-}01 \pm 1.24\text{e-}03$	$1.99\text{e-}01 \pm 1.15\text{e-}03$	$1.24\text{e+}00 \pm 2.12\text{e-}03$	$1.78\text{e+}00 \pm 1.60\text{e-}03$

**Table 4:** Per-trigger pairwise  $h - h$  extracted yields and corresponding statistical errors in the different kinematic regions for each multiplicity bin. The yields were extracted using the same procedure described in the previous section.

In order to investigate the multiplicity dependence of jet-like  $\Lambda$  production, the  $h - \Lambda$  and  $h - h$  near-side and away-side per-trigger pairwise jet yields are plotted in Figure ?. The  $h - \Lambda$  yield appears to increase with respect to multiplicity, whereas the  $h - h$  yield appears mostly flat.

## 5.5 Multiplicity Dependent Ratio Measurement

Once we have extracted the per-trigger pairwise yields from our  $h - \Lambda$  and  $h - h$  correlations, we are able to measure the ratio of yields of  $h - \Lambda/h - h$  pairs in each of the kinematic regions described in the previous section—near-side of jet, away-side of jet, underlying event and total yield—as a function of multiplicity. This result of this can be seen in Figure ?.

Comparing the ratio in different kinematic regions as a function of multiplicity, we see a clear separation between the "jet-like" and "underlying event" components, with the underlying event seeing the largest  $\frac{h-\Lambda}{h-h}$  ratio in all multiplicity bins, whereas both the near-side and away-side ratios are lower than the total ratio for all multiplicity bins. We also see a clear separation between the near-side and away-side ratios, with the away-side ratio being higher than the near-side across all multiplicity bins. All kinematic region ratios see an increase with respect to multiplicity, but the underlying event ratio sees the smallest increase, while the away-side ratio sees the largest increase.

## 6 Systematic Errors

### 6.1 Systematics Overview

This analysis has two major components:

1. The generation of the  $h - \Lambda$  and  $h - h$   $\Delta\phi$  distributions
2. The extraction of the pairwise yields from the  $\Delta\phi$  distributions

As such, this Systematic Errors section is separated into two subsections, one for each of these components. In each section, we detail the different sources of systematic errors that we encounter, and how we account for them in our final results.

## 6.2 $\Delta\phi$ Distribution Generation

As our final yields depend on the  $\Delta\phi$  distributions, we must consider all of the sources of systematic errors that can appear during the generation of these distributions. These sources of systematic errors are as follows.

### 6.2.1 Signal Region Selection

While our central points of this analysis involve almost the entirety of our  $\Lambda$  signal region, the final result should not depend on which section of the signal region we choose. To investigate this, we vary the signal region in the following ways:

### 6.2.2 Signal Region Selection

While our central points of this analysis involve almost the entirety of our  $\Lambda$  signal region, the final result should not depend on which section of the signal region we choose. To investigate this, we vary the signal region in the following ways:

### 6.2.3 Background Subtraction

While we don't consider the combinatorial background from our V0-finder reconstructed  $\Lambda$ s in the central points of this analysis, its effect may still be present in our final correlation distribution. To investigate this effect, we perform a background subtraction procedure on the correlation distribution, similar to the one described in Section ???. Keeping the signal region fixed ( $1.100 < M_{p\pi} < 1.134 \text{ GeV}/c^2$ ), we vary the RSB region in the following ways:

### 6.2.4 Final Systematic Errors from $\Delta\phi$ Distribution Generation

The final systematic errors for the  $\Delta\phi$  distributions are calculated as follows:

- For each  $\Delta\phi$  bin, the result of each variation is divided by the central value to generate a list of ratios
- The RMS of the list of ratios in each  $\Delta\phi$  bin is calculated
- For each  $\Delta\phi$  bin, the systematic error is simply the RMS

As the sources of systematics discussed in this section do not affect our di-hadron distributions, we have assigned a systematic error of 4% to the di-hadron distributions for each  $\Delta\phi$  distribution as this matches the systematic errors from previous analyses of the same data set [?].

The  $h - \Lambda$  and  $h - h$   $\Delta\phi$  distributions with their systematic errors are shown in Figures ?? and ??, respectively. The statistical errors are not shown to emphasize the systematic errors, but they are included in the final results (Section ??)

## 6.3 Yield Extraction

The largest systematic error of this analysis corresponds to the different techniques that can be used to extract the yields in each kinematic region from the  $\Delta\phi$  distributions. We have already discussed the **6-bin underlying event technique** in Section ??, but we will also consider the following methods.



### 6.3.1 4-bin Underlying Event Technique

The 4-bin UE technique is very similar to the 6-bin UE technique, but we only select 4 bins to get an average for our UE baseline. The technique is as follows:

- The underlying event region is defined using a straight-line fit of the average of bins (1, 8, 9, 16) in the  $\Delta\phi$  distribution
- The near-side yield is calculated via  $\sum_{i=1}^8 (\Delta\phi_{\text{bin } i} - \text{UE}_i)$ , where  $\text{UE}_i$  is the value of the straight-line fit at the center of the  $i$ th bin
- The away-side yield is calculated via  $\sum_{i=9}^{16} (\Delta\phi_{\text{bin } i} - \text{UE}_i)$ , where  $\text{UE}_i$  is the value of the straight-line fit at the center of the  $i$ th bin
- The underlying-event yield is calculated via  $\sum_{i=1}^{16} \text{UE}_i = 16 \times \text{UE}$
- The total-yield is calculated via  $\sum_{i=1}^{16} \Delta\phi_{\text{bin } i} = \text{near-side} + \text{away-side} + \text{underlying-event}$

The final per-trigger  $\Delta\phi$  plots with the UE fit using the 4-bin UE technique are shown in Figures ?? ( $h - \Lambda$ ) and ?? ( $h - h$ ), and the extracted yields are shown in Table ?? ( $h - \Lambda$ ) and Table ?? ( $h - h$ ).

Multiplicity Bin	Near-side Jet	Away-side Jet	Underlying Event	Total
0-20%	$3.73\text{e-}03 \pm 1.91\text{e-}04$	$4.25\text{e-}03 \pm 1.94\text{e-}04$	$8.78\text{e-}02 \pm 4.72\text{e-}04$	$9.58\text{e-}02 \pm 2.45\text{e-}04$
20-50%	$3.47\text{e-}03 \pm 1.57\text{e-}04$	$3.30\text{e-}03 \pm 1.59\text{e-}04$	$4.68\text{e-}02 \pm 3.81\text{e-}04$	$5.36\text{e-}02 \pm 2.02\text{e-}04$
50-80%	$2.75\text{e-}03 \pm 2.00\text{e-}04$	$2.83\text{e-}03 \pm 2.12\text{e-}04$	$2.44\text{e-}02 \pm 4.73\text{e-}04$	$2.99\text{e-}02 \pm 2.66\text{e-}04$

**Table 5:** Per-trigger pairwise  $h - \Lambda$  extracted yields and corresponding statistical errors in the different kinematic regions for each multiplicity bin. The yields were extracted using the 4-bin technique described in this section.

Multiplicity Bin	Near-side Jet	Away-side Jet	Underlying Event	Total
0-20%	$3.56\text{e-}01 \pm 9.61\text{e-}04$	$2.30\text{e-}01 \pm 9.58\text{e-}04$	$3.62\text{e+}00 \pm 2.30\text{e-}03$	$4.21\text{e+}00 \pm 1.23\text{e-}03$
20-50%	$3.42\text{e-}01 \pm 8.74\text{e-}04$	$2.08\text{e-}01 \pm 8.63\text{e-}04$	$2.18\text{e+}00 \pm 2.02\text{e-}03$	$2.73\text{e+}00 \pm 1.12\text{e-}03$
50-80%	$3.38\text{e-}01 \pm 1.27\text{e-}03$	$1.96\text{e-}01 \pm 1.18\text{e-}03$	$1.24\text{e+}00 \pm 2.61\text{e-}03$	$1.78\text{e+}00 \pm 1.60\text{e-}03$

**Table 6:** Per-trigger pairwise  $h - h$  extracted yields and corresponding statistical errors in the different kinematic regions for each multiplicity bin. The yields were extracted using the 4-bin technique described in this section.

### 6.3.2 ZYAM Underlying Event Technique

The ZYAM (Zero Yield At Minimum) underlying event technique is a modification of the 4 and 6 bin techniques, whereby we only take the minimum bin value in the  $\Delta\phi$  distribution as the underlying event value. The full technique is as follows:

- The underlying event region is defined using a straight-line fit with value and error set to the value and error of the minimum bin in the  $\Delta\phi$  distribution
- The near-side yield is calculated via  $\sum_{i=1}^8 (\Delta\phi_{\text{bin } i} - \text{UE}_i)$ , where  $\text{UE}_i$  is the value of the straight-line fit at the center of the  $i$ th bin
- The away-side yield is calculated via  $\sum_{i=9}^{16} (\Delta\phi_{\text{bin } i} - \text{UE}_i)$ , where  $\text{UE}_i$  is the value of the straight-line fit at the center of the  $i$ th bin
- The underlying-event yield is calculated via  $\sum_{i=1}^{16} \text{UE}_i = 16 \times \text{UE}$
- The total-yield is calculated via  $\sum_{i=1}^{16} \Delta\phi_{\text{bin } i} = \text{near-side} + \text{away-side} + \text{underlying-event}$

The final per-trigger  $\Delta\phi$  plots with the UE fit using the ZYAM UE technique are shown in Figures ?? ( $h - \Lambda$ ) and ?? ( $h - h$ ), and the extracted yields are shown in Table ?? ( $h - \Lambda$ ) and Table ?? ( $h - h$ ).

Multiplicity Bin	Near-side Jet	Away-side Jet	Underlying Event	Total
0-20%	$4.71\text{e-}03 \pm 2.37\text{e-}04$	$5.23\text{e-}03 \pm 2.40\text{e-}04$	$8.58\text{e-}02 \pm 9.28\text{e-}04$	$9.58\text{e-}02 \pm 2.45\text{e-}04$
20-50%	$3.98\text{e-}03 \pm 1.95\text{e-}04$	$3.81\text{e-}03 \pm 1.96\text{e-}04$	$4.58\text{e-}02 \pm 7.56\text{e-}04$	$5.36\text{e-}02 \pm 2.02\text{e-}04$
50-80%	$3.55\text{e-}03 \pm 2.44\text{e-}04$	$3.63\text{e-}03 \pm 2.54\text{e-}04$	$2.28\text{e-}02 \pm 9.26\text{e-}04$	$2.99\text{e-}02 \pm 2.66\text{e-}04$

**Table 7:** Per-trigger pairwise  $h - \Lambda$  extracted yields and corresponding statistical errors in the different kinematic regions for each multiplicity bin. The yields were extracted using the ZYAM technique described in this section.

Multiplicity Bin	Near-side Jet	Away-side Jet	Underlying Event	Total
0-20%	$3.82\text{e-}01 \pm 1.19\text{e-}03$	$2.56\text{e-}01 \pm 1.18\text{e-}03$	$3.57\text{e+}00 \pm 4.57\text{e-}03$	$4.21\text{e+}00 \pm 1.23\text{e-}03$
20-50%	$3.62\text{e-}01 \pm 1.07\text{e-}03$	$2.28\text{e-}01 \pm 1.06\text{e-}03$	$2.14\text{e+}00 \pm 4.00\text{e-}03$	$2.73\text{e+}00 \pm 1.12\text{e-}03$
50-80%	$3.58\text{e-}01 \pm 1.49\text{e-}03$	$2.16\text{e-}01 \pm 1.42\text{e-}03$	$1.20\text{e+}00 \pm 5.13\text{e-}03$	$1.78\text{e+}00 \pm 1.60\text{e-}03$

**Table 8:** Per-trigger pairwise  $h - h$  extracted yields and corresponding statistical errors in the different kinematic regions for each multiplicity bin. The yields were extracted using the ZYAM technique described in this section.

### 6.3.3 Full 1D Correlation Fit

The full 1D correlation fit involves fitting the entire  $\Delta\phi$  distribution with a function that includes near-side, away-side and underlying-event components. The fit function is given by:

$$\begin{aligned} \text{Fit}(\Delta\phi) = & C + A_{\text{near}} * \exp \frac{(\Delta\phi - M_{\text{near}})^2}{2 * \sigma_{\text{near}}} + A_{\text{away}} * \exp \frac{(\Delta\phi - M_{\text{away}})^2}{2 * \sigma_{\text{away}}} \\ & + (A_{\text{near,mirror}} * \exp \frac{((\Delta\phi + 2\pi) - M_{\text{near,mirror}})^2}{2 * \sigma_{\text{near,mirror}}} + A_{\text{away,mirror}} * \exp \frac{((\Delta\phi - 2\pi) - M_{\text{away,mirror}})^2}{2 * \sigma_{\text{away,mirror}}}) \end{aligned}$$

where the “mirror” terms are added to account for the  $2\pi$  periodicity of the  $\Delta\phi$  distribution. The mean in the near-side gaussian (and corresponding mirror term) is fixed to 0 ( $2\pi$ ) and the mean in the away-side gaussian (and corresponding mirror term) is fixed to  $\pi$  ( $-\pi$ ), but all other parameters are allowed to vary. The yield extraction procedure is as follows:

- The  $\Delta\phi$  distribution is fit with the correlation function described above in the range  $-\frac{\pi}{2} < \Delta\phi < \frac{3\pi}{2}$
- The near-side yield is calculated via  $\frac{16}{2\pi} (\int_{-\frac{\pi}{2}}^{\frac{\pi}{2}} \text{Fit}(\Delta\phi) d\Delta\phi - \int_{-\frac{\pi}{2}}^{\frac{\pi}{2}} \text{UE} d\Delta\phi)$ , where UE is a constant calculated from the average of bins (1, 2, 7, 8, 9, 16)
- The away-side yield is calculated via  $\frac{16}{2\pi} (\int_{\frac{\pi}{2}}^{\frac{3\pi}{2}} \text{Fit}(\Delta\phi) d\Delta\phi - \int_{\frac{\pi}{2}}^{\frac{3\pi}{2}} \text{UE} d\Delta\phi)$
- The underlying-event yield is calculated via  $\frac{16}{2\pi} \int_{-\frac{\pi}{2}}^{\frac{3\pi}{2}} \text{UE} d\Delta\phi$
- The total yield is calculated via  $\frac{16}{2\pi} \int_{-\frac{\pi}{2}}^{\frac{3\pi}{2}} \text{Fit}(\Delta\phi) d\Delta\phi$

The constant  $\frac{16}{2\pi}$  being multiplied by each term is just the inverse of the bin width ( $2\pi$  radians for 16  $\Delta\phi$  bins). The final per-trigger  $\Delta\phi$  plots with the full correlation fits are shown in Figures ?? ( $h - \Lambda$ ) and ?? ( $h - h$ ), and the extracted yields are shown in Table ?? ( $h - \Lambda$ ) and Table ?? ( $h - h$ ).

### 6.3.4 6-bin Underlying Event Technique With Non-Negative Constraint

We again consider the 6-bin underlying event technique, but we restrict that each term in  $\sum_{i=1}^8 (\Delta\phi_{\text{bin } i} - \text{UE}_i)$  (near-side yield) and  $\sum_{i=9}^{16} (\Delta\phi_{\text{bin } i} - \text{UE}_i)$  (away side yield) is non-negative. The full technique is as follows:

Multiplicity Bin	Near-side Jet	Away-side Jet	Underlying Event	Total
0-20%	3.96e-03	4.35e-03	8.75e-02	9.58e-02
20-50%	3.40e-03	3.24e-03	4.69e-02	5.36e-02
50-80%	2.80e-03	2.65e-03	2.44e-02	2.99e-02

**Table 9:** Per-trigger pairwise  $h - \Lambda$  extracted yields in the different kinematic regions for each multiplicity bin. The yields were extracted using the full correlation fit procedure described in this section.

Multiplicity Bin	Near-side Jet	Away-side Jet	Underlying Event	Total
0-20%	3.54e-01	2.27e-01	3.63e+00	4.21e+00
20-50%	3.44e-01	2.08e-01	2.18e+00	2.73e+00
50-80%	3.42e-01	1.97e-01	1.24e+00	1.78e+00

**Table 10:** Per-trigger pairwise  $h - h$  extracted yields in the different kinematic regions for each multiplicity bin. The yields were extracted using the full correlation fit procedure described in this section.

- The underlying event region is defined using a straight-line fit of the average of bins (1, 2, 7, 8, 9, 16) in the  $\Delta\phi$  distribution
- The near-side yield is calculated via  $\sum_{i=1}^8 (\Delta\phi_{\text{bin } i} - \text{UE}_i)$ , where  $\text{UE}_i$  is the value of the straight-line fit at the center of the  $i$ th bin and all negative terms in the sum are manually set to zero
- The away-side yield is calculated via  $\sum_{i=9}^{16} (\Delta\phi_{\text{bin } i} - \text{UE}_i)$ , where  $\text{UE}_i$  is the value of the straight-line fit at the center of the  $i$ th bin and all negative terms in the sum are manually set to zero
- The underlying-event yield is calculated via  $\sum_{i=1}^{16} \text{UE}_i = 16 \times \text{UE}$
- The total-yield is calculated via  $\sum_{i=1}^{16} \Delta\phi_{\text{bin } i} = \text{near-side} + \text{away-side} + \text{underlying-event}$

As this method doesn't change the UE fit line in any way, we report only the extracted yields in Table ?? ( $h - \Lambda$ ) and Table ?? ( $h - h$ ). (If you would like a reminder of the  $\Delta\phi$  plots with 6-bin UE fits, see Figures ?? ( $h - \Lambda$ ) and ?? ( $h - h$ ))

Multiplicity Bin	Near-side Jet	Away-side Jet	Underlying Event	Total
0-20%	$4.14\text{e-}03 \pm 1.84\text{e-}04$	$4.42\text{e-}03 \pm 1.88\text{e-}04$	$8.75\text{e-}02 \pm 3.84\text{e-}04$	$9.58\text{e-}02 \pm 2.45\text{e-}04$
20-50%	$3.50\text{e-}03 \pm 1.52\text{e-}04$	$3.27\text{e-}03 \pm 1.54\text{e-}04$	$4.69\text{e-}02 \pm 3.11\text{e-}04$	$5.36\text{e-}02 \pm 2.02\text{e-}04$
50-80%	$2.93\text{e-}03 \pm 1.94\text{e-}04$	$2.80\text{e-}03 \pm 2.06\text{e-}04$	$2.44\text{e-}02 \pm 3.89\text{e-}04$	$2.99\text{e-}02 \pm 2.66\text{e-}04$

**Table 11:** Per-trigger pairwise  $h - \Lambda$  extracted yields and corresponding statistical errors in the different kinematic regions for each multiplicity bin. The yields were extracted using the 6-bin UE technique with non-negative constraint described in this section.

Multiplicity Bin	Near-side Jet	Away-side Jet	Underlying Event	Total
0-20%	$3.60\text{e-}01 \pm 9.32\text{e-}04$	$2.28\text{e-}01 \pm 9.29\text{e-}04$	$3.63\text{e+}00 \pm 1.88\text{e-}03$	$4.21\text{e+}00 \pm 1.23\text{e-}03$
20-50%	$3.48\text{e-}01 \pm 8.49\text{e-}04$	$2.08\text{e-}01 \pm 8.38\text{e-}04$	$2.18\text{e+}00 \pm 1.65\text{e-}03$	$2.73\text{e+}00 \pm 1.12\text{e-}03$
50-80%	$3.46\text{e-}01 \pm 1.24\text{e-}03$	$1.99\text{e-}01 \pm 1.15\text{e-}03$	$1.24\text{e+}00 \pm 2.12\text{e-}03$	$1.78\text{e+}00 \pm 1.60\text{e-}03$

**Table 12:** Per-trigger pairwise  $h - h$  extracted yields and corresponding statistical errors in the different kinematic regions for each multiplicity bin. The yields were extracted using the 6-bin UE technique with non-negative constraint described in this section.

### 6.3.5 $v_2$ Background Technique

All of the aforementioned yield extraction techniques rely on the assumption that the background is flat. This assumption would not be valid in the presence of a non-zero  $v_2$ , thus we must perform an additional

check to ensure that a non-zero  $v_2$  does not have a significant effect on our yield extraction and therefore final ratio measurement. To do this, we use the single-particle p-Pb  $v_2$  of the  $\Lambda$  and charged hadrons, found in this Analysis Note: [?]. The values were taken as an average over the  $2 < p_T < 4$  GeV/c bins for the  $\Lambda$  and associated hadron, and the  $4 < p_T < 6$  GeV/c bins for the trigger hadron (there was no data up to 8 GeV, but the  $v_2$  is mostly flat at higher  $p_T$  anyway). The  $v_2$  values in the 0-20% multiplicity bin are as follows:

- $\Lambda$ : 0.155
- Associated hadron: 0.150
- Trigger hadron: 0.190

As there is no published data corresponding to the multiplicity bins chosen in this analysis, the  $v_2$  values in the 20-50% and 50-80% bins are taken as 85% and 50% of the 0-20% values, respectively. Using these  $v_2$  values, we extract the yields using the following method:

- Let  $Fit_{v_2}(\Delta\phi) = UE \times (1 + 2(v_{2,trig}v_{2,assoc})(\frac{1}{2} + \cos(2\Delta\phi)))$ , where UE is the average of bins (1, 2, 7, 8, 9, 16) in the  $\Delta\phi$  distribution
- The near-side yield is calculated via  $\sum_{i=1}^8 (\Delta\phi_{bin\ i} - Fit_{v_2,bin\ i})$ , where  $Fit_{v_2,bin\ i}$  is the value of  $Fit_{v_2}$  at the center of the  $i$ th  $\Delta\phi$  bin
- The away-side yield is calculated via  $\sum_{i=8}^{16} (\Delta\phi_{bin\ i} - Fit_{v_2,bin\ i})$
- The underlying-event yield is calculated via  $\frac{16}{2\pi} \int_{-\frac{\pi}{2}}^{\frac{3\pi}{2}} Fit_{v_2} d\Delta\phi$
- The total-yield is calculated via  $\sum_{i=1}^{16} \Delta\phi_{bin\ i} = \text{near-side} + \text{away-side} + \text{underlying-event}$

The constant  $\frac{16}{2\pi}$  being multiplied by the underlying event integral term is just the inverse of the bin width (2 $\pi$  radians for 16  $\Delta\phi$  bins). The final per-trigger  $\Delta\phi$  plots with the  $v_2$  fits are shown in Figures ?? ( $h - \Lambda$ ) and ?? ( $h - h$ ), and the extracted yields are shown in Table ?? ( $h - \Lambda$ ) and Table ?? ( $h - h$ ).

Multiplicity Bin	Near-side Jet	Away-side Jet	Underlying Event	Total
0-20%	3.90e-03	4.42e-03	8.75e-02	9.58e-02
20-50%	3.41e-03	3.24e-03	4.69e-02	5.36e-02
50-80%	2.72e-03	2.80e-03	2.44e-02	2.99e-02

**Table 13:** Per-trigger pairwise  $h - \Lambda$  extracted yields in the different kinematic regions for each multiplicity bin. The yields were extracted using the  $v_2$  fit procedure described in this section. Despite the optically large contribution from  $v_2$  in the most central multiplicity bin, the extracted yields are still very similar to the other techniques.

Multiplicity Bin	Near-side Jet	Away-side Jet	Underlying Event	Total
0-20%	3.54e-01	2.28e-01	3.63e+00	4.21e+00
20-50%	3.43e-01	2.08e-01	2.18e+00	2.73e+00
50-80%	3.40e-01	1.99e-01	1.24e+00	1.78e+00

**Table 14:** Per-trigger pairwise  $h - h$  extracted yields in the different kinematic regions for each multiplicity bin. The yields were extracted using the  $v_2$  fit procedure described in this section.

### 6.3.6 Additional Systematics for Yield Extraction

Track Merging As mentioned in Section ??, the track merging effect causes an 8% loss in the  $h - \Lambda$  near-side yield extraction. Because we were unable to generate a template in MonteCarlo with enough statistics to correct for this effect, we have assigned an assymmetric (above central value) 10% systematic error to the near-side yields of our  $h - \Lambda$  distributions.

### 6.3.7 Final Systematic Errors from Yield Extraction

The final systematic errors for the yield extraction are calculated in the following way:

- For every extraction technique, the yield in a given kinematic region is divided by the yield in the same region using our default technique (6-bin UE)
- The RMS of the resulting ratios in each kinematic region is calculated
- For the near-side, 1/2 the RMS is added in quadrature with our track-merging systematic error (10%), which gives the upper side of the systematic error. The lower side is simply 1/2 the RMS.
- For the rest of the regions, the systematic error is simply the RMS

The final systematic errors from the yield extraction in each kinematic region and multiplicity bin can be seen in Table ??.

Multiplicity Bin	Near-side Jet	Away-side Jet	Underlying Event	Total
0-20%	$3.60\text{e-}01 \pm 9.32\text{e-}04$	$2.28\text{e-}01 \pm 9.29\text{e-}04$	$3.63\text{e+}00 \pm 1.88\text{e-}03$	$4.21\text{e+}00 \pm 1.23\text{e-}03$
20-50%	$3.48\text{e-}01 \pm 8.49\text{e-}04$	$2.08\text{e-}01 \pm 8.38\text{e-}04$	$2.18\text{e+}00 \pm 1.65\text{e-}03$	$2.73\text{e+}00 \pm 1.12\text{e-}03$
50-80%	$3.46\text{e-}01 \pm 1.24\text{e-}03$	$1.99\text{e-}01 \pm 1.15\text{e-}03$	$1.24\text{e+}00 \pm 2.12\text{e-}03$	$1.78\text{e+}00 \pm 1.60\text{e-}03$

**Table 15:** Final systematic errors from the yield extraction in each kinematic region and multiplicity bin. The systematic errors are calculated using the method described in this section.

## 6.4 Summarizing Plots

A plot summarizing all of the systematic errors contributing to the  $h - \Lambda$  and  $h - h \Delta\phi$  distributions for each multiplicity bin can be seen in Figure ??.

A plot summarizing all of the systematic errors contributing to the  $h - \Lambda$  and  $h - h$  pairwise yield extractions for each multiplicity bin and kinematic region can be seen in Figure ??.

## 7 Results and Comparisons

### 7.1 Per-trigger $h - \Lambda$ , $h - h \Delta\phi$ Correlations

### 7.2 $h - \Lambda$ , $h - h$ Jet-like Yields

### 7.3 Multiplicity Dependent $h - \Lambda/(h - h)$ Ratios

### 7.4 Additional Momentum Bin Measurements

In order to gain more insight into the  $\Lambda$  production in jets vs. the underlying event, we can also split the associated momentum bins into a high  $p_T$  bin ( $2.5 < p_T < 4.0 \text{ GeV}/c$ ) and a low  $p_T$  bin ( $1.5 < p_T < 2.5 \text{ GeV}/c$ ). The correlation analysis is performed for these two separate momentum bins exactly as laid out in Section 4, and is done for both  $h - \Lambda$  and  $h - h$  correlated pairs. The results for the final  $\Delta\phi$  distributions are shown in Figures ?? (low  $p_T$  bin) and ?? (high  $p_T$  bin).

By comparing the ratio of  $(h - \Lambda)/(h - h)$  pairs in these two different momentum regions (Figures ?? (low) and ?? (high)), we still see the clear separation between the jet-like production and the underlying event production. We also observe a similar increase in the  $h - \Lambda/h - h$  ratio as a function of multiplicity in both momentum bins. However, the increase in the UE and total ratios appear to be enhanced within the higher  $p_T$  bin when compared with the lower  $p_T$  bin.

The lower momentum bin also sees a steeper increase in the ratio within the away-side jet as a function of multiplicity, hinting that jet-medium interactions in the low momentum region may be causing the away-side  $h - \Lambda/h - h$  ratio to approach the underlying event ratio at high multiplicity.

The per-trigger pairwise yields for both momentum bins can be seen in Figures ?? (low) and ?? (high). We observe similar trends across both momentum bins, including a much larger increase in both jet-like components of the  $h - \Lambda$  yields when compared to the  $h - h$  yields, which appear mostly flat in both  $p_T$  bins. However, the lower momentum bin sees moderate tension between the near and away-side yields of the  $h - \Lambda$  pairs, with the away-side production appearing to be slightly higher than the near-side production across all multiplicity bins. This may also be a hint that  $\Lambda$  production is being enhanced via jet-medium interactions.

## 7.5 Comparison to the $\phi(1020)$

## 7.6 Multiplicity Dependent $h - \Lambda/h - \phi$ Ratios

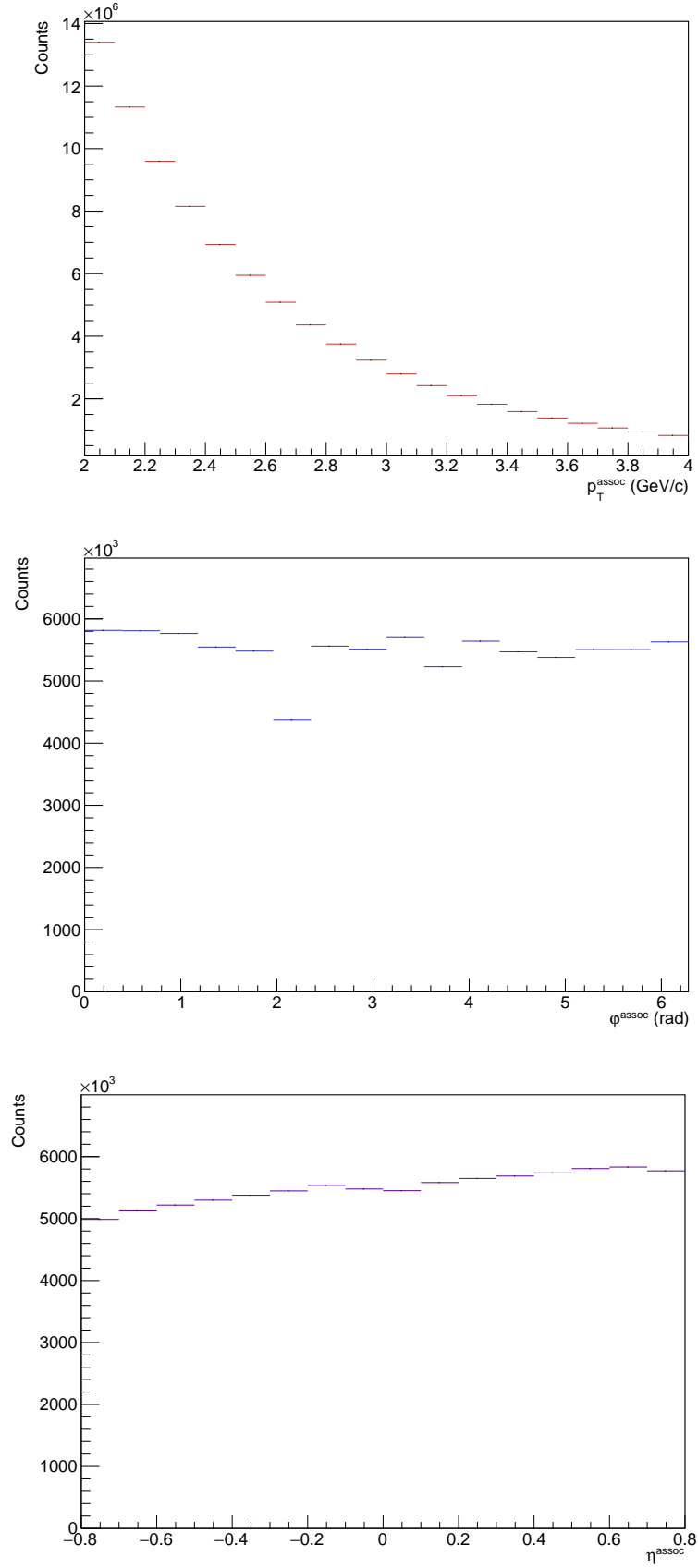


**Fig. 2:** The  $p_T$  (top),  $\phi$  (center) and  $\eta$  (bottom) distributions for the associated hadrons in the multiplicity range 0-20%.

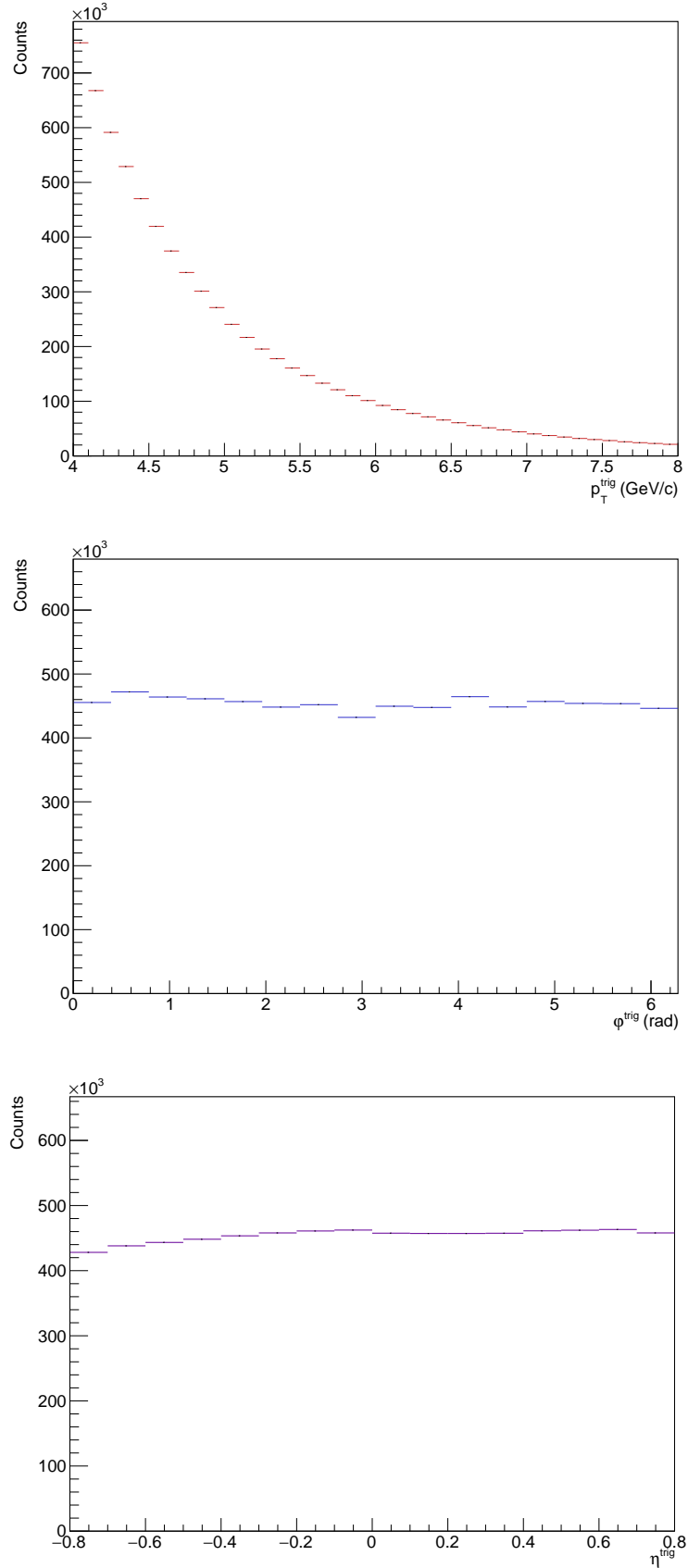


**Fig. 3:** The  $p_T$  (top),  $\phi$  (center) and  $\eta$  (bottom) distributions for the trigger hadrons in the multiplicity range 0-20%. Note that the  $\phi$  and  $\eta$  distributions are uniform, indicating no geometric biases from track selection (TPC sector bounds, etc.) will be introduced into the angular correlations.



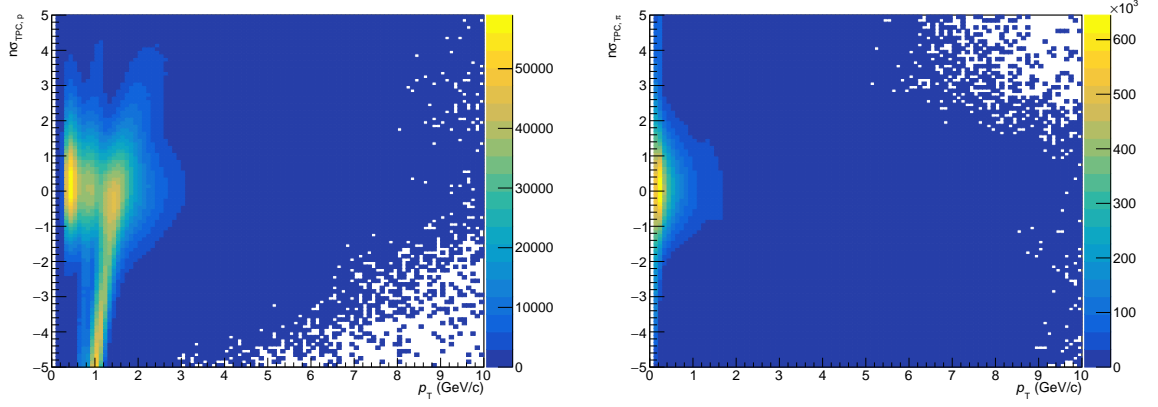


**Fig. 4:**  $n\sigma$  for protons (left) and pions (right) in the TPC detector as a function of  $p_T$ . A wider PID cut is used for the pion to maximize the  $\Lambda$  signal.

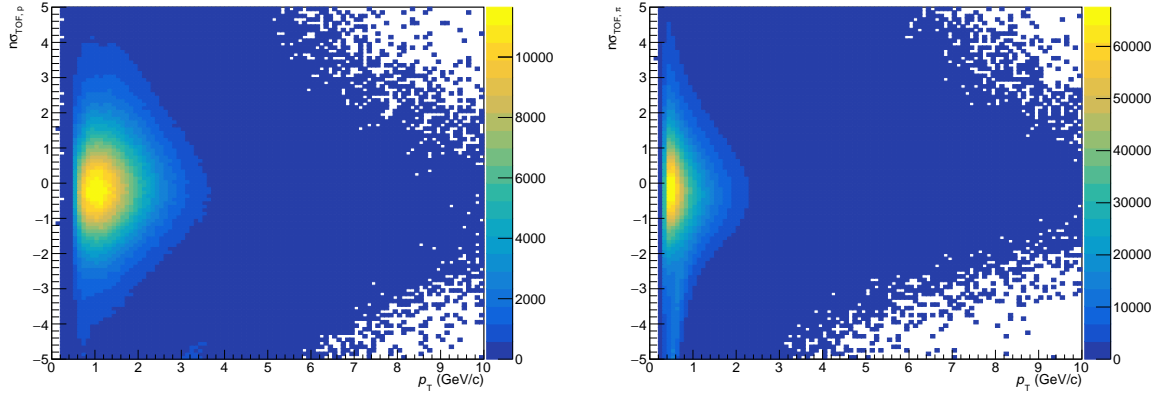


**Fig. 5:**  $n\sigma$  for pions (left) and protons (right) in the TOF detector as a function of  $p_T$ . If there is no TOF signal for the track, the TOF PID cut is not applied.

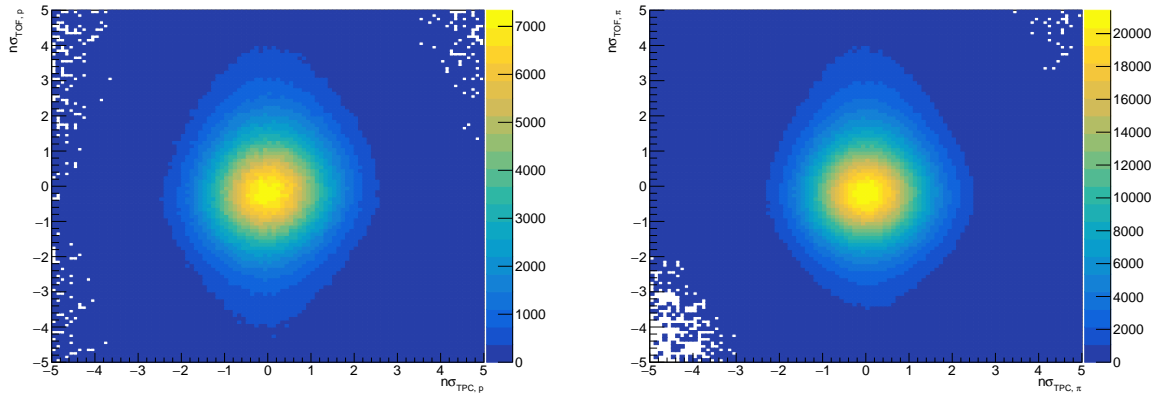


**Fig. 6:**  $n\sigma$  in TOF vs  $n\sigma$  in TPC for protons (left) and pions (right). No contamination is observed for both of the particle species.

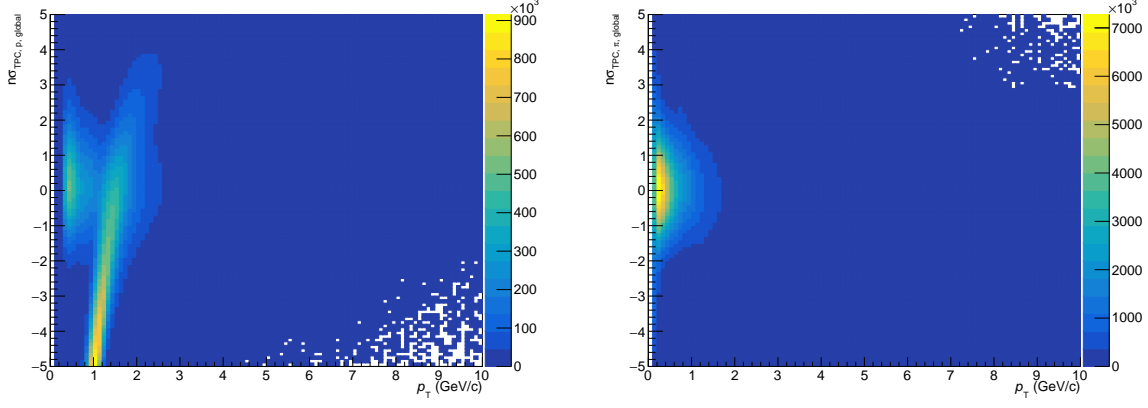


**Fig. 7:**  $n\sigma$  for protons (left) and pions (right) from the global AOD track list in the TPC detector as a function of  $p_T$ . These plots are very similar to those generated from V0 daughter tracks, so we conclude no PID biases are introduced from the V0 finder method.

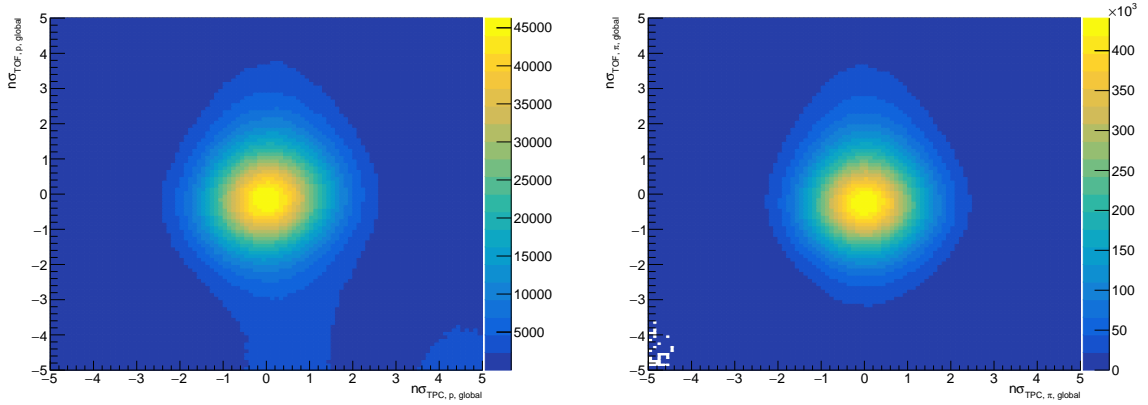


**Fig. 8:**  $n\sigma$  for protons (left) and pions (right) from the global AOD track list in the TOF detector as a function of  $p_T$ . Little to no contamination is observed.

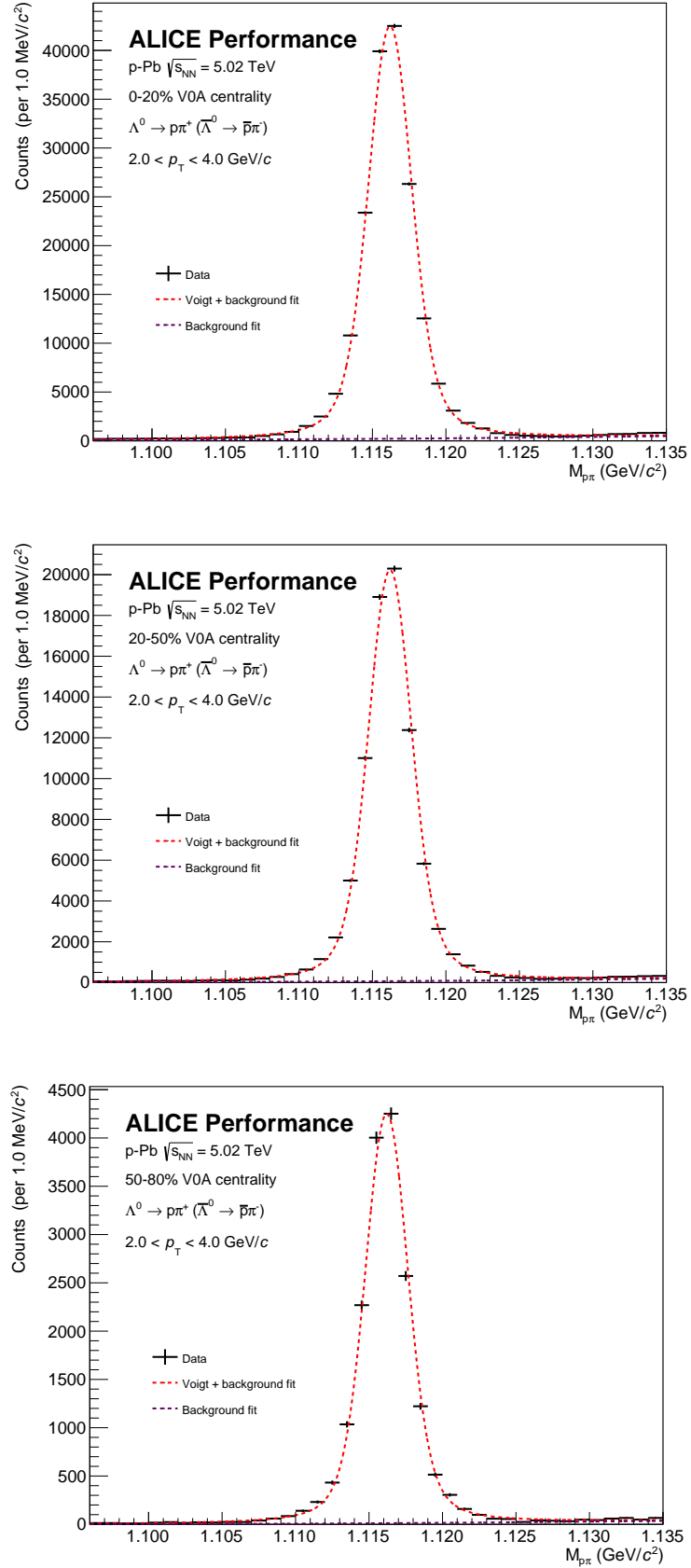


**Fig. 9:** Invariant mass distributions in the 0-20% (top), 20-50% (center), and 50-80% (bottom) multiplicity bins for  $\Lambda$ s reconstructed using the V0 finder with  $2 < p_T < 4$ . The background from misidentified  $\Lambda$ s is negligible for all multiplicity bins, despite no topological cuts being applied to the V0s.

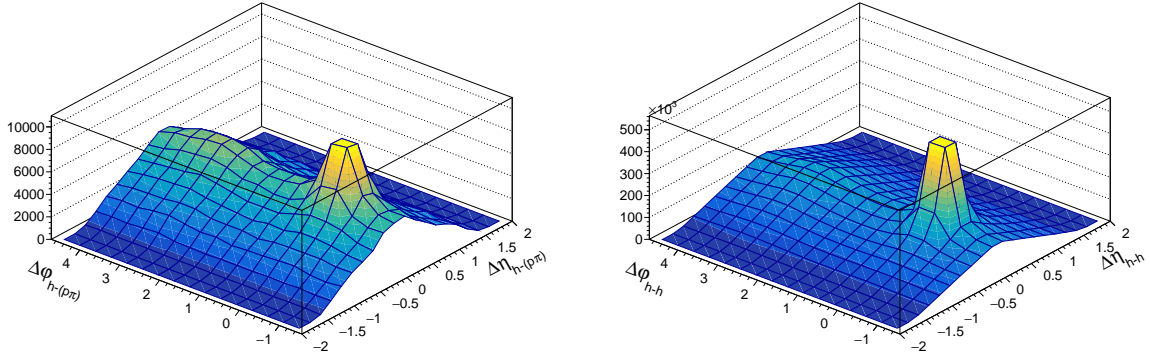


**Fig. 10:** 2-D non-acceptance corrected h- $p\pi$  (left) and h-h (right) angular correlations for the 0-20% multiplicity bin (all z-vertex bins merged together)

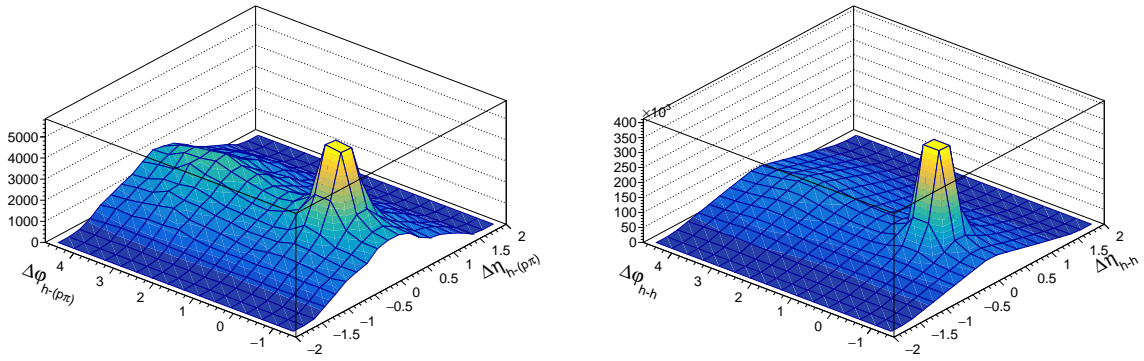


**Fig. 11:** 2-D non-acceptance corrected h- $p\pi$  (left) and h-h (right) angular correlations for the 20-50% multiplicity bin (all z-vertex bins merged together)

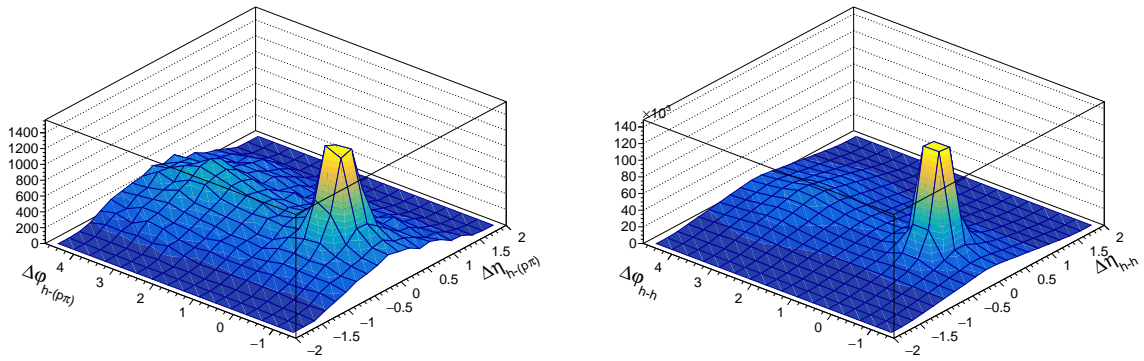


**Fig. 12:** 2-D non-acceptance corrected h- $p\pi$  (left) and h-h (right) angular correlations for the 50-80% multiplicity bin (all z-vertex bins merged together)

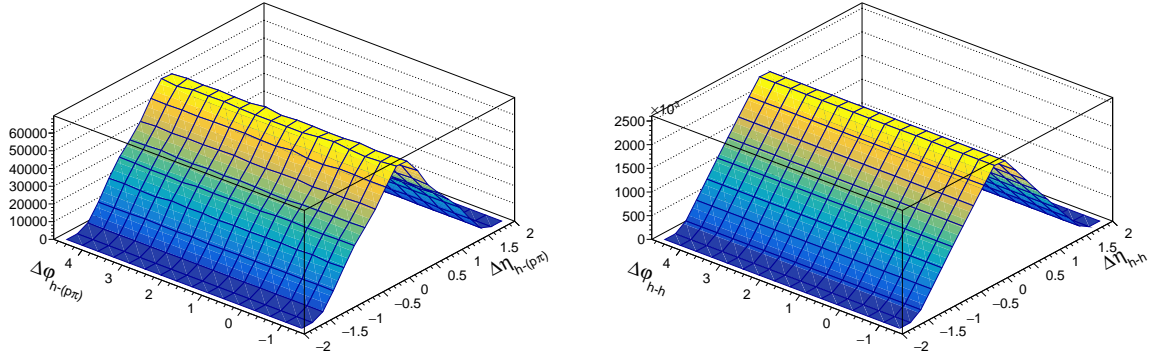


**Fig. 13:** 2-D mixed event  $h-p\pi$  (left) and  $h-h$  (right) angular correlations for the 0-20% multiplicity bin (all z-vertex bins merged together)

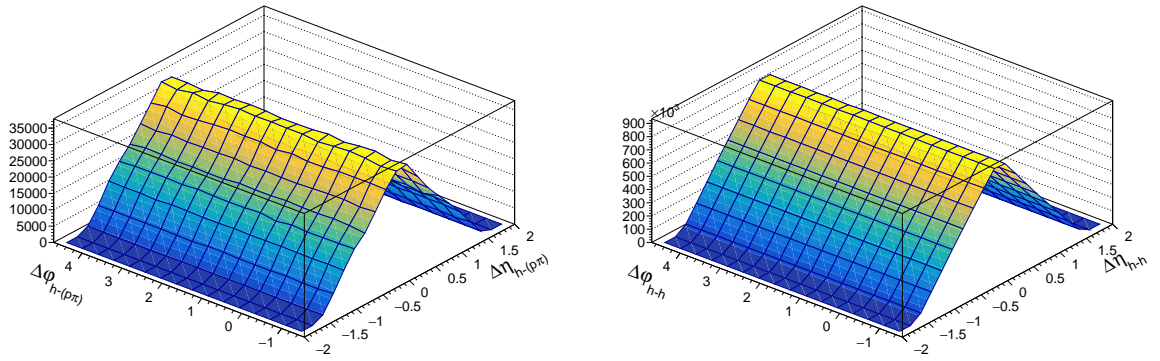


**Fig. 14:** 2-D mixed event  $h-p\pi$  (left) and  $h-h$  (right) angular correlations for the 20-50% multiplicity bin (all z-vertex bins merged together)

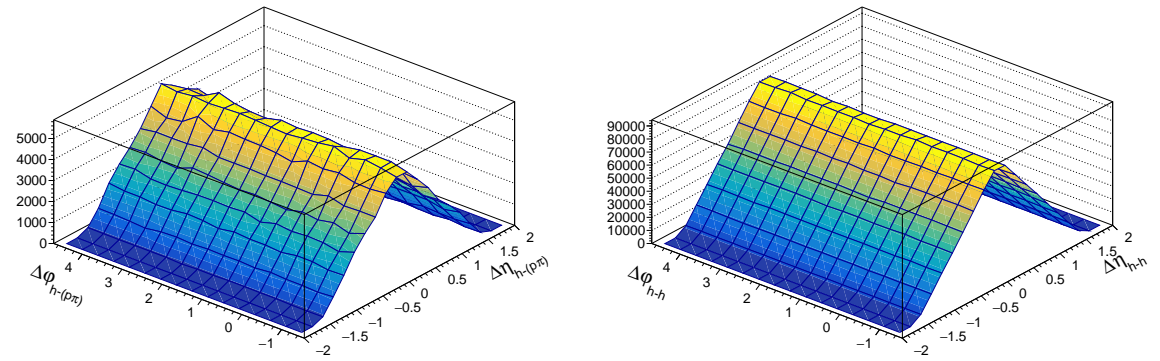


**Fig. 15:** 2-D mixed event  $h-p\pi$  (left) and  $h-h$  (right) angular correlations for the 50-80% multiplicity bin (all z-vertex bins merged together)

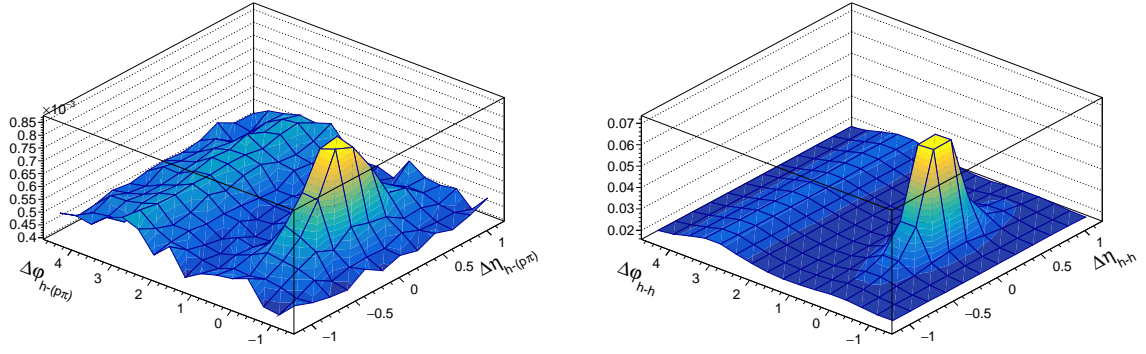


**Fig. 16:** Per-trigger 2-D  $h$ - $p\pi$  (left) and  $h$ - $h$  (right) angular correlations for the 0-20% multiplicity bin after acceptance corrections. Note that the triangular shape in  $\Delta\eta$  is no longer present.

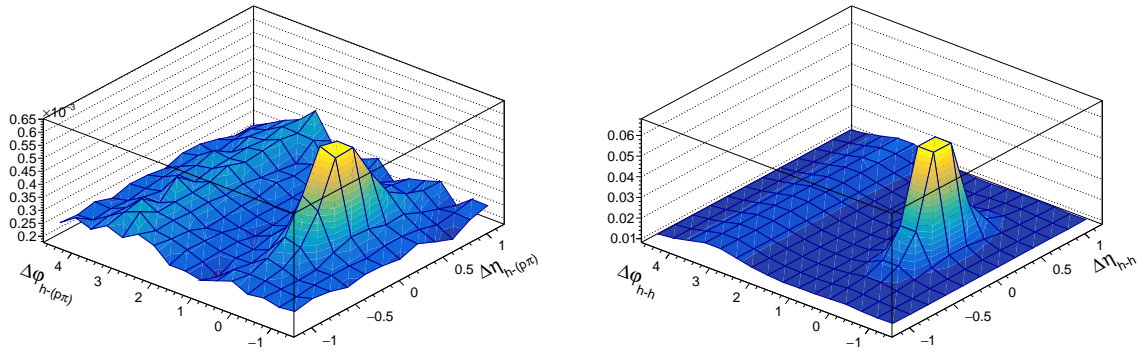


**Fig. 17:** Per-trigger 2-D  $h$ - $p\pi$  (left) and  $h$ - $h$  (right) angular correlations for the 20-50% multiplicity bin after acceptance corrections. Note that the triangular shape in  $\Delta\eta$  is no longer present.

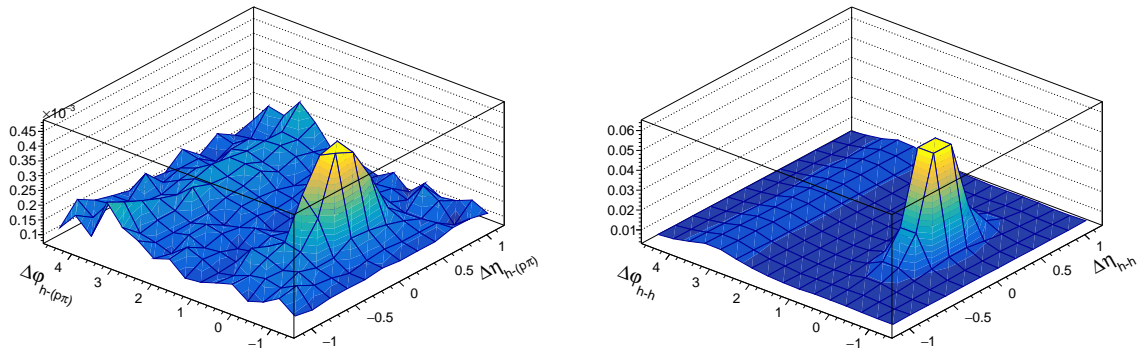


**Fig. 18:** Per-trigger 2-D  $h$ - $p\pi$  (left) and  $h$ - $h$  (right) angular correlations for the 50-80% multiplicity bin after acceptance corrections. Note that the triangular shape in  $\Delta\eta$  is no longer present.

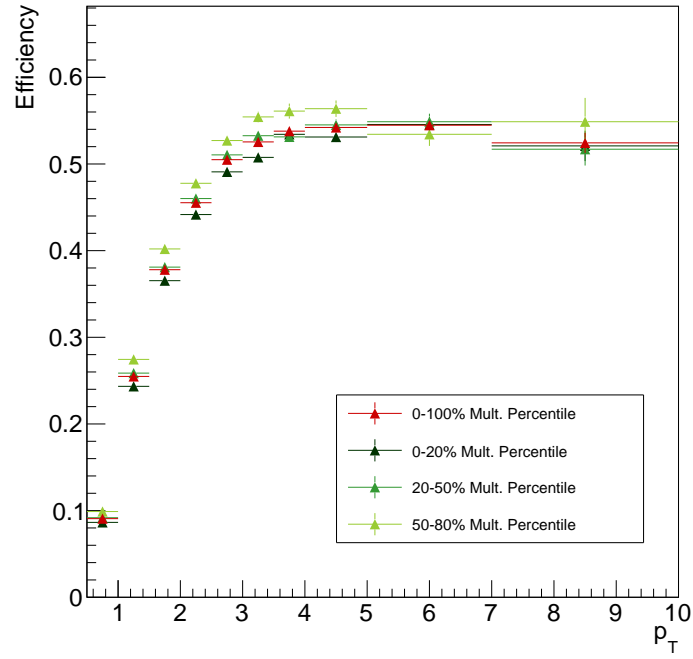


**Fig. 19:** Efficiency vs.  $p_T$  for  $\Lambda$  reconstruction for each multiplicity bin, along with an integrated 0-100% point in red. There does not appear to be any significant dependence on multiplicity.

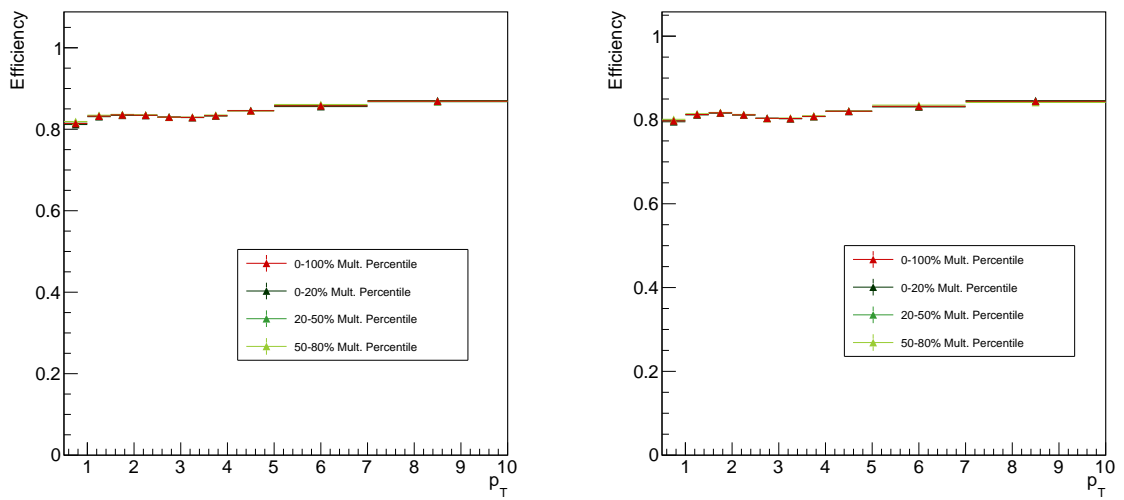


**Fig. 20:** Efficiency vs.  $p_T$  for trigger (left) and associated (right) hadrons. Both are slightly above 80% for the entire  $p_T$  range.



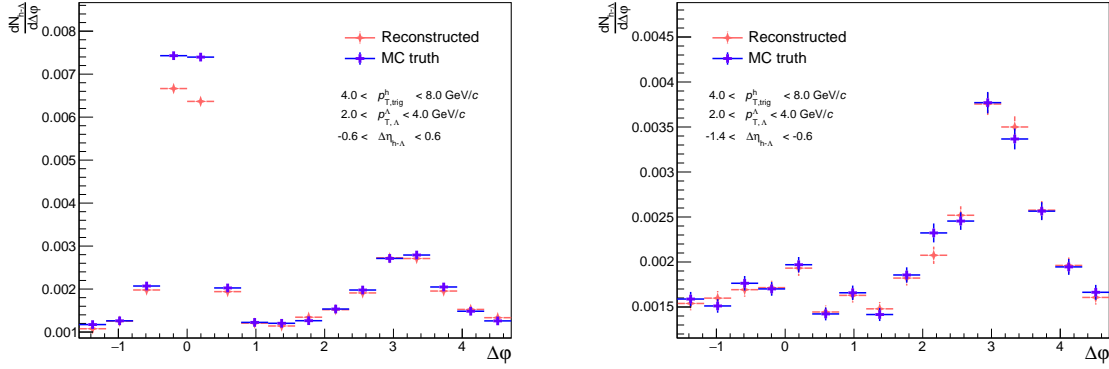


**Fig. 21:** Demonstration of the track merging effect for  $h - \Lambda$  pairs, whereby we see a dip in the reconstructed distribution at small  $\Delta\phi$  and  $\Delta\eta$  when compared to the MC ground truth (left). This dip is not present at large  $\Delta\eta$  (right), but we also lose nearly the entirety of our near-side peak.

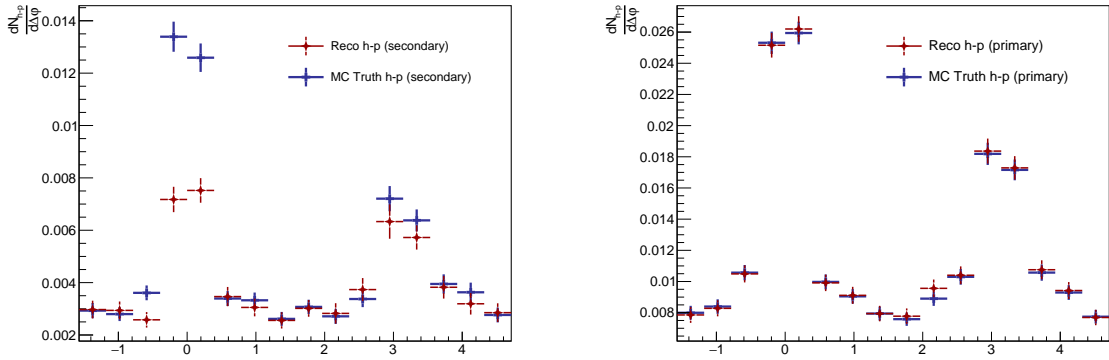


**Fig. 22:** The reconstructed and ground truth  $\Delta\phi$  distributions in the  $-1.2 < \Delta\eta < 1.2$  region for  $h$ -(secondary protons) (left) and  $h$ -(primary protons) (right). The suppression at smaller  $\Delta\phi$  is clearly seen in the secondary case, but is not observable in the primary case.

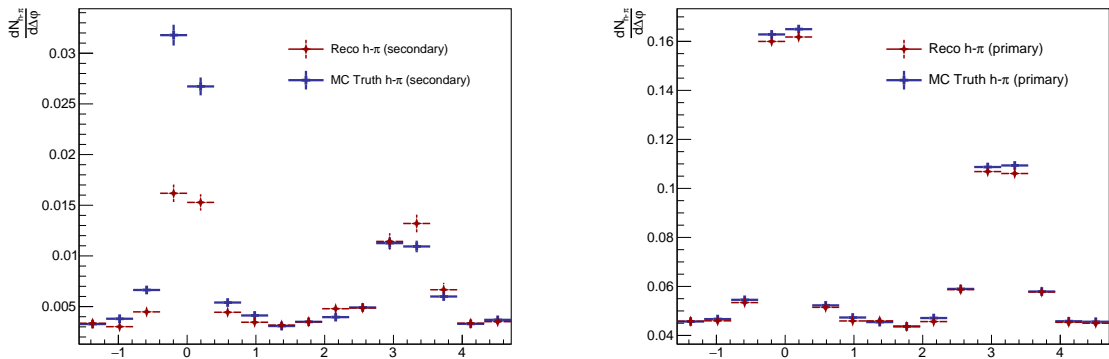


**Fig. 23:** The reconstructed and ground truth  $\Delta\phi$  distributions in the  $-1.2 < \Delta\eta < 1.2$  region for  $h$ -(secondary pions) (left) and  $h$ -(primary pions) (right). The suppression at smaller  $\Delta\eta, \Delta\phi$  is clearly seen in the secondary case, but is not observable in the primary case.



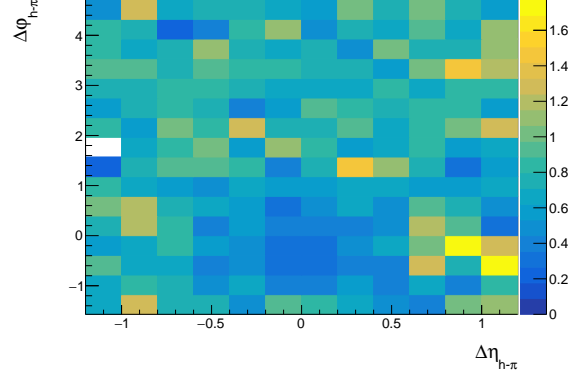


**Fig. 24:** The (reconstructed)/(ground truth)  $\Delta\eta\Delta\phi$  distribution for h-(secondary pions). There appears to be a dip from around  $-0.8 < \Delta\phi < 0.8$  and  $-0.3 < \Delta\eta < 0.3$ .

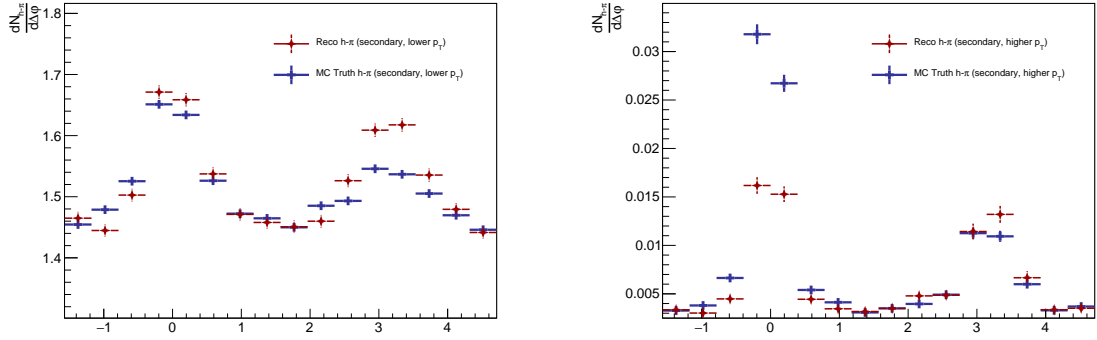


**Fig. 25:** The reconstructed and ground truth  $\Delta\phi$  distributions in the  $-1.2 < \Delta\eta < 1.2$  region for h-(secondary pions) with  $0.15 < p_{T,\pi} < 2$  (left) and  $2 < p_{T,\pi} < 4$  (right). The suppression at smaller  $\Delta\eta, \Delta\phi$  is clearly seen in the higher momentum bin, but not present in the lower one.

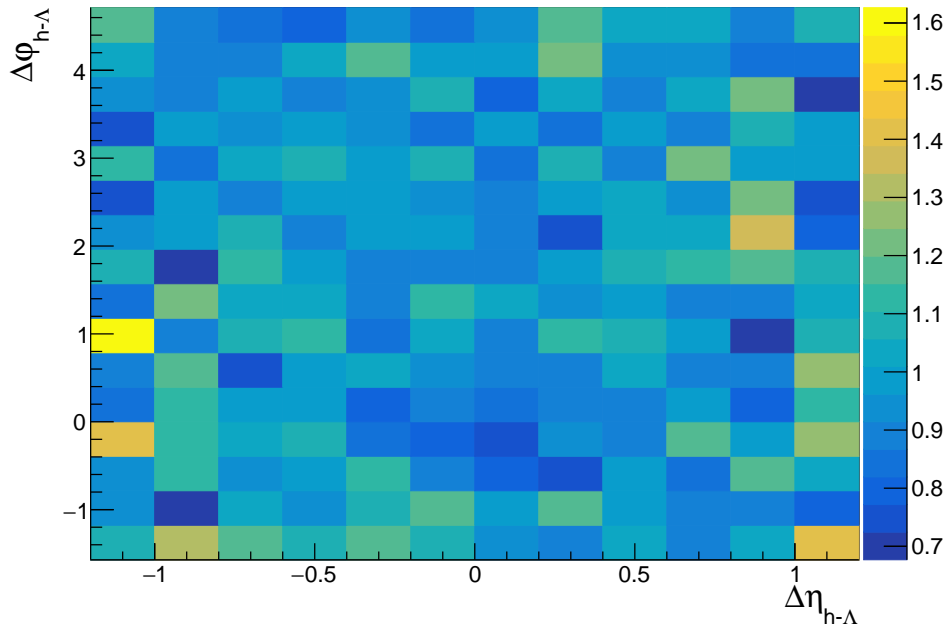


**Fig. 26:** Efficiency template for track merging correction. Due to the poor statistics of this template, the correction is not applied to our final results.

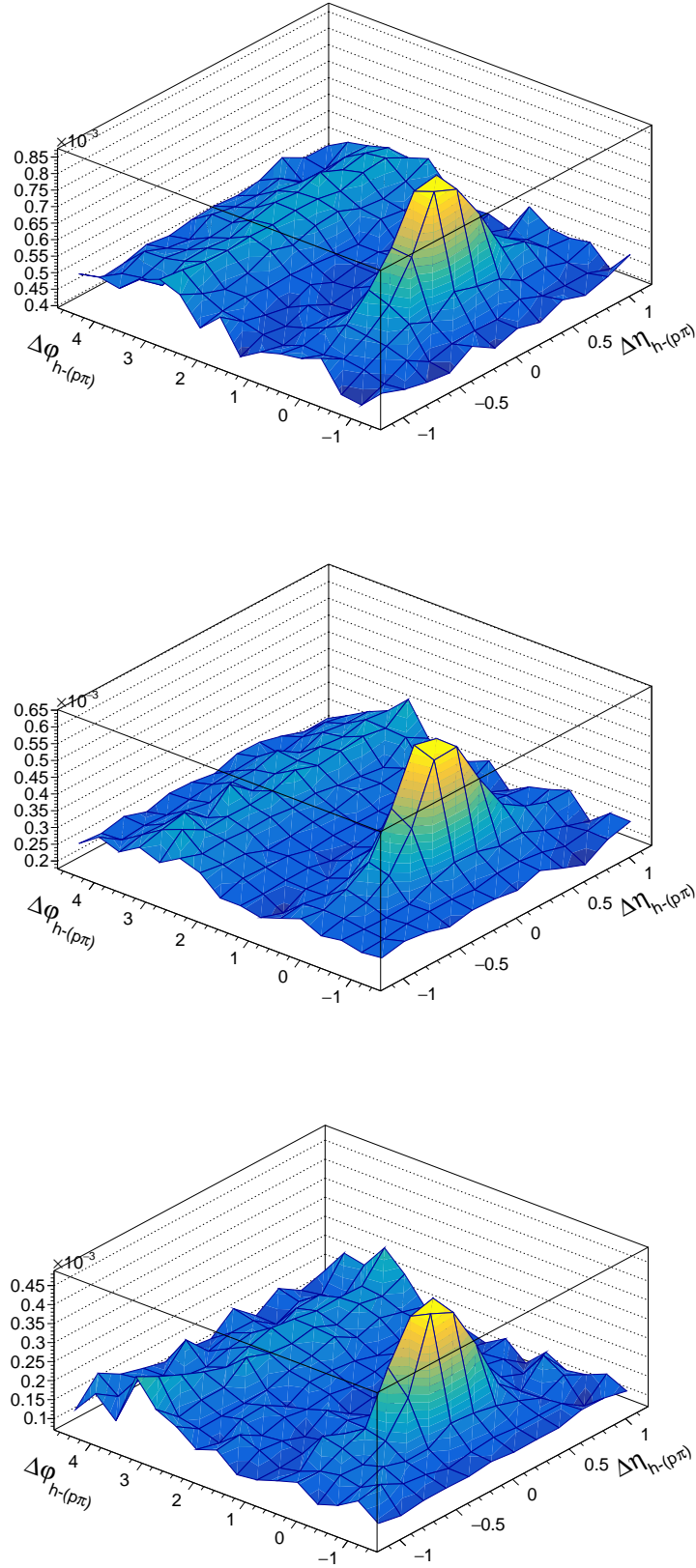


**Fig. 27:** Per-trigger normalized 2D angular correlations for h- $\Lambda$  pairs in the 0-20% (top), 20-50% (center) and 50-80% (bottom) multiplicity bins.

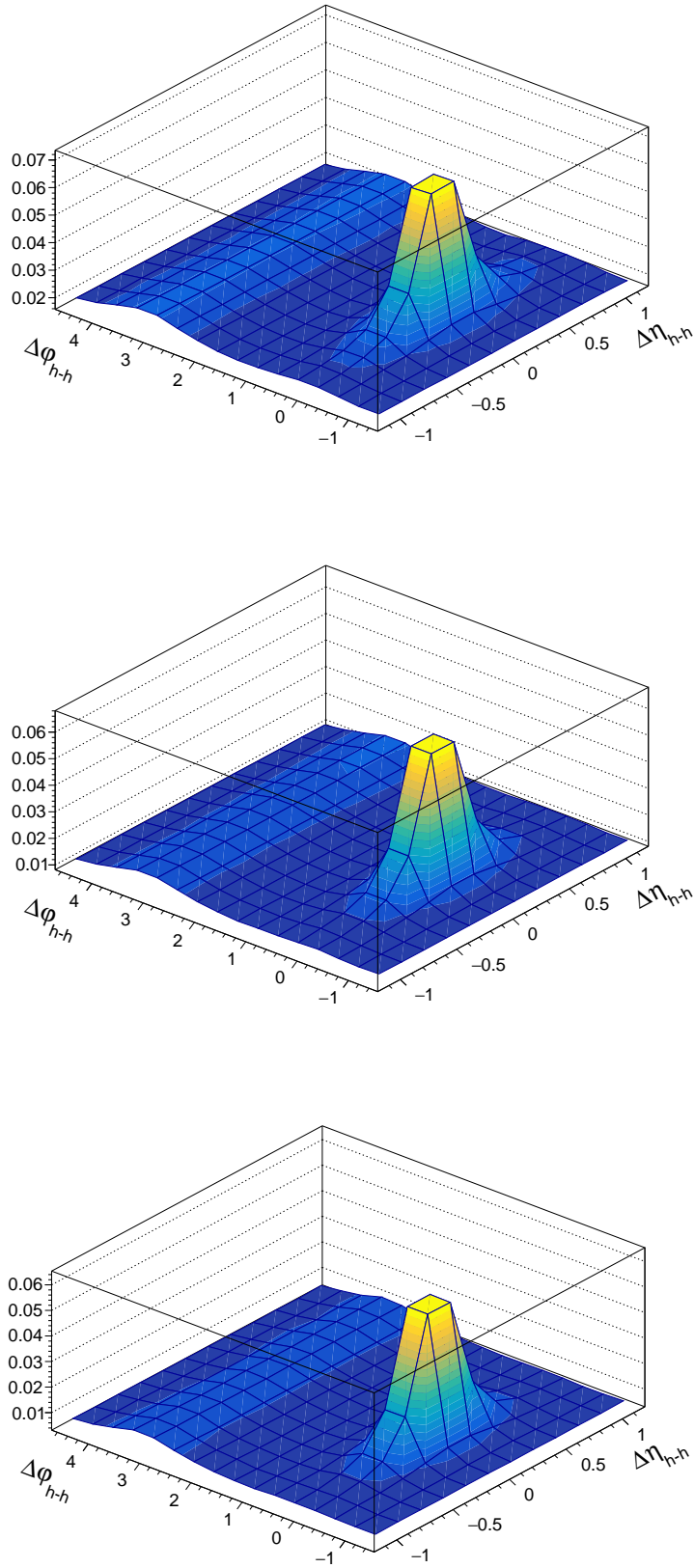


**Fig. 28:** Per-trigger normalized 2D angular correlations for h-h pairs in the 0-20% (top), 20-50% (center) and 50-80% (bottom) multiplicity bins.

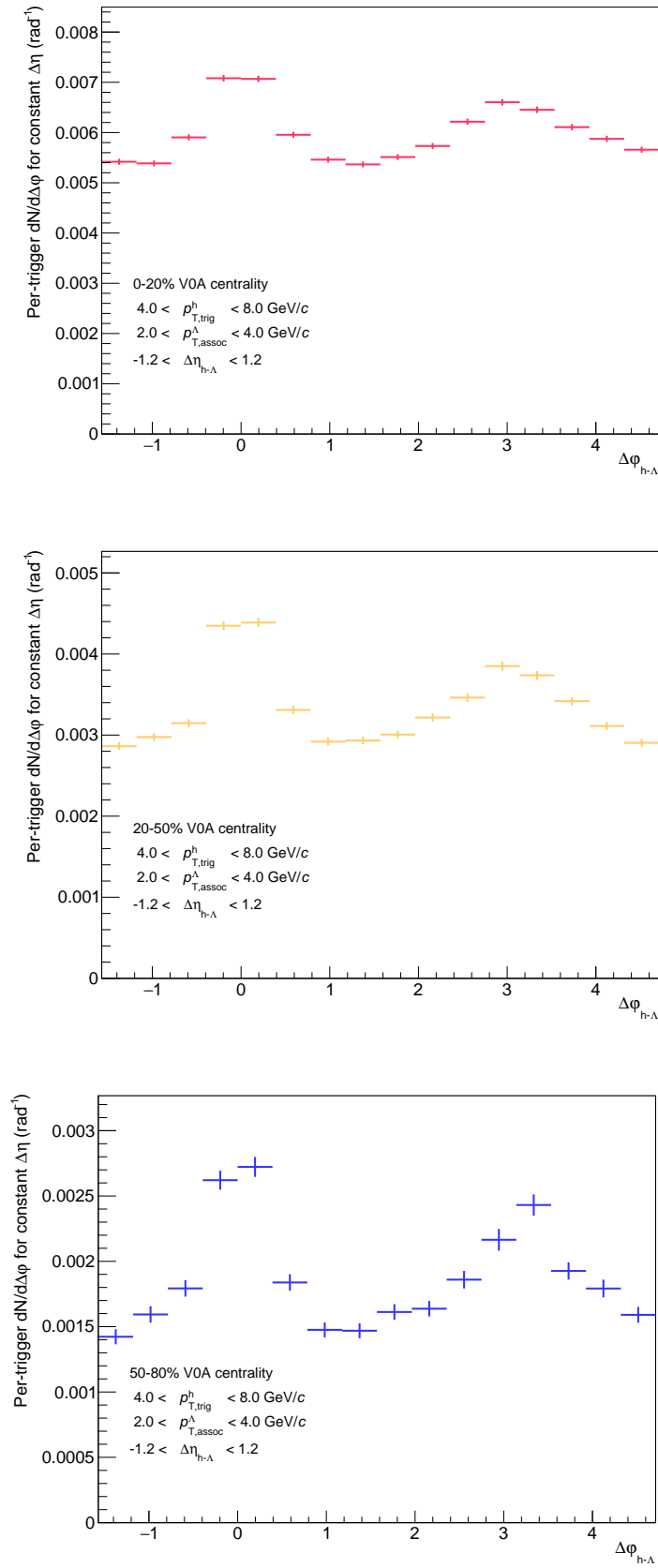


**Fig. 29:** Per-trigger normalized  $\Delta\phi$  correlations for  $h$ - $\Lambda$  pairs in the 0-20% (top), 20-50% (center) and 50-80% (bottom) multiplicity bins.

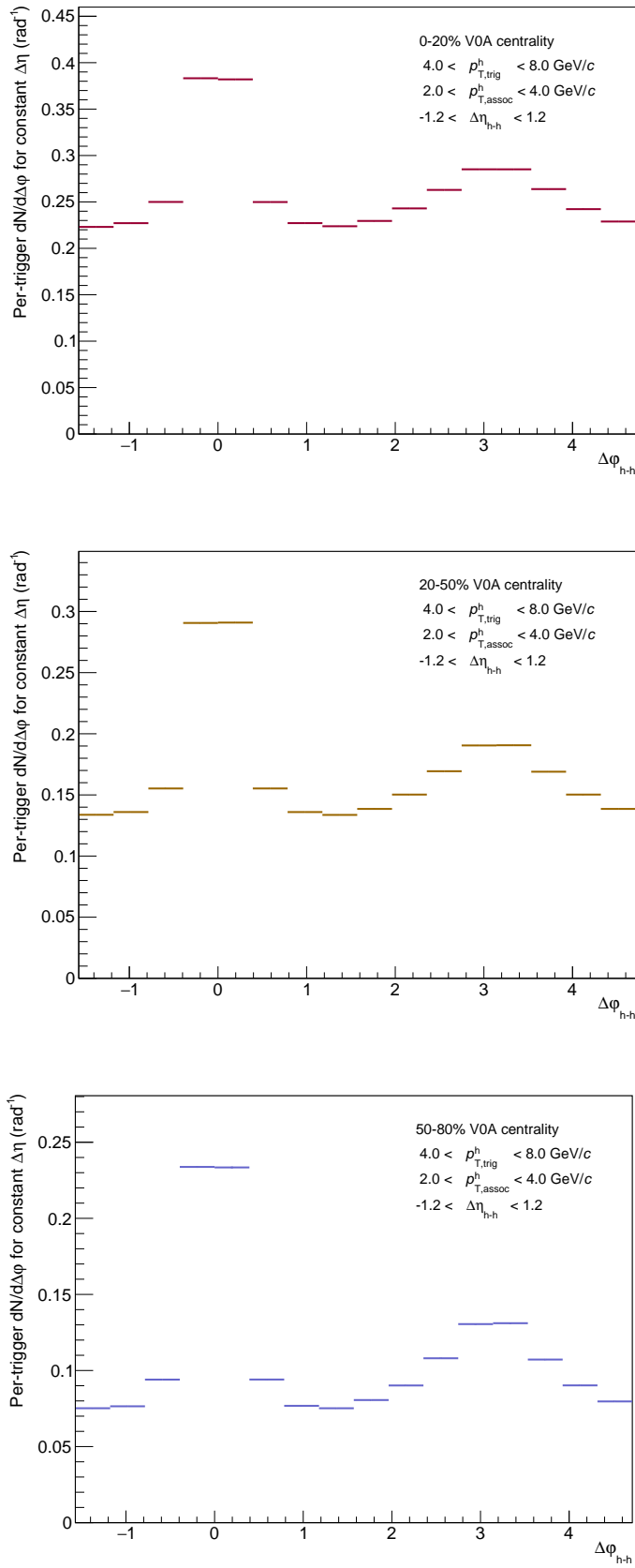


**Fig. 30:** Per-trigger normalized  $\Delta\phi$  correlations for h-h pairs in the 0-20% (top), 20-50% (center) and 50-80% (bottom) multiplicity bins.

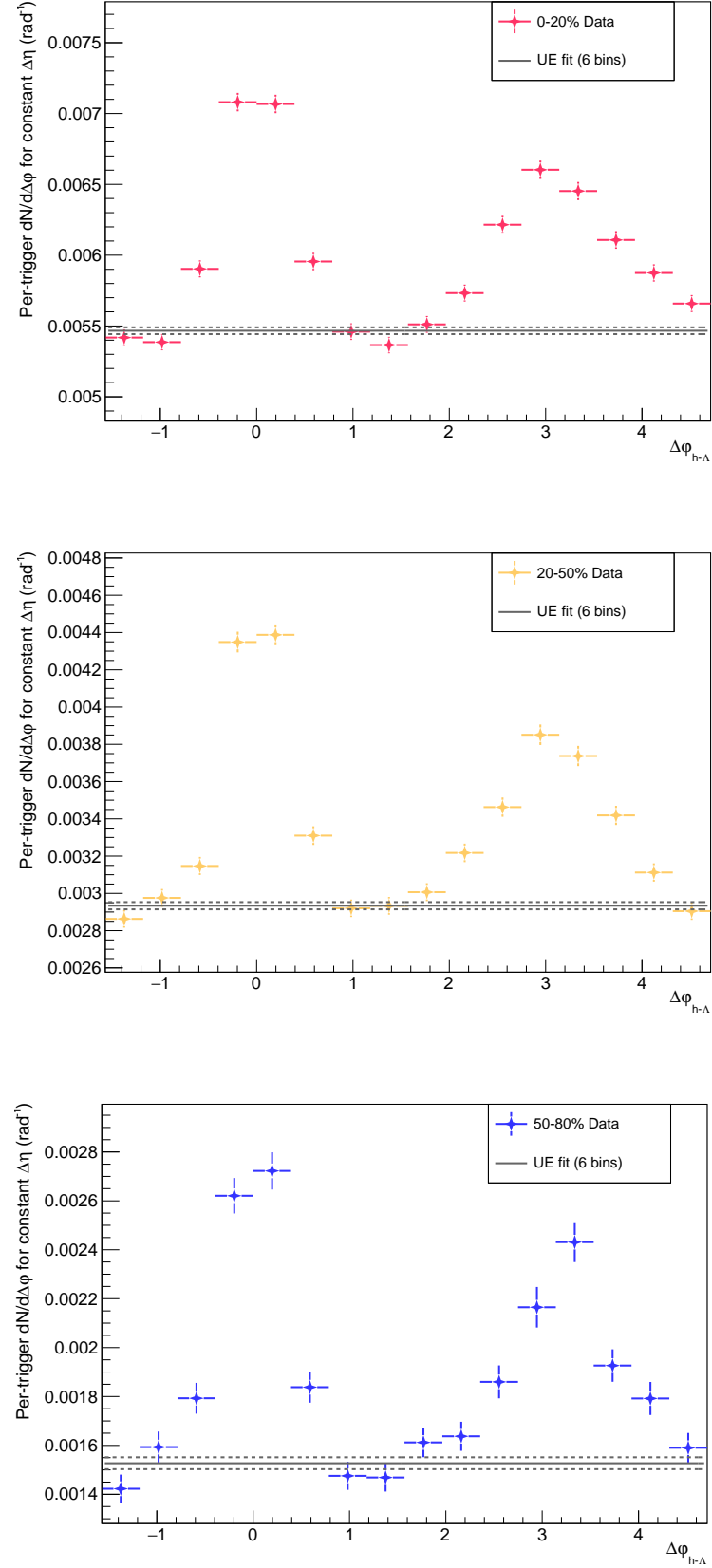


**Fig. 31:** The final per-trigger  $h - \Lambda$   $\Delta\phi$  correlations with underlying event fit for the 0-20% (top), 20-50% (center) and 50-80% (bottom) multiplicity bins. The solid line is the central value for the fit, with the dashed lines representing the error ( $\pm$ ). The underlying event fit was taken using the 6-bin technique described in this section.

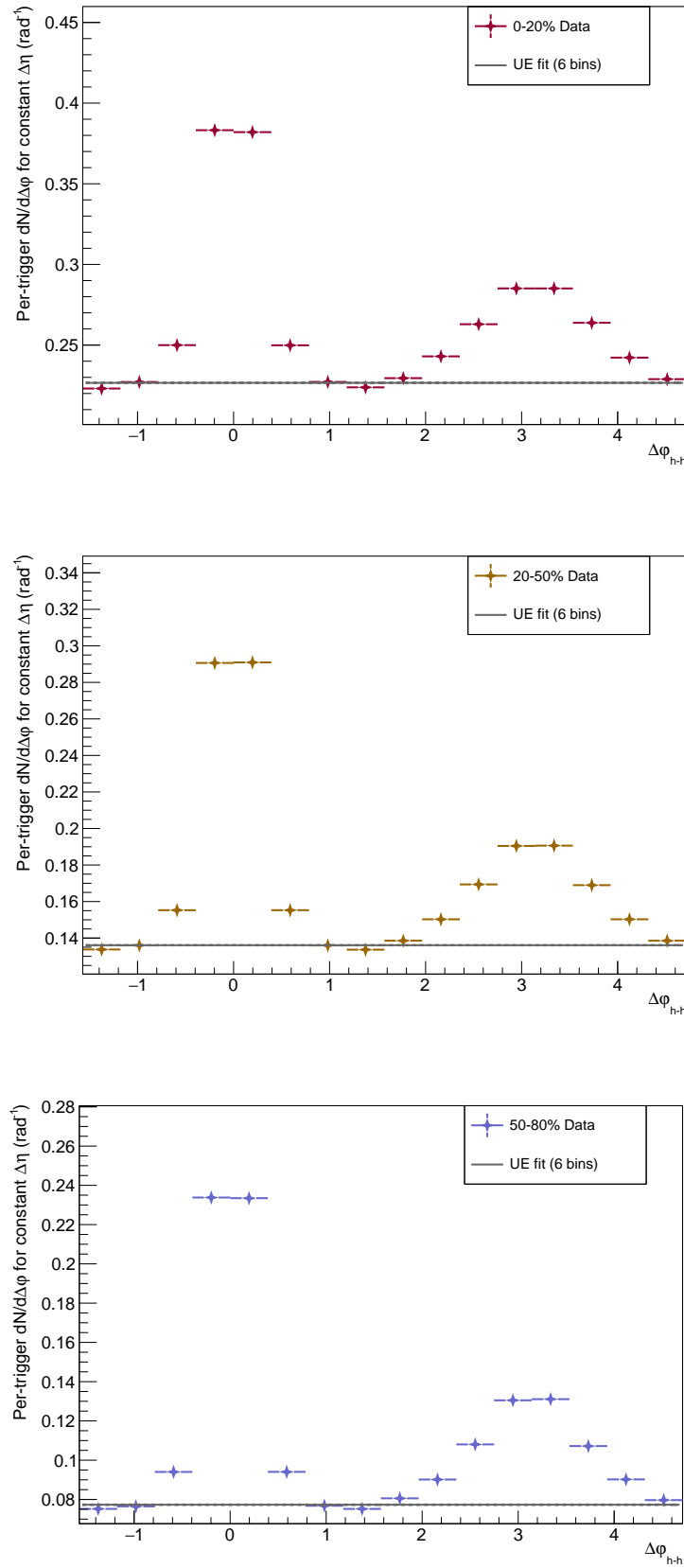


**Fig. 32:** The final per-trigger  $h-h$   $\Delta\phi$  correlations with underlying event fit for the 0-20% (top), 20-50% (center) and 50-80% (bottom) multiplicity bins. The solid line is the central value for the fit, with the dashed lines representing the error ( $\pm$ ). The underlying event fit was taken using the 6-bin technique described in this section.



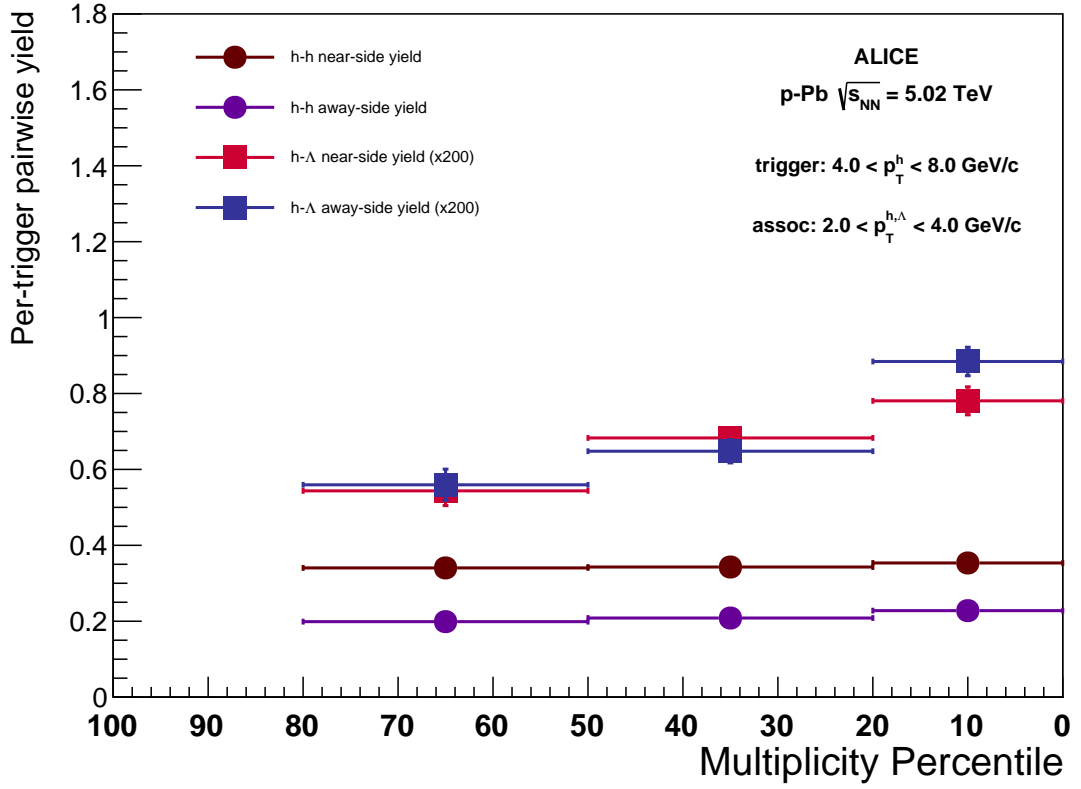


**Fig. 33:** Per-trigger pairwise  $h - \Lambda$  (scaled by 200 for clarity) and  $h - h$  yields plotted with respect to our multiplicity bins. The  $h - \Lambda$  sees roughly a 70% increase from the lowest multiplicity bin to the highest, while the  $h - h$  yield only sees around a 5% increase.

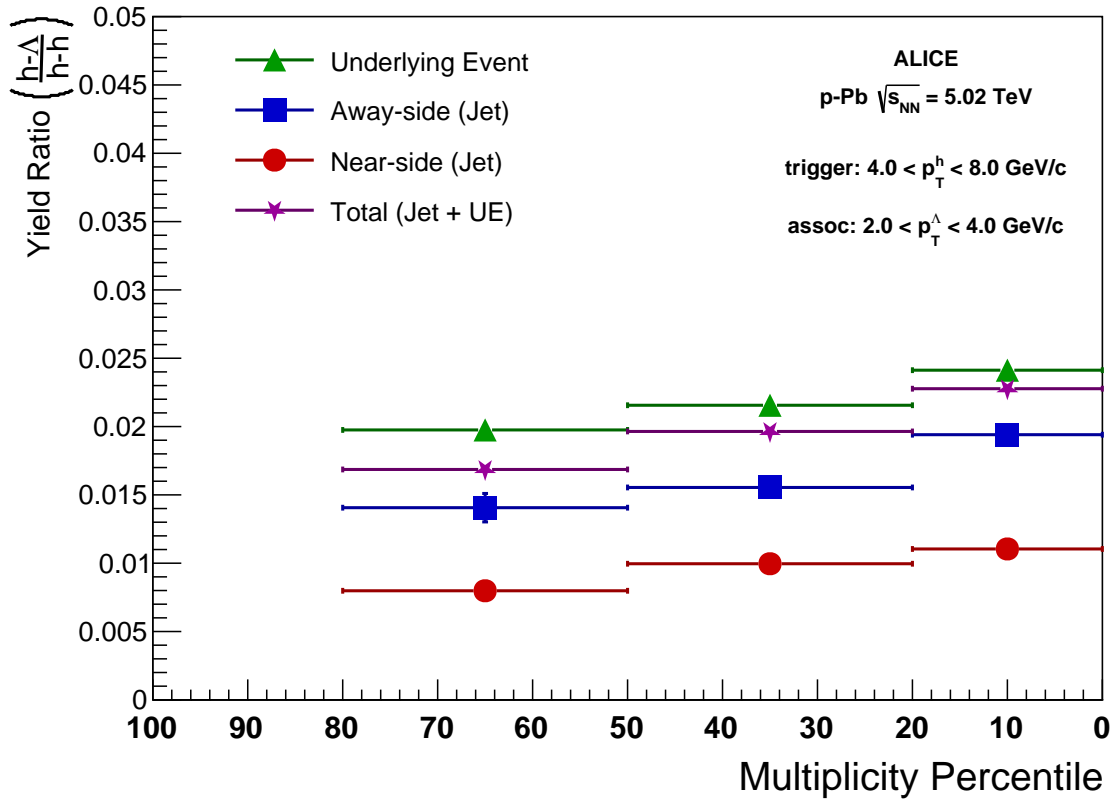
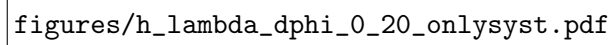
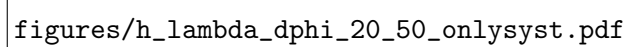


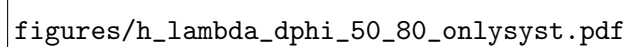
**Fig. 34:** Ratio of the per-trigger yields of  $h - \Delta/h - h$  pairs as a function of multiplicity percentile for each of the kinematic regions. The yields are extracted using the procedure described in Section ??, with values taken from Tables ?? and ??.



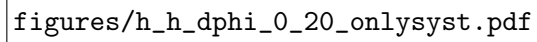
figures/h\_lambda\_dphi\_0\_20\_onlysyst.pdf



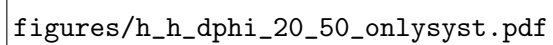
figures/h\_lambda\_dphi\_20\_50\_onlysyst.pdf



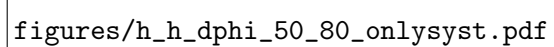
figures/h\_lambda\_dphi\_50\_80\_onlysyst.pdf



figures/h\_h\_dphi\_0\_20\_onlysyst.pdf



figures/h\_h\_dphi\_20\_50\_onlysyst.pdf



figures/h\_h\_dphi\_50\_80\_onlysyst.pdf

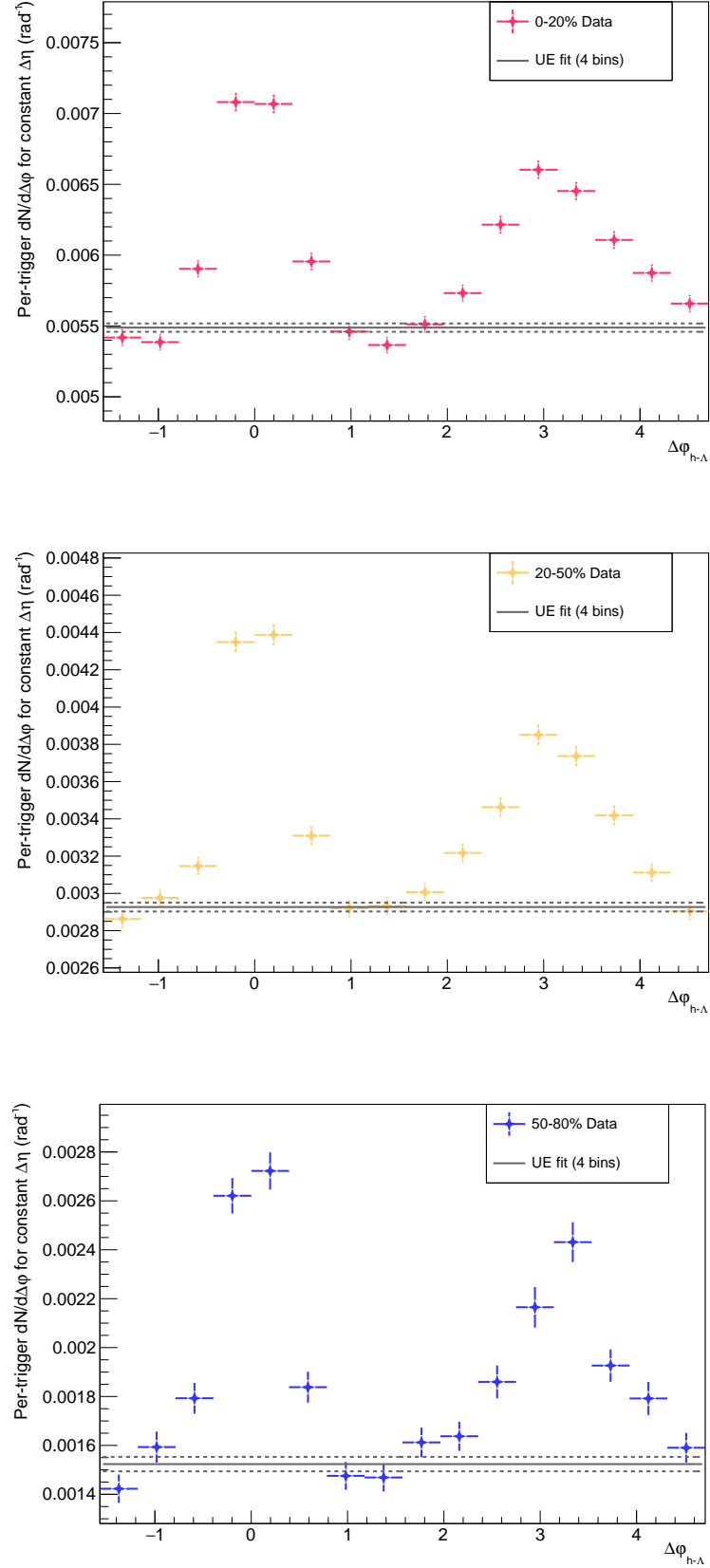


**Fig. 37:** The final per-trigger  $h - \Lambda$   $\Delta\phi$  correlations with underlying event fit for the 0-20% (top), 20-50% (center) and 50-80% (bottom) multiplicity bins. The solid line is the central value for the fit, with the dashed lines representing the error ( $\pm$ ). The underlying event fit was taken using the 4-bin technique described in this section.

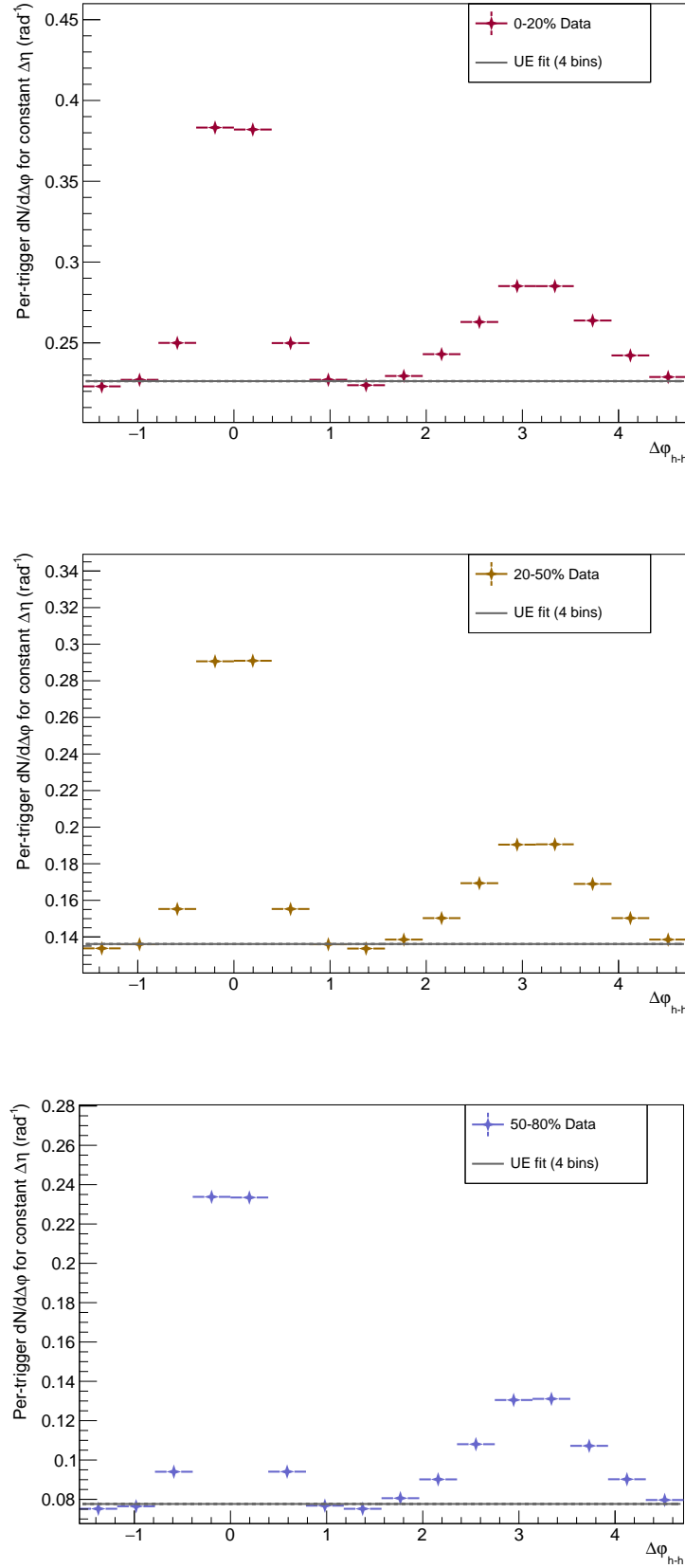


**Fig. 38:** The final per-trigger  $h-h$   $\Delta\phi$  correlations with underlying event fit for the 0-20% (top), 20-50% (center) and 50-80% (bottom) multiplicity bins. The solid line is the central value for the fit, with the dashed lines representing the error (+/-). The underlying event fit was taken using the 4-bin technique described in this section.

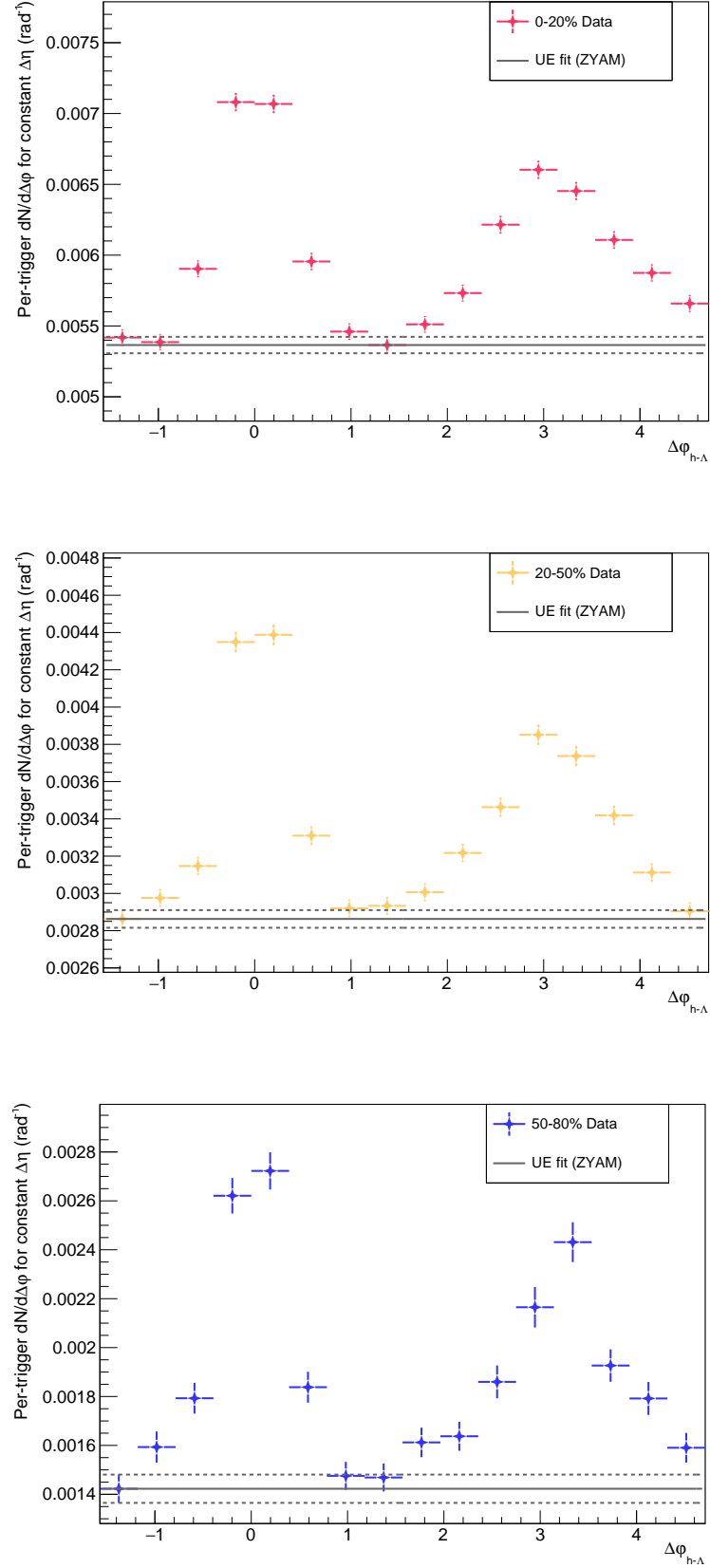


**Fig. 39:** The final per-trigger  $h - \Lambda$   $\Delta\phi$  correlations with underlying event fit for the 0-20% (top), 20-50% (center) and 50-80% (bottom) multiplicity bins. The solid line is the central value for the fit, with the dashed lines representing the error ( $\pm$ ). The underlying event fit was taken using the ZYAM technique described in this section.

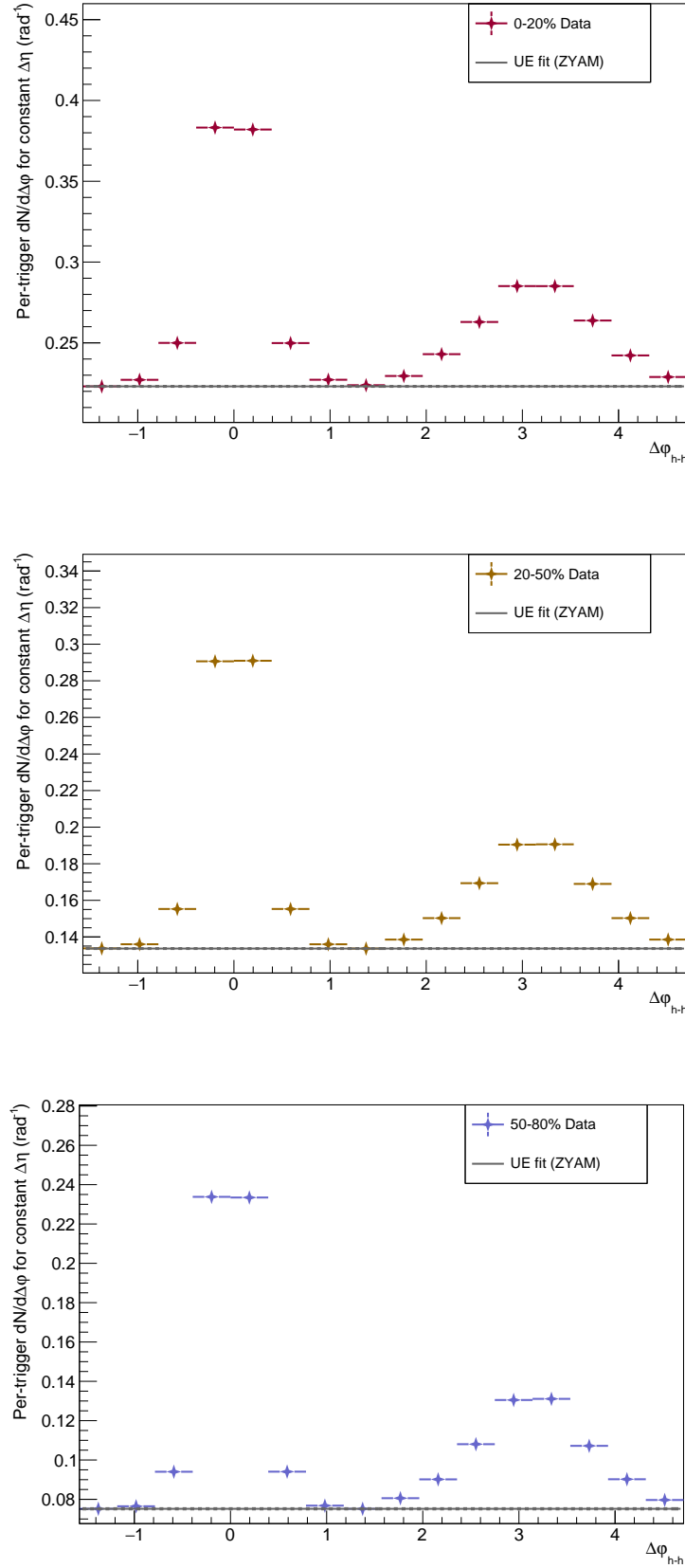


**Fig. 40:** The final per-trigger  $h-h$   $\Delta\phi$  correlations with underlying event fit for the 0-20% (top), 20-50% (center) and 50-80% (bottom) multiplicity bins. The solid line is the central value for the fit, with the dashed lines representing the error (+/-). The underlying event fit was taken using the ZYAM technique described in this section.



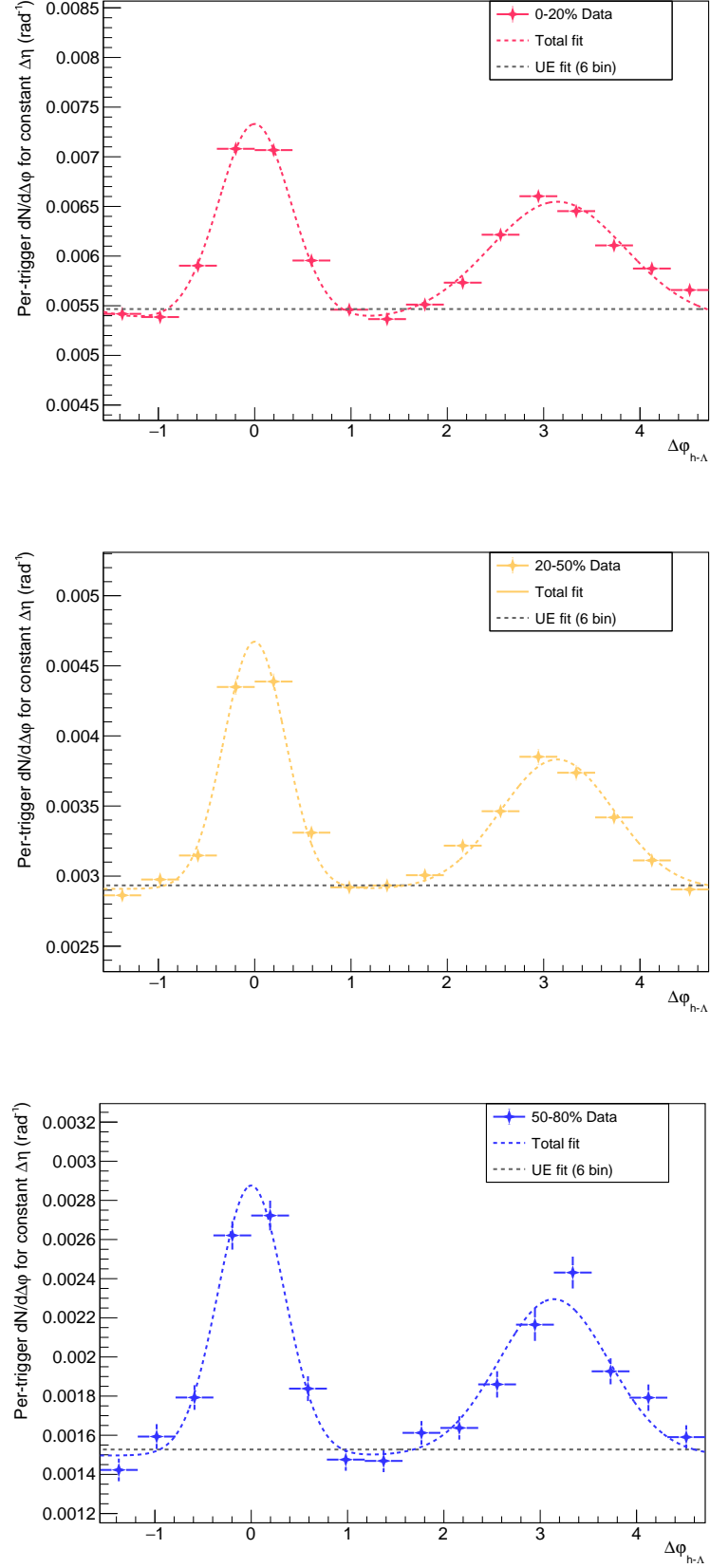


**Fig. 41:** The final per-trigger  $h - \Lambda$   $\Delta\phi$  correlations with the full correlation fit for the 0-20% (top), 20-50% (center) and 50-80% (bottom) multiplicity bins. The fit was generated using the technique described in this section.

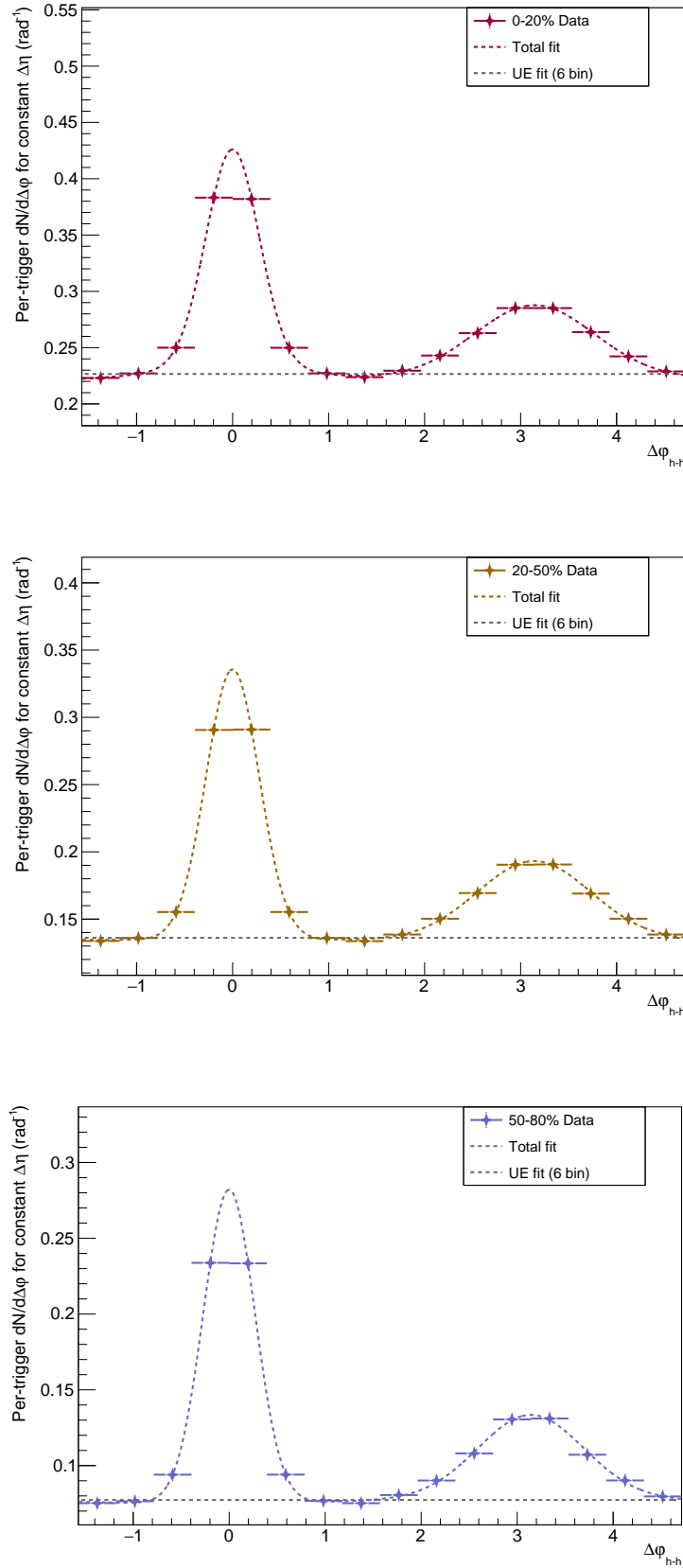


**Fig. 42:** The final per-trigger  $h-h$   $\Delta\phi$  correlations with the full correlation fit for the 0-20% (top), 20-50% (center) and 50-80% (bottom) multiplicity bins. The fit was generated using the technique described in this section.

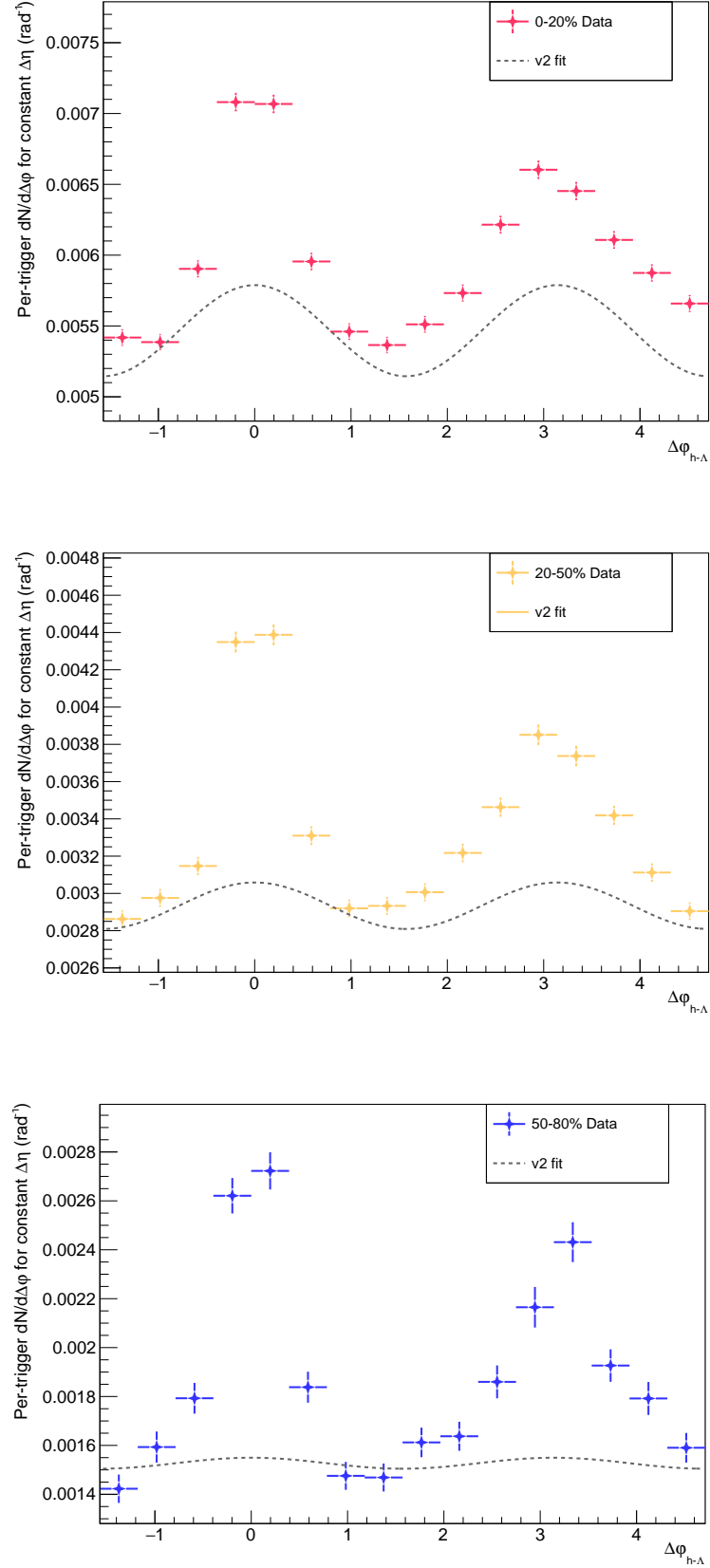


**Fig. 43:** The final per-trigger  $h-\Lambda$   $\Delta\phi$  correlations with the  $v_2$  fit for the 0-20% (top), 20-50% (center) and 50-80% (bottom) multiplicity bins. The  $v_2$  fit was generated using the technique described in this section. The most central multiplicity bin sees a substantial contribution from  $v_2$ , whereas the other bins only see a small contribution.

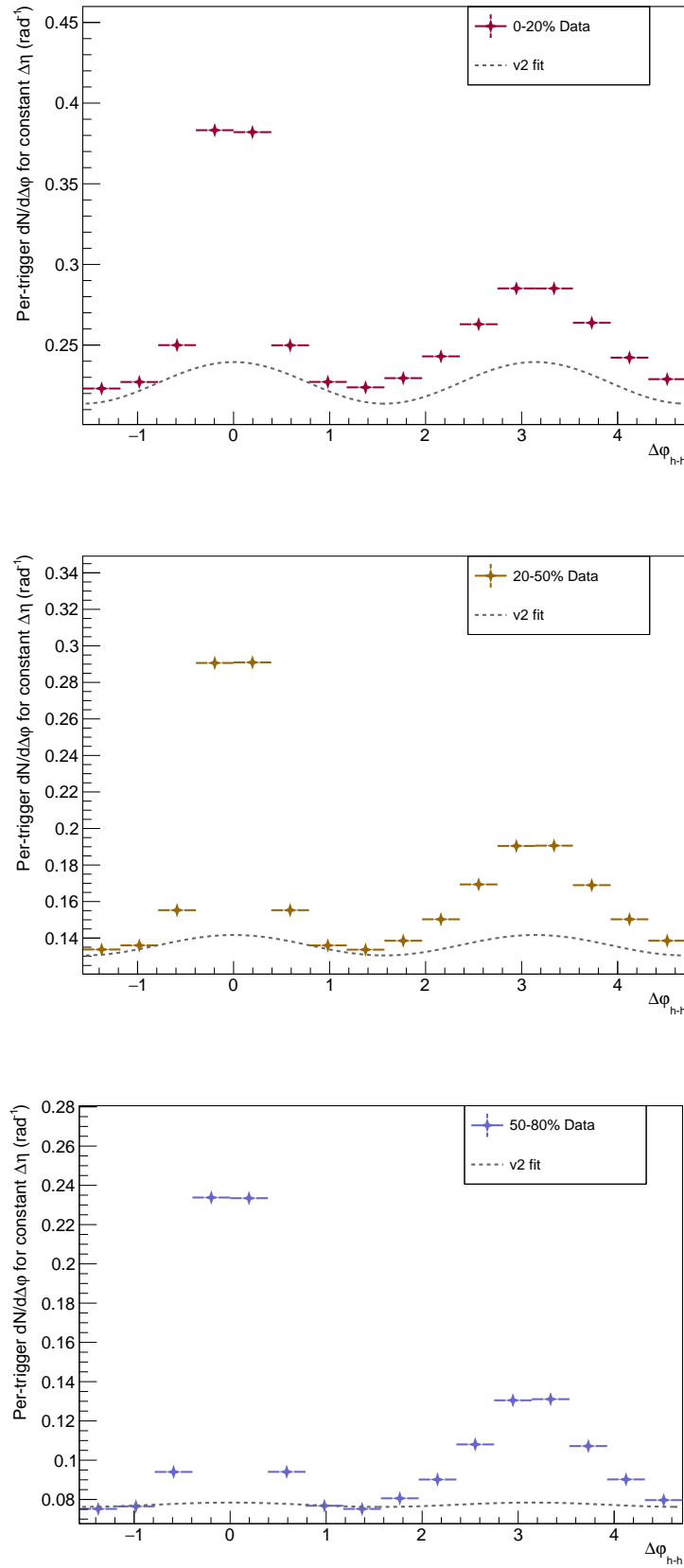


**Fig. 44:** The final per-trigger  $h-h$   $\Delta\phi$  correlations with the  $v_2$  fit for the 0-20% (top), 20-50% (center) and 50-80% (bottom) multiplicity bins. The fit was generated using the technique described in this section. All multiplicity bins see a mostly negligible contribution from  $v_2$ .

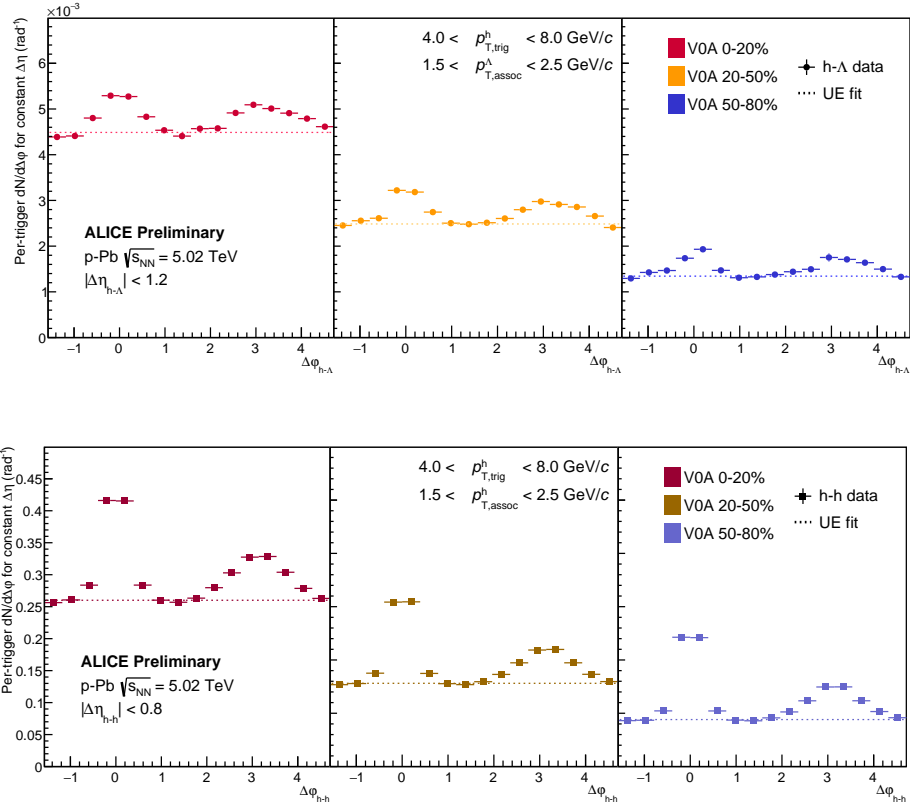


**Fig. 45:** Final  $h-\Lambda$  (top) and  $h-h$  (bottom)  $\Delta\phi$  distributions in the low  $p_T$  bin. The jet-like components appear suppressed when compared to our full momentum range measurement.

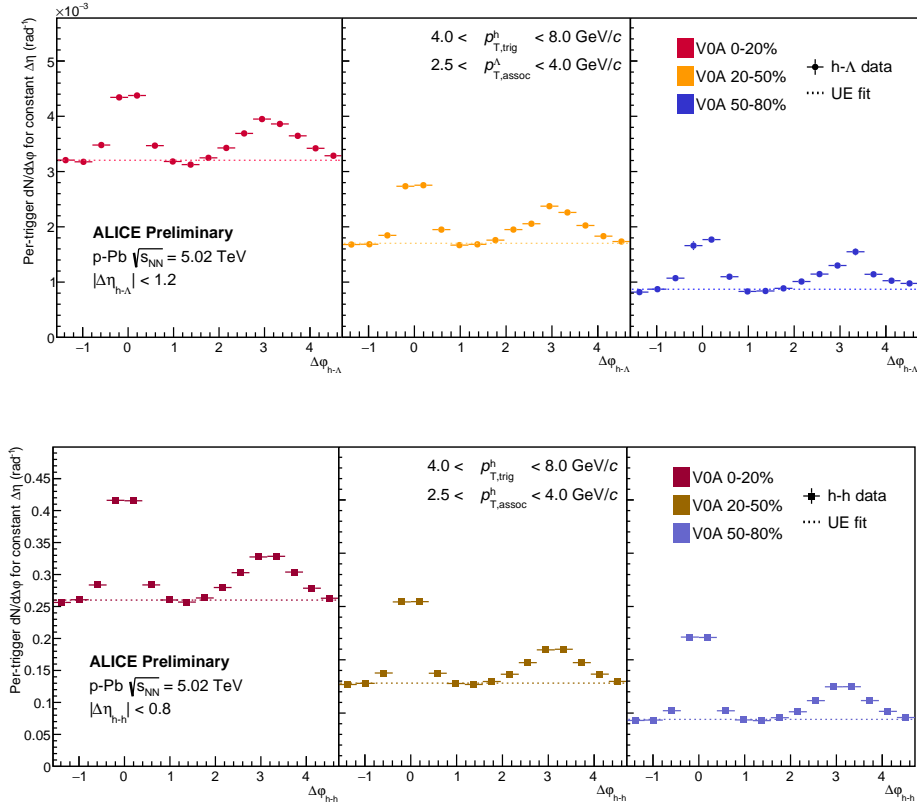


**Fig. 46:** Final  $h-\Lambda$  (top) and  $h-h$  (bottom)  $\Delta\phi$  distributions in the high  $p_T$  bin. There appears to be a slight enhancement of the jet-like components when compared to our full momentum range measurement.

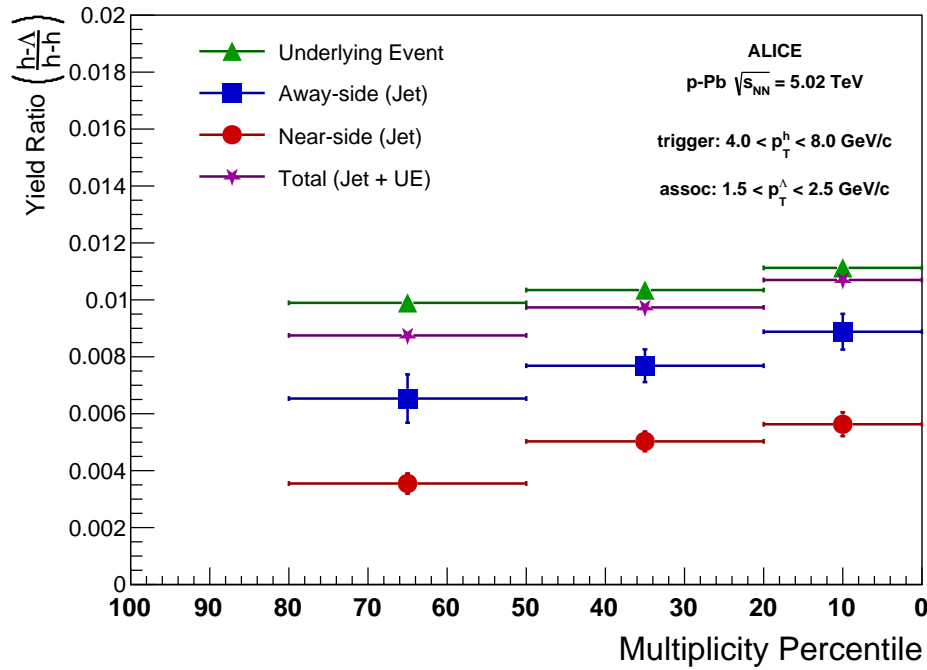


**Fig. 47:** The final  $h-\Lambda/h-h$  ratios as a function of multiplicity in the  $1.5 < p_T < 2.5$  GeV/c bin.

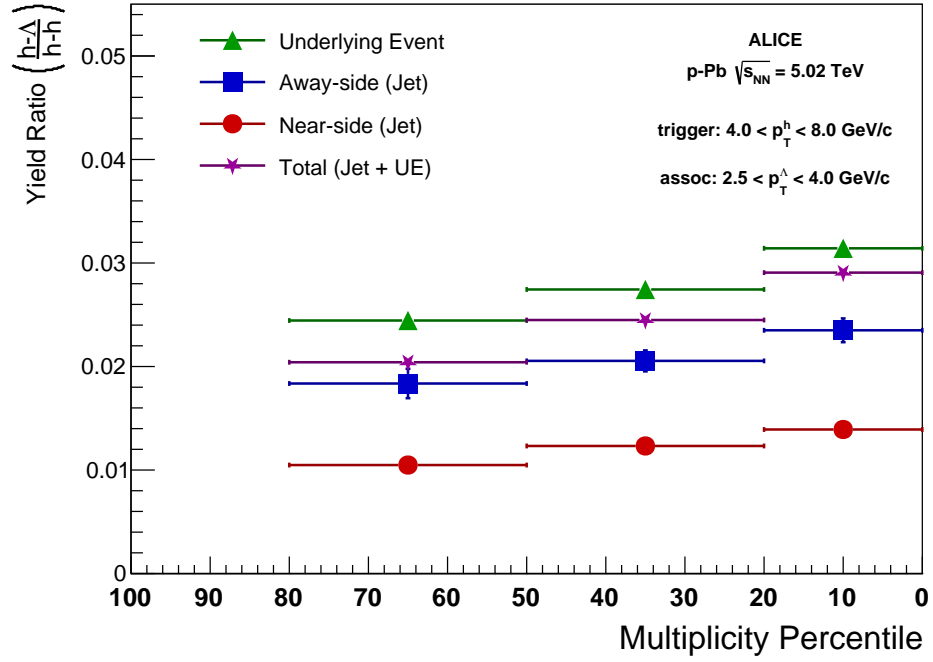


**Fig. 48:** The final  $h - \Lambda/h - h$  ratios as a function of multiplicity in the  $2.5 < p_T < 4.0$  GeV/c bin.

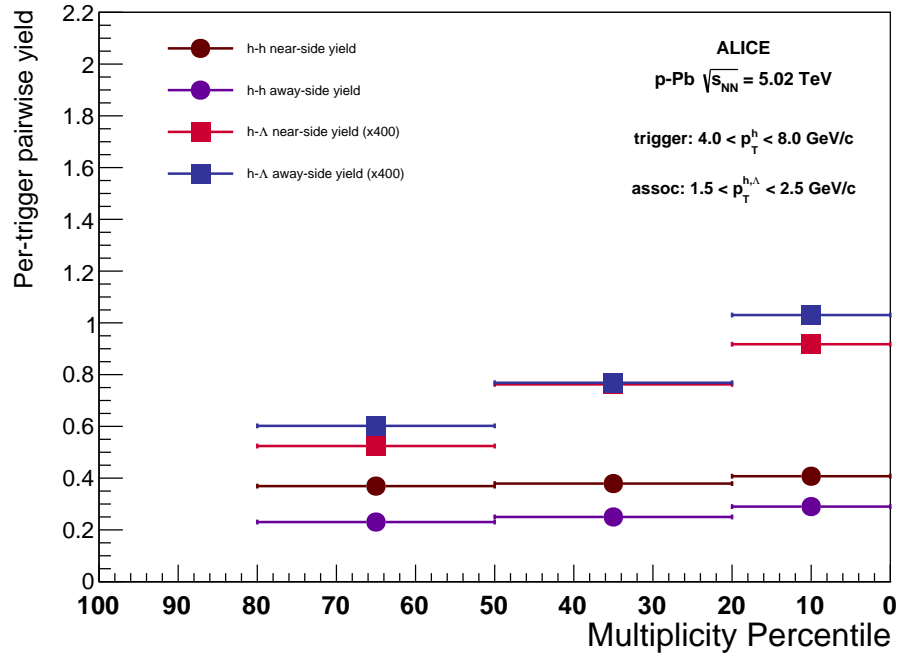


**Fig. 49:** The final per-trigger  $h - \Lambda$  and  $h - h$  yields as a function of multiplicity in the  $1.5 < p_T < 2.5$  GeV/c bin.

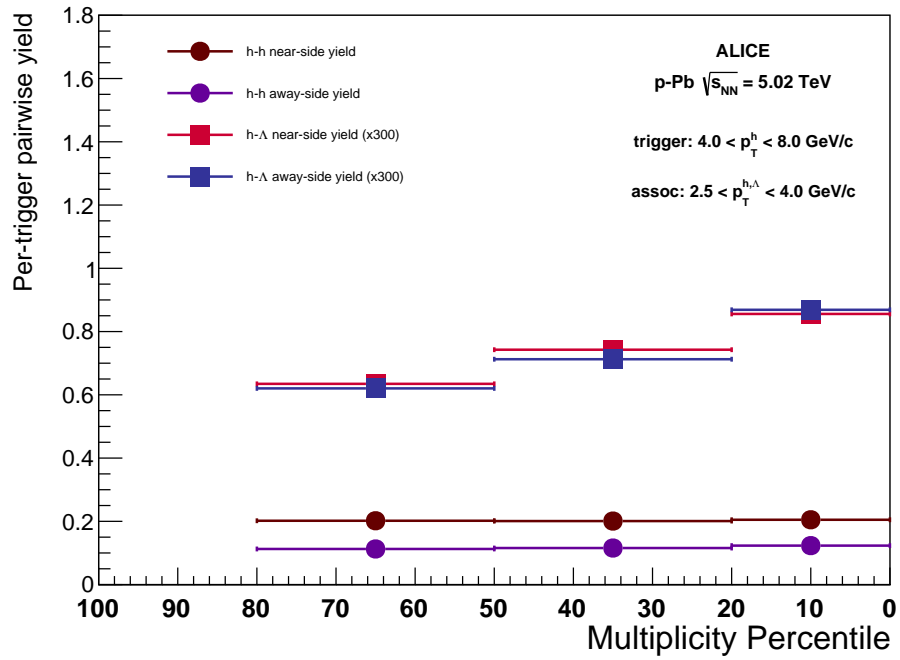


**Fig. 50:** The final per-trigger  $h - \Lambda$  and  $h - h$  yields as a function of multiplicity in the  $2.5 < p_T < 4.0$  GeV/c bin.



## 8 Cross Checks

### 8.1 Resonance Technique for $\Lambda$ Reconstruction

While using the V0 finder to reconstruct  $\Lambda$  baryons is the most common method, it is possible that the V0 finder algorithm introduces some topological biases in the  $\Lambda$  reconstruction, even when no further topological cuts are being applied to the V0 or its corresponding daughters. Because of this, we also investigate another method for reconstructing  $\Lambda$  baryons whereby all proton and pion pairs from the global AOD track list that pass the daughter cuts (Section ??) within an event are combined to reconstruct the  $\Lambda$ s. This method is referred to as the *resonance technique*, as it is the technique used to reconstruct short-lived particles that could otherwise not be reconstructed using the V0 finder.

#### 8.1.1 Combinatorial Background Estimation

As  $\Lambda$  baryons reconstructed using the resonance technique will have a large combinatorial background, the final correlation will contain  $h - (p\pi)$  pairs that need to be removed. In order to remove this background, we need both an estimate of the correlation shape of the  $h - (p\pi)$  pairs, as well as an estimate of the Signal/Background in the  $\Lambda$  mass peak region.

The background shape of the  $\Lambda$  invariant mass distribution can be estimated using one of the following techniques:

- **Like-sign  $p\pi$  pairs** - Reconstruct the invariant mass of like-sign  $p\pi$  pairs, and scale the like-sign  $p\pi$  distribution to the un-like sign  $p\pi$  distribution in a region outside of the  $\Lambda$  signal region.
- **Rotated  $p\pi$  pairs** - Reconstruct the invariant mass of unlike-sign  $p\pi$  pairs, but rotate either the pion or proton around the z-axis by  $\pi$  radians, and scale the rotated  $p\pi$  distribution to the un-like sign  $p\pi$  distribution in a region outside of the  $\Lambda$  signal region.
- **Voigt + polynomial fit** - Perform a standard fitting procedure using TMath::Voigt for the signal along with a second-order polynomial for the background.

We will address the last technique (fitting procedure) first, as it fails to properly estimate the signal and background in data. To illustrate this, we can find the best possible fits in data and extract the corresponding signal shape to compare with the signal shape in MonteCarlo (with full track reconstruction). This comparison is done for our 20-50% multiplicity bin in Figure ??.

The MonteCarlo plot was generated using our standard MC sample, and applying the same techniques for  $\Lambda$  reconstruction described previously using the global AOD list. The background on the plot was generated by taking all  $p\pi$  pairs that did NOT come from a  $\Lambda$ , verified within the MC stack. While comparing data to MonteCarlo should be done with caution, it should also be pointed out that even extracting the  $\Lambda$  signal in MonteCarlo without a priori knowledge of the background shape is nontrivial and naive attempts result in severely underestimating the signal.

While it may be possible to get a proper handle on the background shape using the fitting procedure, all attempts by the author to do so have failed. Because of this, we will only consider the first two techniques for the rest of this analysis. To determine which of the two remaining techniques is more effective, we compare the background shape of the  $\Lambda$  invariant mass distribution for both techniques in MonteCarlo where we have direct access to the background shape. The like-sign and rotated  $p\pi$  pairs are shown along with the extracted signal comparison in Figure ?. The like-sign  $p\pi$  pairs match the background shape of the  $\Lambda$  invariant mass distribution more closely than the rotated  $p\pi$  pairs, so we use the like-sign  $p\pi$  pairs to estimate the combinatorial background in the  $\Lambda$  invariant mass distribution in data.

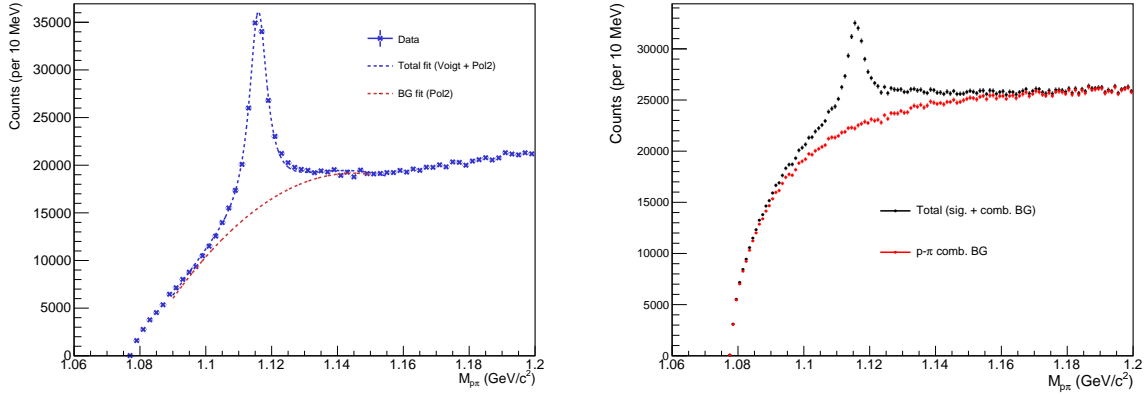


**Fig. 51:** Left: Invariant mass distribution with corresponding Voigt + Polynomial fit in our 20-50% multiplicity bin (data). Right: Our signal and background shapes in MonteCarlo (MC). Note that even though MC appears to have a completely different S/B, the signal shapes should be similar. Our fit in data appears to be massively underestimating our  $\Lambda$  signal, as our MC sample indicates we have  $\Lambda$  signal where our total data fit converges with our BG fit.

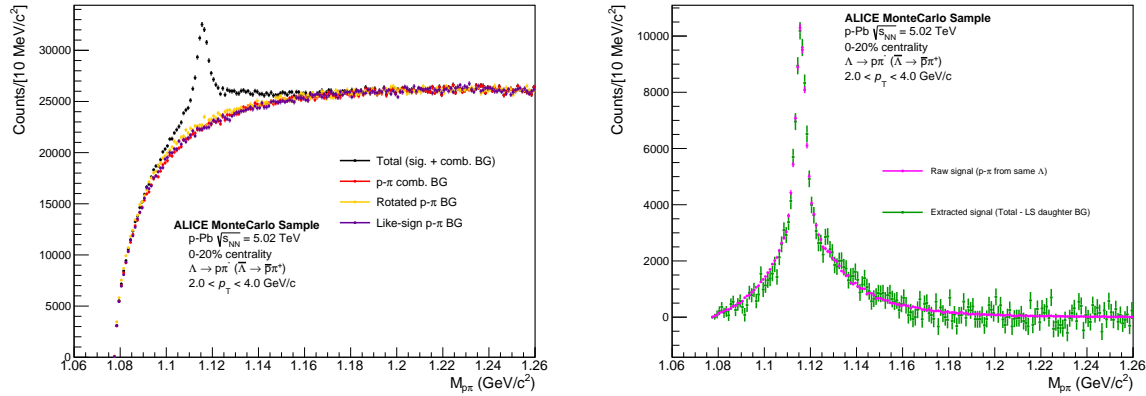


**Fig. 52:** Left: Invariant Mass distribution for unlike-sign  $p\pi$  pairs (black) in our MonteCarlo sample. The like-sign  $p\pi$  pair mass distribution (purple) and unlike-sign rotated  $p\pi$  distributions are scaled to match the unlike-sign distribution within the invariant mass region. The true combinatorial background (red) matches most closely with the like-sign pairs. Right: The actual  $\Lambda$  signal (magenta) compared with the result of subtracting the like-sign from the total unlike-sign  $p\pi$  distribution (green). The two distributions show good agreement.

The region outside of the  $\Lambda$  signal region used for scaling the background estimates is called the Right SideBand region, or RSB. The choice of RSB has a large systematical effect on the background approximation as neither the like-sign nor rotated  $p\pi$  pairs match the background shape throughout the entirety of the distribution. The RSB region was chosen to minimize the difference in shape between the extracted signal in data (total - like-sign BG) and the resonance-technique reconstructed signal shape in MonteCarlo, generated from all  $p\pi$  pairs which guaranteed came from a  $\Lambda$ . The raw unlike-sign  $p\pi$  distribution for the 0-20% Multiplicity Percentile is shown in Figure ??, and the extracted signal and comparison with MonteCarlo is shown in Figure ??.

The resonance technique  $p\pi$  invariant mass distributions for each multiplicity bin are shown in Figure ??, and a table containing their yields, signal/BG and significance is shown in Table ??.

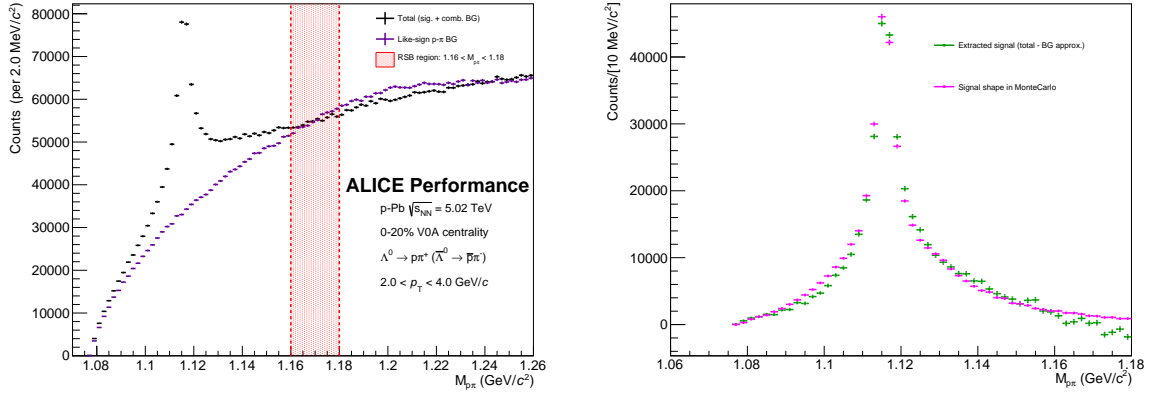


**Fig. 53:** Left: Invariant Mass distribution for unlike-sign  $p\pi$  pairs (black) along with the like-sign  $p\pi$  background (purple) and the RSB region (red) in the 0-20% multiplicity bin. Right: The extracted signal (green) compared with the resonance-technique reconstructed signal shape in MonteCarlo (magenta). The RSB was chosen such that these shapes are similar.

### 8.1.2 Invariant Mass Regions

The signal shape and background from  $\Lambda$ s reconstructed using the resonance technique is vastly different than those reconstructed using the V0 finder, thus it is necessary to define new invariant mass regions such that the signal can be properly extracted:

- unlike-sign  $p\pi$  in  $\Lambda$  mass region:  $1.014 \text{ GeV}/c^2 < M_{p\pi} < 1.026 \text{ GeV}/c^2$
- like-sign  $p\pi$  in  $\Lambda$  mass region:  $1.014 \text{ GeV}/c^2 < M_{p\pi} < 1.026 \text{ GeV}/c^2$
- unlike-sign  $p\pi$  in 0-20% multiplicity bin RSB:  $0.995 \text{ GeV}/c^2 < M_{p\pi} < 1.005 \text{ GeV}/c^2$
- unlike-sign  $p\pi$  in 20-50% multiplicity bin RSB:  $0.995 \text{ GeV}/c^2 < M_{p\pi} < 1.005 \text{ GeV}/c^2$
- unlike-sign  $p\pi$  in 50-80% multiplicity bin RSB:  $0.995 \text{ GeV}/c^2 < M_{p\pi} < 1.005 \text{ GeV}/c^2$

The signal regions were chosen to maximize significance and were not multiplicity dependent, whereas the RSB regions were chosen to minimize the difference in shape between the extracted signal in data (total - like-sign BG) and the resonance-technique reconstructed signal shape in MonteCarlo, generated from all  $p\pi$  pairs which guaranteed came from a  $\Lambda$ , as was demonstrated in Figure ???. This process was repeated for each multiplicity bin resulting in slight fluctuations of the RSB with respect to multiplicity.

For the resonance technique, the combinatorial background contribution to the correlation was removed using the like-sign  $p\pi$  distribution scaled to the RSB for each multiplicity bin, a procedure described with more detail in Section ???.

### 8.1.3 Efficiency Correction

To estimate the  $\Lambda$  reconstruction efficiency, we compare  $\Lambda$  yields reconstructed using the resonance technique to the true  $\Lambda$  yields using the MC production LHC17f2b\_FAST (anchored to LHC16q\_FAST production). The efficiency was calculated using the following formula:

$$\epsilon_{\Lambda} = \frac{N_{\Lambda, \text{ reco. with resonance technique}}}{N_{\Lambda, \text{ real MC yield}}},$$

where each  $\Lambda$  in  $N_{\Lambda, \text{ reco. with resonance technique}}$  is found in the following way:

- 629 – Find all protons and pions within the AOD list that pass our daughter cuts (Section ??, PID is done  
630 via MC label)
- 631 – For each proton in list, determine if it came from a  $\Lambda$  (via MC label)
- 632 – If proton came from  $\Lambda$ , loop through pions until we find one that came from same  $\Lambda$  (via MC label)
- 633 – Reconstruct the  $\Lambda_{reco}$  using the daughter AOD tracks
- 634 – Only keep  $\Lambda_{reco}$  if  $|\eta| < 0.8$

635 and each  $\Lambda$  in  $N_{\Lambda, \text{real MC yield}}$  meets the following criteria:

- 636 – Found in the MC stack
- 637 –  $|\eta_{\Lambda}| \leq 0.8$
- 638 – The  $\Lambda$  decays to  $p\pi$

639 As the resulting invariant mass signal from  $N_{\Lambda, \text{reco. with resonance technique}}$  is much wider than the signal  
640 from the V0 finder technique (Figure ??), the efficiency calculation is taken using the entire invariant  
641 mass range and the correction for our finite signal region is applied later (see Section ??).

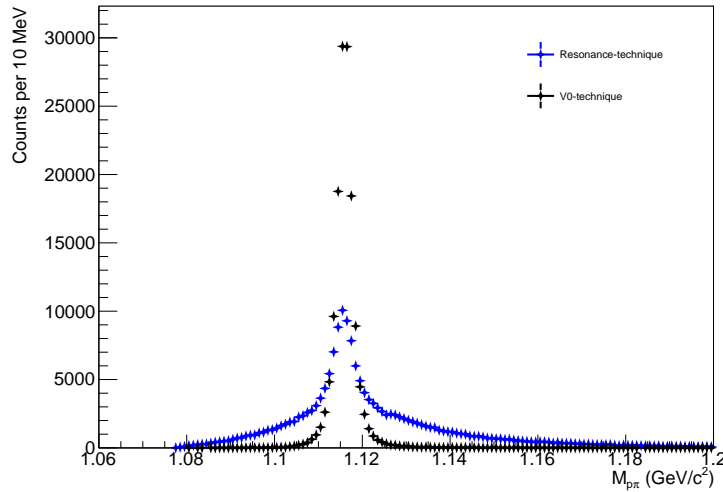


**Fig. 54:** The invariant mass signal for  $\Lambda_s$  reconstructed using the resonance technique (blue) compared to the V0 technique (black) in MC. The wider tails of the resonance technique distribution are due to using the global AOD tracks for reconstruction, which do not account for the secondary vertex position and therefore slightly miscalculate the kinematics.

642 While previous analyses focus solely on primary  $\Lambda_s$  (excluding  $\Omega$  and  $\Xi$  contamination), there is no  
643 requirement for either the V0-reconstructed  $\Lambda$  or the MC-generated  $\Lambda$  to be a primary particle. As this  
644 analysis is mostly interested in the  $\Lambda$  due to its strange quark content, whether or not the  $\Lambda$  came from  
645 a cascade decay is irrelevant. This is important to note when making comparisons between this analysis  
646 and previous analyses, as secondary contamination from cascades accounts for nearly 20% of all  $\Lambda_s$ .

647 As mentioned in Section ??, both the  $\Lambda$  and the  $\bar{\Lambda}$  were combined together for this efficiency calculation.  
648 Efficiencies were calculated as a function of  $p_T$ ,  $\eta$ ,  $\phi$ , Event Z vertex, and Multiplicity. However, the  
649 final efficiency correction was applied as a function of  $p_T$  only and can be seen in Figure ??.

650 The  $h - \Lambda$  pairwise efficiency correction is applied in the same way as described in Section ??.

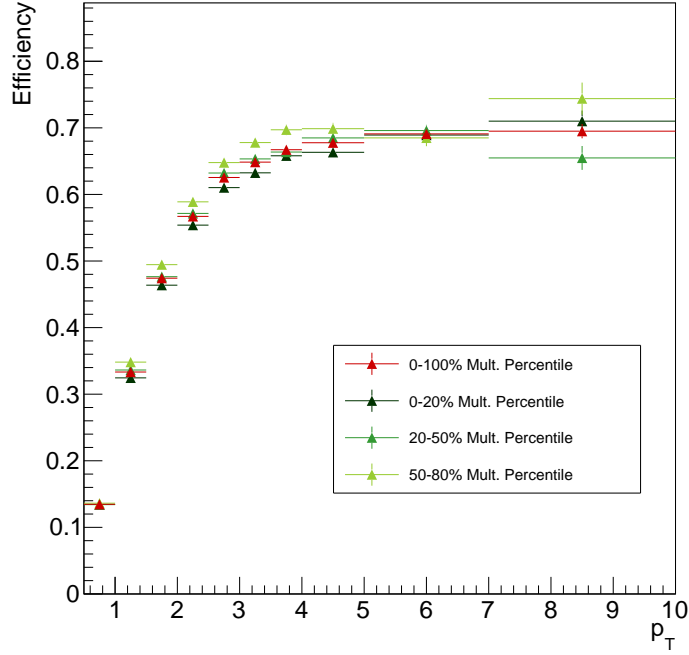


**Fig. 55:** Efficiency vs.  $p_T$  for  $\Lambda$  reconstruction using resonance technique for each multiplicity bin, along with an integrated 0-100% point in red. There does not appear to be any significant dependence on multiplicity. Also worth nothing that the efficiency is higher for this technique when compared to the V0 technique, as expected (all AOD tracks from V0 finder daughters are also in total AOD track list).

#### 8.1.4 Mixed Event Acceptance Correction

The procedure for correcting for finite detector acceptance in our angular correlations is exactly the same as the one described in Section ??.

#### 8.1.5 Removal of Combinatorial $p - \pi$ Background

Since we do not know which  $p - \pi$  pairs came from a real  $\Lambda$  decay, we must remove the contribution to the angular correlation structure due to the combinatorial background of  $p - \pi$  pairs that did not come from a  $\Lambda$ .

To do this,  $h-(p\pi)$  angular correlations are measured for unlike-sign  $p\pi$  pairs within the right sideband (RSB) for each multiplicity bin. The correlation structure in the RSB is then normalized to its integral to give an estimate of the combinatorial background shape, as the RSB should contain little-to-no  $p\pi$  pairs that came from a  $\Lambda$ . The self-normalized 1D  $\Delta\phi$  distributions for different choices of RSB regions are shown in Figure ?. As the shapes are similar for each choice of RSB, we conclude that there is no substantial contribution from  $p\pi$  pairs coming from  $\Lambda$  decay.

For the remainder of this resonance technique analysis we will be using  $1.16 < M_{RSB} < 1.18$  as our choice of RSB region for each multiplicity bin.

Next, the  $h - p\pi$  angular correlation in our chosen sideband region is scaled to match the integral of our background in our signal region. However, this scaling is not performed directly as while the Signal/Background and Signal/(Signal + Background) ratios are the same for the single-particle  $\Lambda$  distribution and its corresponding invariant mass axis in our  $h - \Lambda$  distribution, the total yields are different. We therefore scale the  $h - p\pi$  distribution in the RSB to the BG integral in our signal region found using the following formula:

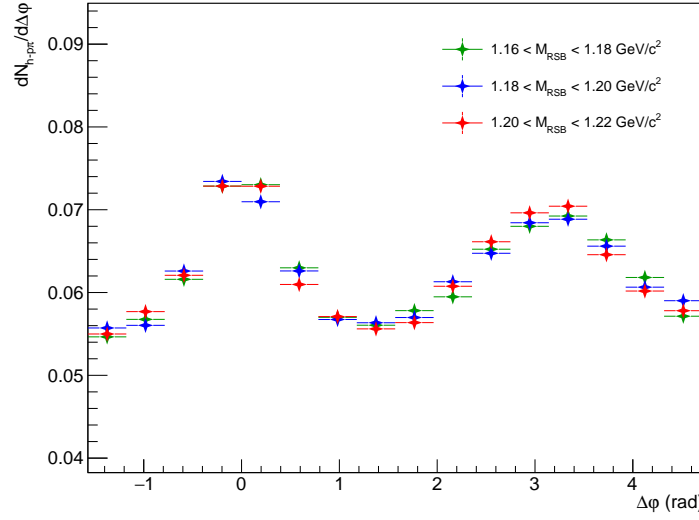


**Fig. 56:** The projected  $\Delta\phi$  distributions for different choices of RSB within the  $-1.2 < \Delta\eta < 1.2$  region. The correlation shapes are identical within the statistical errors.

$$h - p\pi \text{ Combinatorial BG} = (\text{Integral of } h - p\pi \text{ in Signal Region}) \times \left(1 - \frac{S}{S+B}\right), \quad (3)$$

where  $S$  and  $B$  are calculated in the Signal region using the single-particle  $\Lambda$  distributions from Table ??.

Once the  $h - p\pi$  angular correlation in the RSB is scaled to match the  $h - p\pi$  Combinatorial BG, it is subtracted from the total  $h - p\pi$  distribution in our signal region, then scaled to correct for our finite signal region. This scale factor is calculated using the following formula:

$$S_{\text{finite region}} = (\text{Integral of residual in signal region} / \text{Total integral of residual})^{-1} \quad (4)$$

Once the scale factor is applied, we are then left with the full  $h - \Lambda$  2D angular correlations and corresponding 1D  $\Delta\phi$  projections, shown in Figures ?? and ??, respectively.

### 8.1.6 Near-side, Away-side and Underlying Event Yield Extraction

The procedure for extracting the near-side, away-side and underlying event yields is exactly the same as the one described in Section ?. However, due to the statistical fluctuations introduced by the combinatorial background subtraction, we will be limiting the underlying event fitting procedure to the “6-bin average” method. The final  $\Delta\phi$  correlations with their corresponding underlying event fits can be seen in Figure ?. The extracted per-trigger yields and corresponding errors are shown in Table ?.

Multiplicity Bin	Near-side Jet	Away-side Jet	Underlying Event	Total
0-20%	$4.21\text{e-}3 \pm 0.38\text{e-}3$	$5.07\text{e-}3 \pm 0.54\text{e-}3$	$1.01\text{e-}1 \pm 0.01\text{e-}1$	$1.11\text{e-}1 \pm 0.07\text{e-}1$
20-50%	$3.66\text{e-}3 \pm 0.31\text{e-}3$	$3.58\text{e-}3 \pm 0.35\text{e-}3$	$5.34\text{e-}2 \pm 0.07\text{e-}2$	$6.05\text{e-}2 \pm 0.05\text{e-}2$
50-80%	$3.40\text{e-}3 \pm 0.31\text{e-}3$	$3.62\text{e-}3 \pm 0.40\text{e-}3$	$2.51\text{e-}2 \pm 0.08\text{e-}2$	$3.21\text{e-}2 \pm 0.05\text{e-}2$

**Table 16:** Per-trigger pairwise  $h - \Lambda$  extracted yields and corresponding errors in the different kinematic regions for each multiplicity bin. The yields were extracted using the same procedure described in Section ?.

### 8.1.7 Results and Comparison with V0 Technique

The final  $h - \Lambda/h - h$  ratio vs. multiplicity plot for  $\Lambda$ s reconstructed using the resonance technique is shown in Figure ???. The per-trigger near and away-side pairwise yields vs. multiplicity for the  $h - \Lambda$  and  $h - h$  distributions are shown in Figure ??.

A comparison of the final per-trigger  $h - \Lambda \Delta\phi$  correlation structure for the resonance and V0 techniques can be seen in Figure ???. The correlation shapes are nearly identical, with the resonance technique having slightly larger uncertainties due to the combinatorial background subtraction. While this is not surprising (a  $\Lambda$  is a  $\Lambda$ , regardless of how it is reconstructed), it serves as a powerful cross check to our central values from the V0 technique.

## 8.2 Single Trigger $h - \Lambda$ , $h - h$ Correlations

As our technique does not directly give the yields of the associated particles, it could be possible that event-by-event fluctuations in the number of trigger particles could lead to small differences between the number of associated pairs and the number of associated particles. To be more explicit, if there are two triggers and two associated particles in a single event, the correlation measurement will give a yield of four trigger-associated pairs, while the number of associated particles is only two.

Furthermore, if there are two triggers corresponding to two separate jets in an event, we would be misplacing the true kinematic regions of our trigger-associated pairs: if one of the trigger-associated pairs lies in the near-side jet, it's possible when that associated particle gets correlated with another trigger, it would be placed in the "underlying event". We can get a rough estimate of how often this occurs by looking at the number of triggers per event, shown in Figure ??.

While events with multiple triggers ( $\geq 1$ ) are rare—less than 5%—an additional crosscheck was performed to investigate the effect of using multiple triggers within an event has on our final measurement. For this crosscheck, we perform the exact same analysis as demonstrated in this note, but we only use a single trigger hadron for each triggered event. If the event has multiple triggers, we select the trigger with the highest momentum within our  $4 < p_T < 8$  GeV/c range. The final per-trigger  $\Delta\phi$  distributions for each multiplicity bin are shown in Figures ?? ( $h - \Lambda$ ) and ?? ( $h - h$ ). The ratio of the single-trigger  $\Delta\phi$  distribution to the total-trigger  $\Delta\phi$  distribution for each multiplicity bin for both the  $h - h$  and  $h - \Lambda$  correlations is shown in Figure ??.

As the single-trigger/total-trigger ratio is flat for both the  $h - h$  and  $h - \Lambda$  distributions across all multiplicity bins, the effect on our final yield and ratio measurements would only be a change of scale. As this scale factor is the same across all multiplicity bins, we conclude that using our standard per-trigger correlation method accurately captures the behaviour of the  $\Lambda/h$  ratio in the different kinematic regions with respect to multiplicity.

## 8.3 MonteCarlo Closure Tests

### 8.4 Dihadron Comparison with $\phi$ Analysis

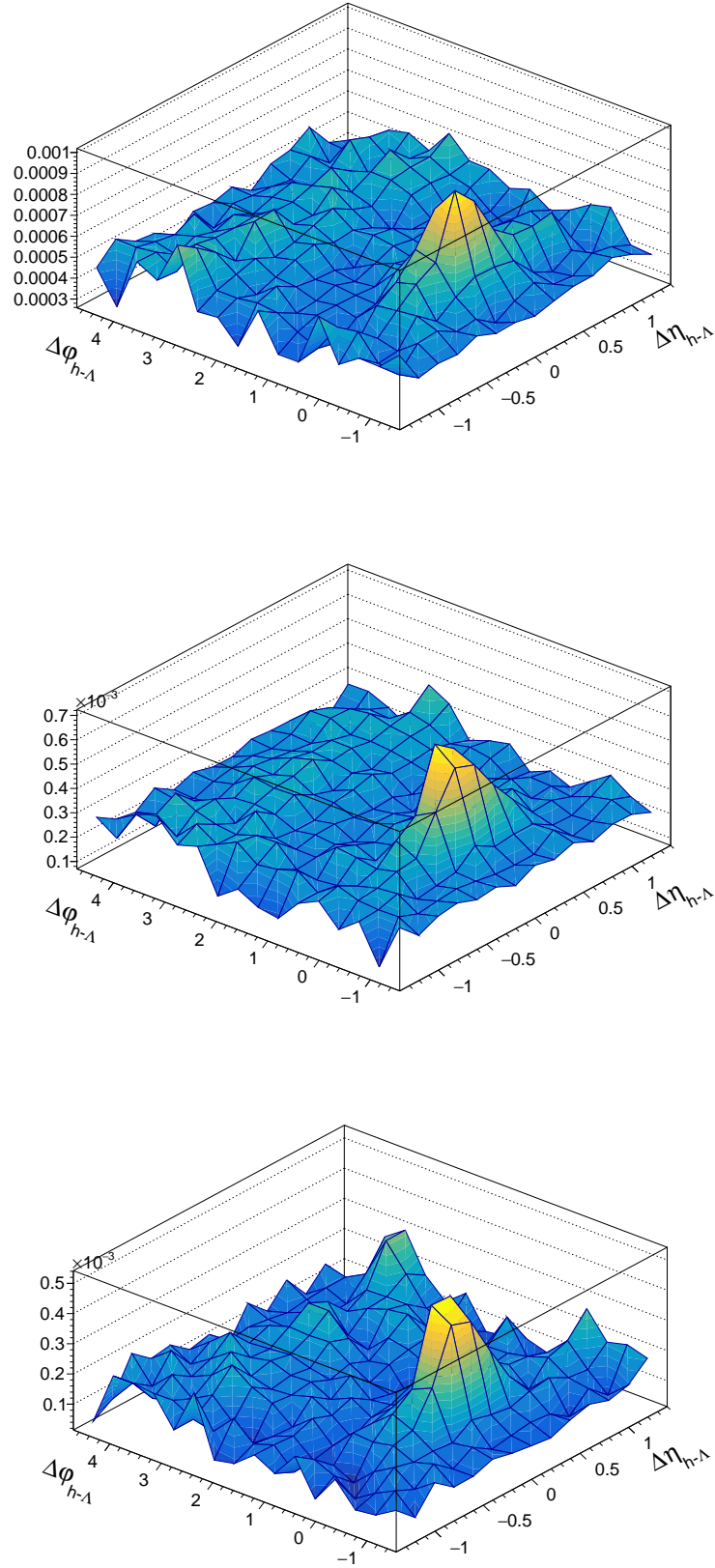
As both this analysis and the similar analysis for the  $\phi$  are run over the same data set, with the same cuts being used on both the trigger and associated particles, we would expect the corresponding dihadron  $\Delta\phi$  correlations from both analyses to be the same. As these analyses are being performed by humans with vastly different coding styles, we should do a thorough comparison of the final dihadron correlations to ensure they are indeed identical. The final per-trigger dihadron  $\Delta\phi$  distributions in each multiplicity bin for both the  $\phi$  and  $\Lambda$  analyses are shown in Figure ??, with their corresponding ratios shown in Figure ???. The dihadron distributions are identical for both analyses, as expected.

## 8.5 Jet vs. Total Production comparison

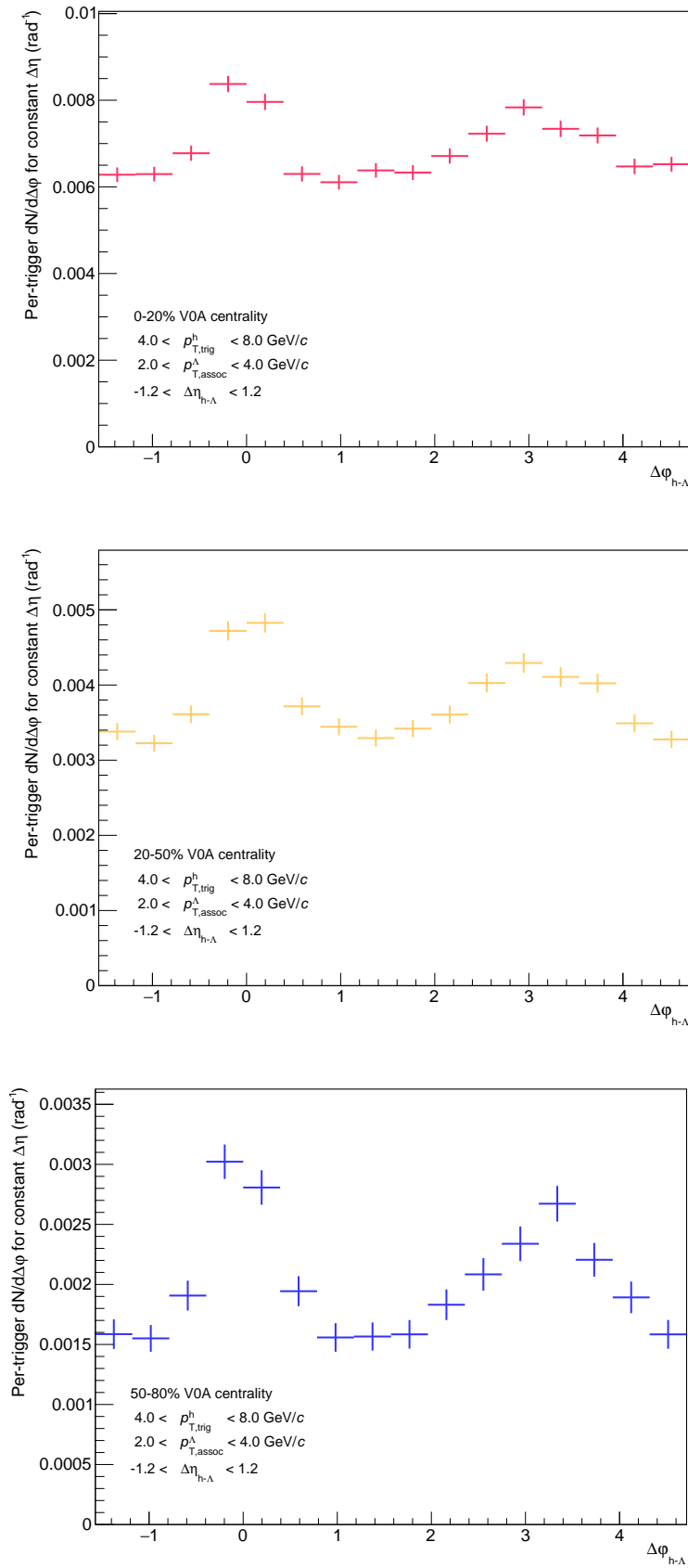
To get a quantitative look at the differences between low multiplicity events (more jet) and high multiplicity events (more underlying event) and the effect this has on the correlation ratios, we can measure the ratio of Jet pairs over Total pairs (i.e. the fraction of correlated pairs that are in a jet) (fig. ??).

From this measurement, there is a clear difference in behavior of jet production of associated  $\phi$  mesons vs. associated inclusive hadrons as multiplicity increases. The fraction of jet-produced hadrons shows a sharp decrease as a function of multiplicity, while the fraction of jet-produced  $\phi$  mesons is significantly lower and flatter as a function of multiplicity. This shows that the balance of production methods of  $\phi$  mesons are mostly independent of multiplicity, while the production methods of hadrons significantly shifts from jet production towards underlying event production as multiplicity increases.

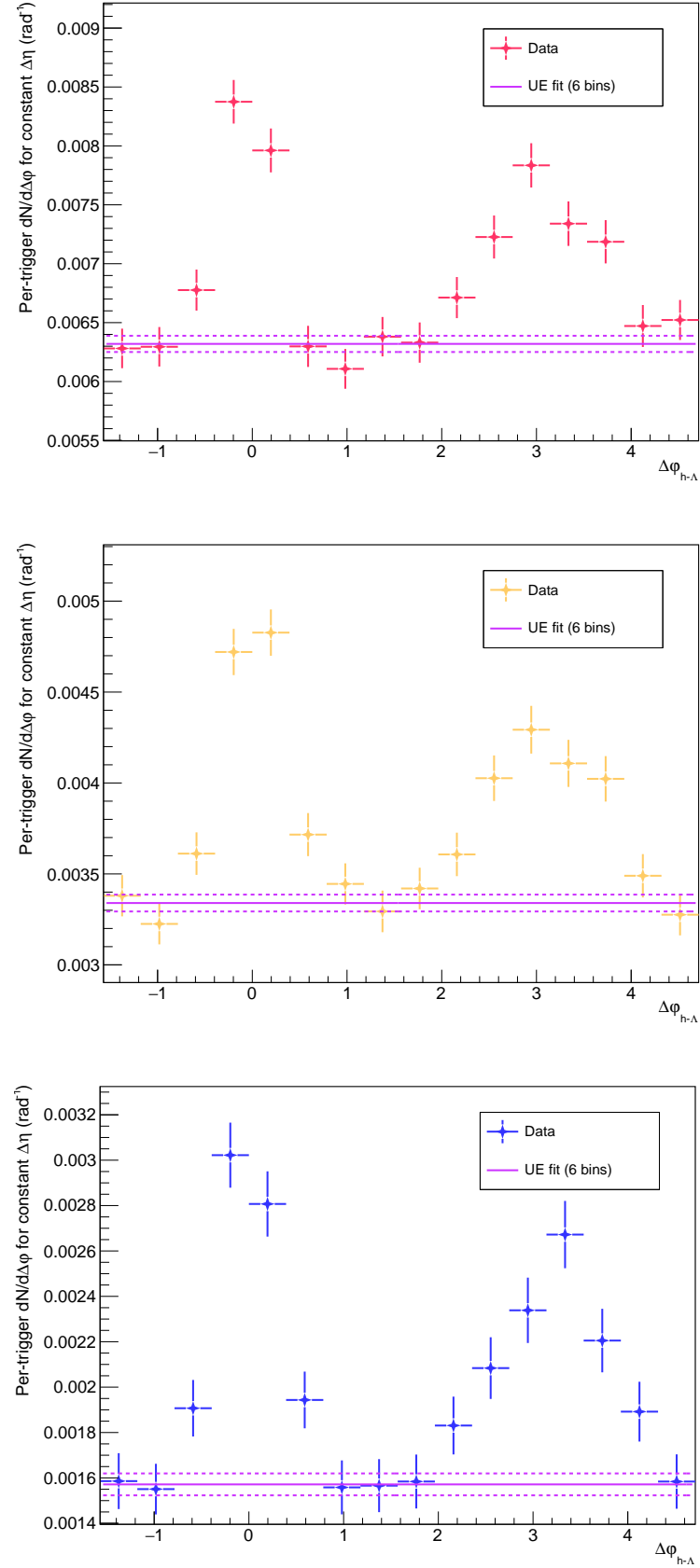




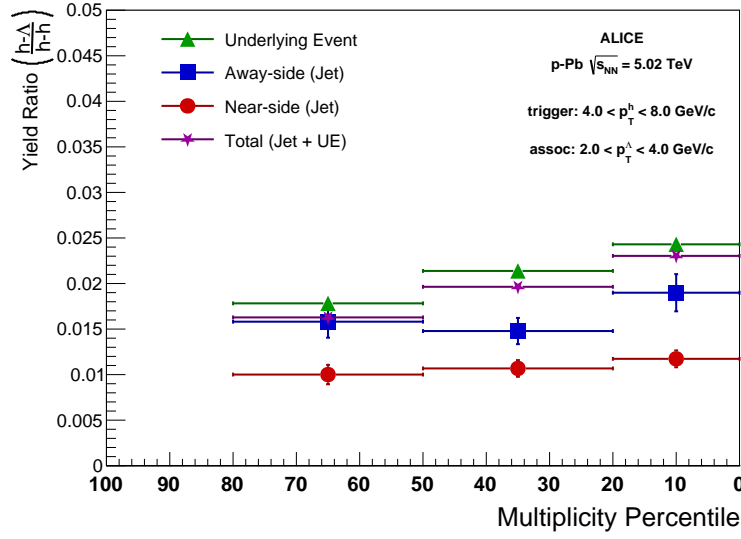
**Fig. 57:** The final per-trigger  $h - \Lambda$  2D  $\Delta\eta\Delta\phi$  distributions after mixed event acceptance correction and combinatorial background subtraction for the 0-20% (top), 20-50%(center) and 50-80% (bottom) multiplicity bins.



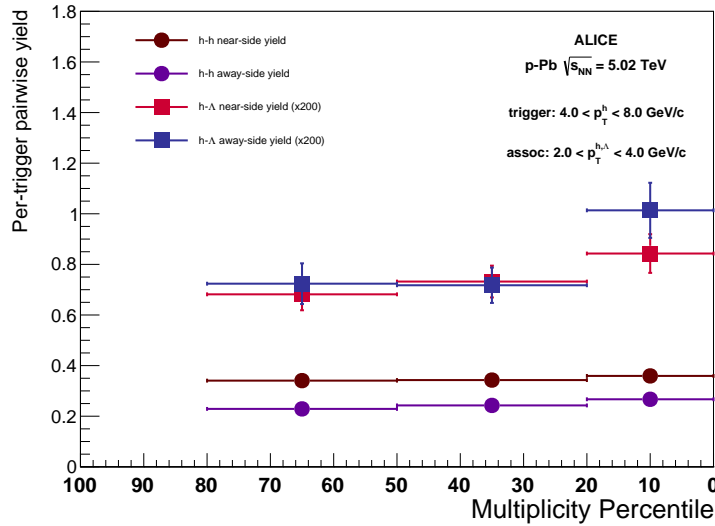
**Fig. 58:** The final per-trigger  $h - \Lambda$   $\Delta\phi$  distributions after mixed event acceptance correction and combinatorial background subtraction for the 0-20% (top), 20-50% (center) and 50-80% (bottom) multiplicity bins within  $-1.2 < \Delta\eta < 1.2$ .



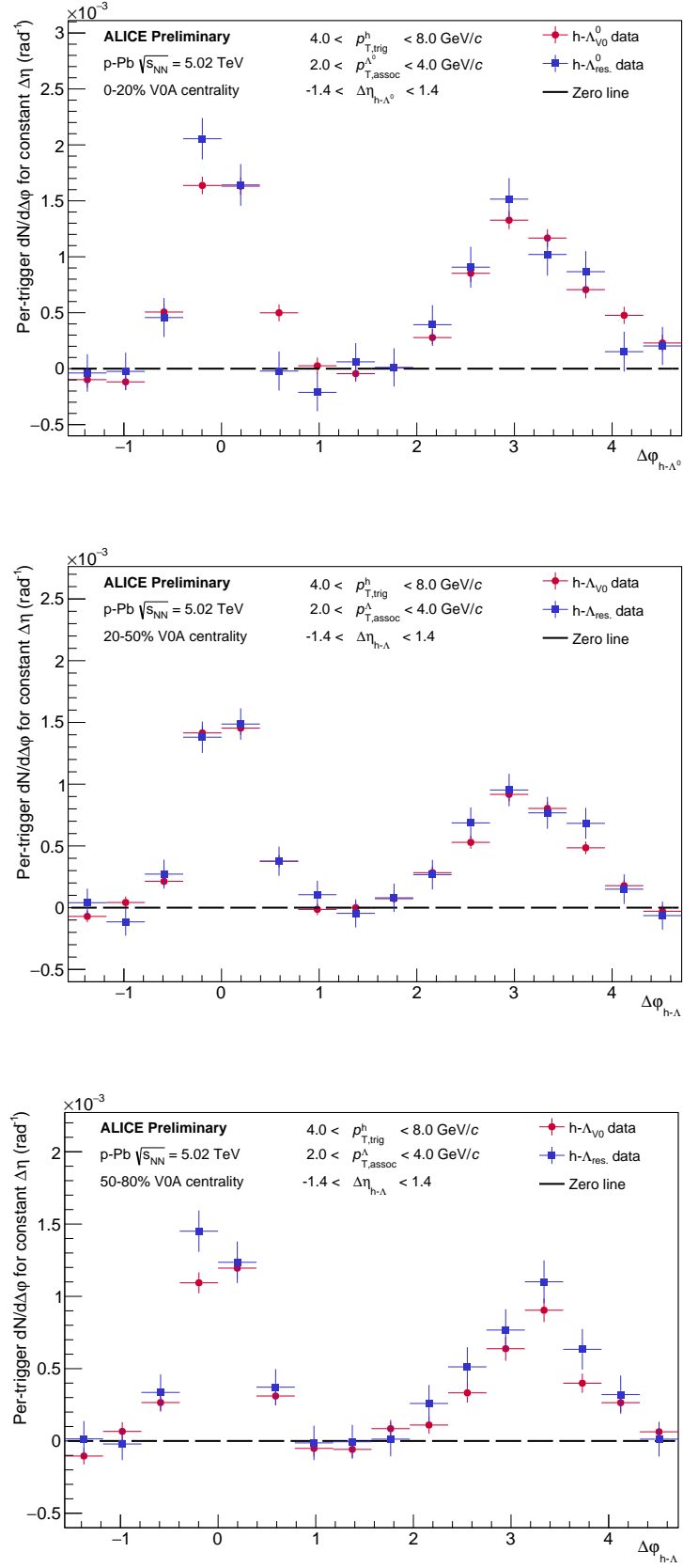
**Fig. 59:** The final  $h - \Lambda$   $\Delta\phi$  correlations with underlying event fit for the 0-20% (top), 20-50%(center) and 50-80% (bottom) multiplicity bins. The solid line is the central value for the fit, with the dashed lines representing the error (+/-). The underlying event fit was taken using the 6-bin technique described in Section ??.



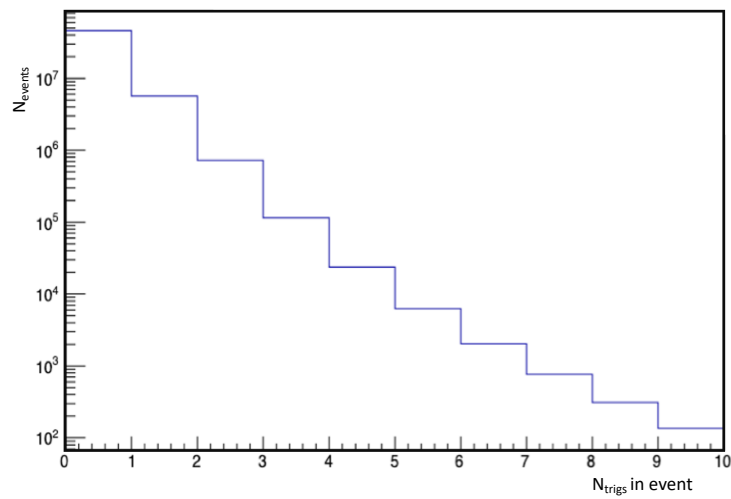
**Fig. 60:** The final  $h - \Lambda/h - h$  ratio vs. multiplicity plot for  $\Lambda_s$  reconstructed using the resonance technique. While the error bars and statistical fluctuations are larger than the same plot with  $\Lambda_s$  reconstructed using the V0 technique (due to the comb. BG subtraction), the general trends are the same.



**Fig. 61:** The final  $h - \Lambda/h - h$  per-trigger pairwise jet yields vs. multiplicity plot for  $\Lambda_s$  reconstructed using the resonance technique. The general trends are very similar to the same plot with  $\Lambda_s$  reconstructed using the V0 technique, just with larger uncertainties.

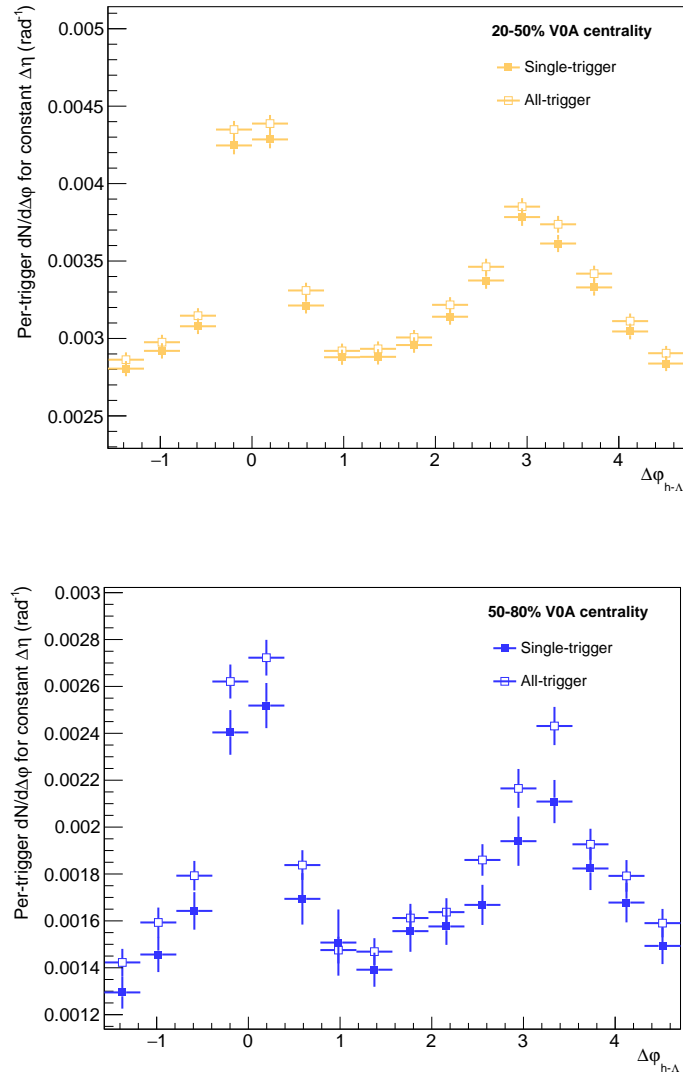


**Fig. 62:** The final per-trigger  $h-\Lambda$   $\Delta\phi$  correlations for  $\Lambda$ s reconstructed using the resonance technique (blue) and the V0 technique (red) for each multiplicity bin (from top to bottom). All three multiplicity bins show very good agreement between the two techniques.

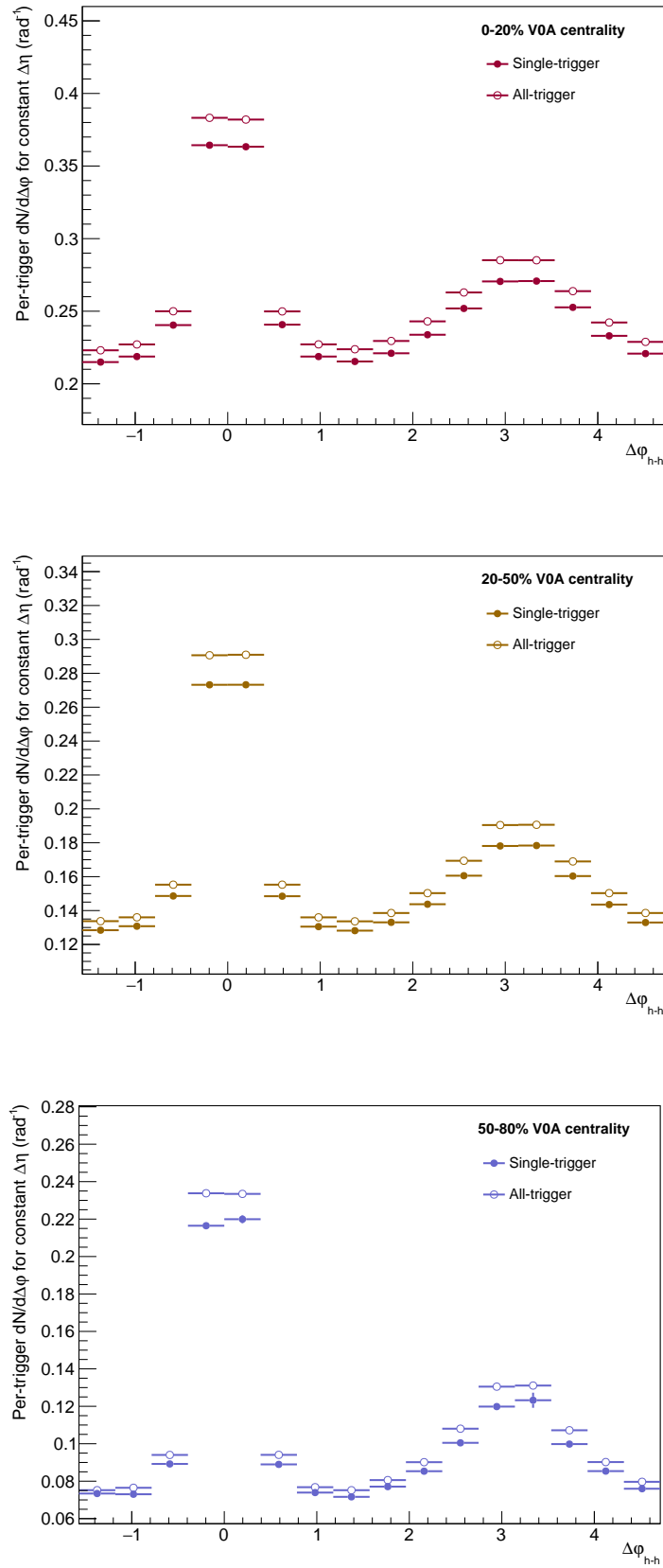


**Fig. 63:** A log-plot showing the number of triggers per event across our data sample. Only a small fraction of events have at least a single trigger, and of those events, only a small fraction have more than one trigger

figures/h\_lambda\_dphi\_subtracted\_0\_20\_singletrigger.pdf

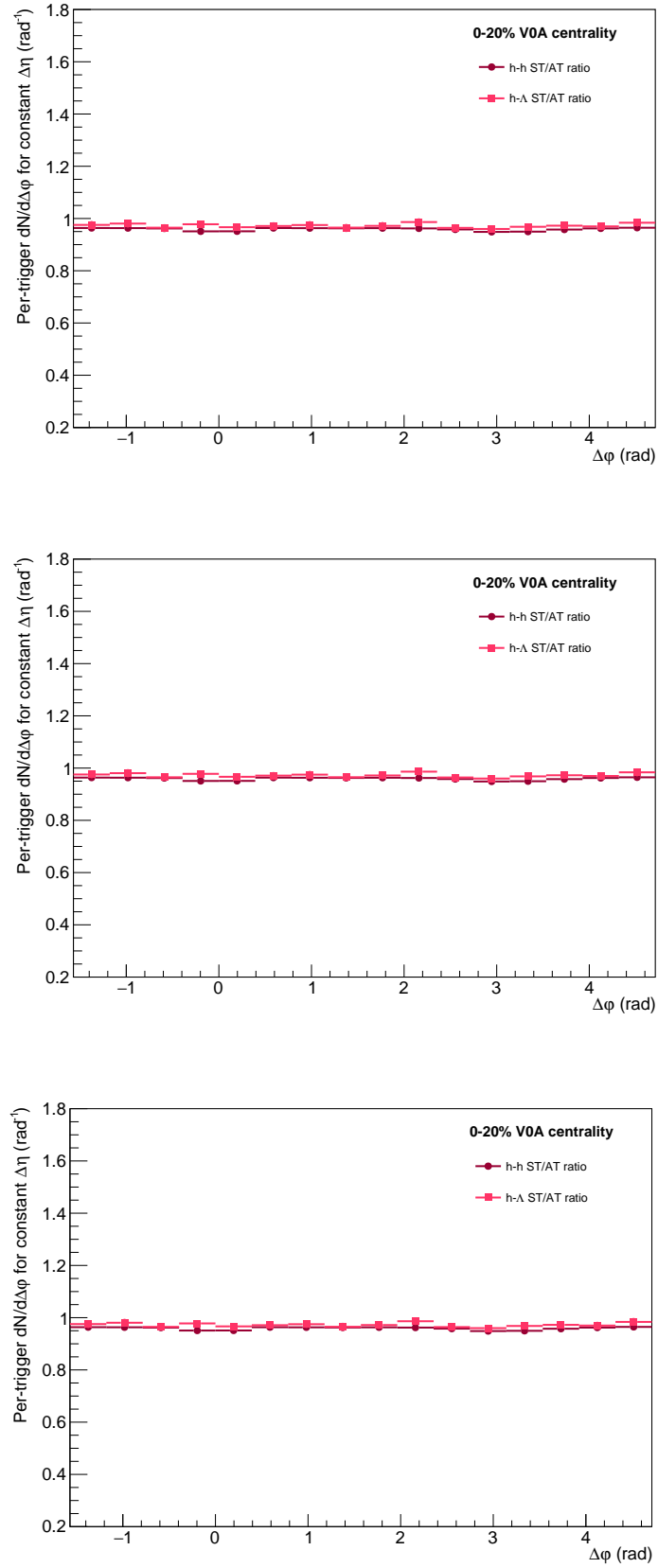


**Fig. 64:** The per-trigger  $h - \Lambda$   $\Delta\phi$  comparison between using a single trigger (closed points) and all triggers (open points) in a given event for the 0-20% (top), 20-50% (center) and 50-80% (bottom) multiplicity bins. The only

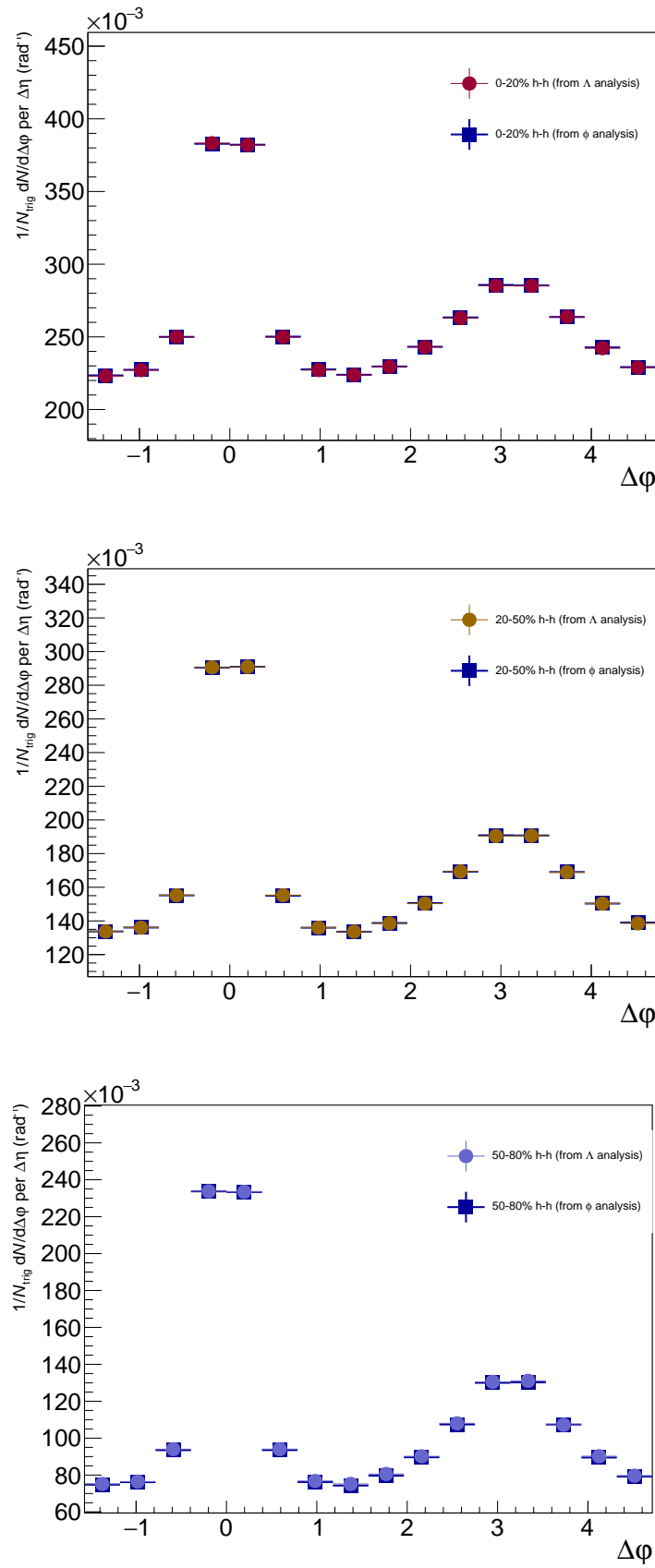


**Fig. 65:** The per-trigger  $h-h$   $\Delta\phi$  comparison between using a single trigger (closed points) and all triggers (open points) in a given event for the 0-20% (top), 20-50% (center) and 50-80% (bottom) multiplicity bins. The only difference appears to be a scale factor.

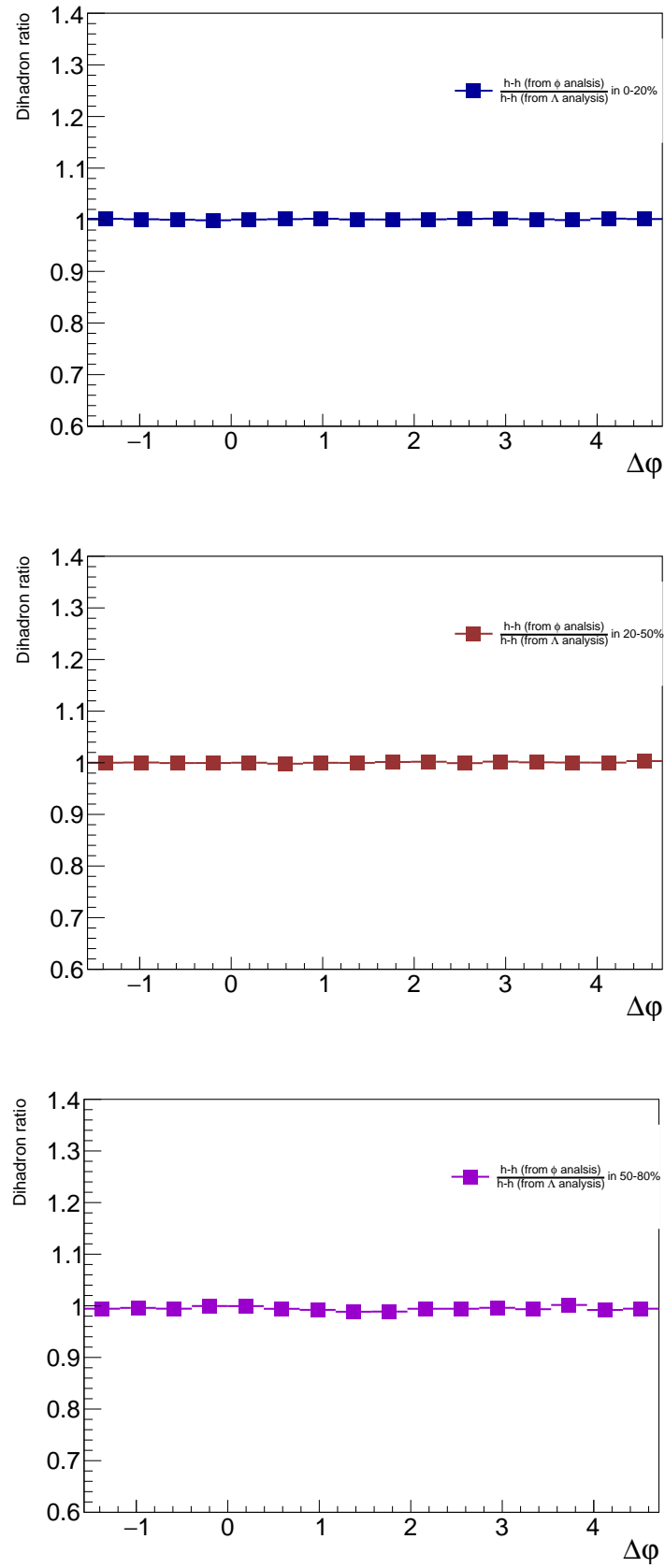




**Fig. 66:** The single-trigger/total-trigger ratio for both the  $h - \Lambda$  and  $h - h$   $\Delta\phi$  distributions. The ratios are flat across  $\Delta\phi$ , and the scale factor is the same for each multiplicity bin.



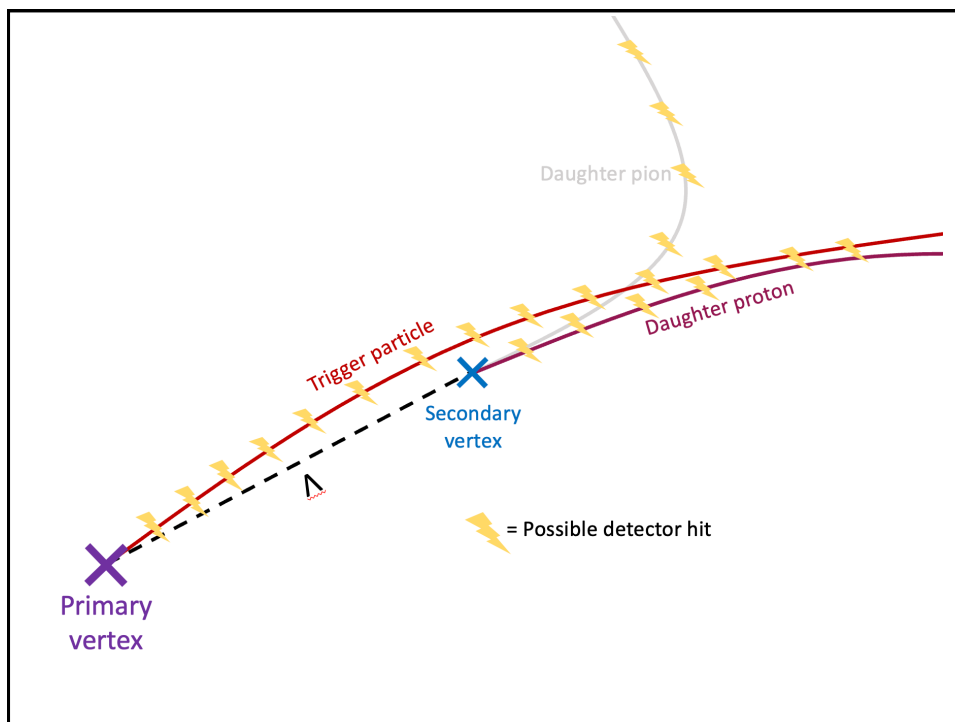
**Fig. 67:** Comparison of the the dihadron  $\Delta\phi$  correlations between the  $\phi$  and  $\Lambda$  analyses for the 0-20% (top), 20-50% (center) and 50-80% (bottom) multiplicity bins. They are functionally identical for all multiplicity bins.



**Fig. 68:** The dihadron ratio between the  $\phi$  and  $\Lambda$  analyses for the 0-20% (top), 20-50% (center) and 50-80% (bottom) multiplicity bins. The ratios are consistent with unity for all multiplicity bins.



**Fig. 69:** Fraction of Jet Produced correlated pairs as a function of multiplicity for low momentum (left) and high momentum (right) regions. In both momentum regions, the Jet fraction of h-h pairs decreases significantly as a function of multiplicity. For h- $\phi$  pairs, however, the overall fraction coming from jets only slightly decreases as multiplicity increases.

736 **9 Additional Plots**

**Fig. 70:** Simple diagram depicting why track merging occurs: The  $\Lambda$  daughter proton has fewer possible hits in the detector, and is physically close to the trigger particle. When the tracks are being reconstructed, the proton track is “merged” over by the trigger track as the Kalman filtering process favors the track with more hits.